

Development of a Converter-Fed Reluctance Synchronous Generator Wind Turbine Controller

by

Jon-Pierre du Plooy



*Thesis presented in partial fulfilment of the requirements
for the degree of Master of Science in Electrical Engineering
in the Faculty of Engineering at Stellenbosch University*

Supervisor: Dr. N. Gule

March 2015

Declaration

By submitting this thesis electronically, I declare that the entirety of the work contained therein is my own, original work, that I am the sole author thereof (save to the extent explicitly otherwise stated), that reproduction and publication thereof by Stellenbosch University will not infringe any third party rights and that I have not previously in its entirety or in part submitted it for obtaining any qualification.

Date: 24/02/2015

Copyright © 2015 Stellenbosch University
All rights reserved.

Abstract

The growing contribution of wind energy to utility grids has sparked interest in small-scale wind turbines and thus a growing global cumulative installed capacity. Small-scale wind turbines find use in the saving of cost of electricity or for the carbon footprint reduction of small farms and small-holdings, as well as the electrification of rural communities.

A goal of any wind turbine is to produce power at as low of a cost per unit energy as possible. Thus, a generator with a high power density and high efficiency is essential. The reluctance synchronous machine (RSM) is a strong competitor in this regard. Additionally, the RSM is a robust brushless topology that has good properties of manufacturability. However, studies published on the use of RSMs as generators in wind turbines is limited. This study serves to explore the performance and controllability of an RSM as a generator in a small-scale 9.2 kW wind turbine.

For maximum power capture, it is desirable to have a wind turbine vary its rotor speed. However, there is a limit to the power that the generator may produce and so techniques are employed to reduce the captured power when operating above the rated wind speed. A turbine controller is developed that employs a speed-controlled maximum power point tracking (MPPT) technique for maximum power capture and soft-stalling of the blades to reduce power capture at excessive wind speeds. The RSM is modelled along with a turbine simulation model, complete with a wind source generator, to evaluate the performance of the system.

Speed-controlled MPPT is known to sacrifice torque smoothness for fast tracking performance. To mitigate these harsh effects on the drivetrain, the speed reference of the generator is filtered to provide an average response to the optimal speed reference. This is shown to reduce the frequent and excessive speed, torque, and electrical power variations though optimal performance is not possible. However, any reduction on drivetrain fatigue that will maximise operation time of the turbine is considered an important gain.

The RSM proves to have qualities that are applicable to wind turbine applications with its high efficiency, good manufacturability properties, low cost, and high robustness. Its higher power density over induction machines is also favourable though power electronics are required for optimal operation of the machine.

Opsomming

Die groeiende bydrae van wind energie te nut roosters het aanleiding gegee tot belangstelling in kleinskaalse wind turbines en dus 'n groeiende wêreldwye kumulatiewe geïnstalleerde kapasiteit. Kleinskaalse wind turbines vind ook gebruik in die besparing van koste van elektrisiteit, of vir die koolstofvoetspoor vermindering van klein plase en klein-hoewes, sowel as die elektrifisering van landelike gemeenskappe.

Een van die doelwitte van enige wind turbine is om krag te produseer teen so laag van 'n koste per eenheid energie as moontlik. Dus, 'n kragopwekker met 'n hoë krag digtheid en hoë doeltreffendheid is noodsaaklik. Die reluktansie sinchroonmasjien (RSM) is 'n sterk mededinger in hierdie verband. Daarbenewens is die RSM 'n robuuste borsellose topologie wat goeie eienskappe van vervaardigbaarheid het. Maar studies oor die gebruik van RSMs as kragopwekkers gepubliseer in die wind turbines is beperk. Hierdie studie dien om die prestasie te ondersoek en die beheerbaarheid van 'n RSM as 'n a kragopwekker in 'n klein-skaal 9.2 kW wind turbine te verken.

Vir maksimum krag vang is dit wenslik dat die wind turbine sy rotor spoed wissel. Maar daar is 'n beperking op die krag wat die kragopwekker kan produseer en daarom word tegnieke gebruik om die gevange krag te verminder wanneer daar bo die gegradeerde wind spoed gewerk word. 'n Turbine beheerder word ontwikkel wat werk om 'n spoedbeheer maksimum kragpunt dop tegniek vir maksimum krag vang en die sagtsteking van die lemme krag vang deur oormatige wind spoed te verminder. Die RSM is gemodelleer saam met 'n turbine simulatie model kompleet met 'n wind bron kragopwekker om die prestasie van die stelsel te evalueer.

Spoedbeheerde maksimum kragpunt dop is bekend om wringkrags gladheid vir 'n vinnige dop prestasie te offer. Om hierdie harde gevolge op die kragoorbringstelsel te versag is die spoed verwysing van die kragopwekker gefiltreer om 'n gemiddelde reaksie op die optimale spoed verwysing te verskaf. Dit word getoon om gereelde en hoë spoed, wringkrags en elektriese krag variasies te verminder al is optimale prestasie nie moontlik nie. Enige afname van aandryfstelsel moegheid wat operasie tyd van die turbine maksimeer word beskou as 'n belangrike gewin.

Die RSM bewys eienskappe wat van toepassing is op die turbine aansoeke na aanleiding met sy hoë doeltreffendheid, goeie vervaardigbaarheid eienskappe, lae koste end ' hoë robuustheid. Sy hoër krag digtheid oor induksiemasjien is ook gunstig al is drywingselektronika nodig vir optimale werking van die masjien.

Acknowledgements

I would like to express my sincere gratitude to the following people:

- Dr. N. Gule, my supervisor, for his guidance and supervision.
- Eduan Howard for his advice.
- David Groenewald for his in-depth knowledge of SV-PWM and assistance with testbench problems.
- Wikus Villet for bringing me up to speed with all things related to reluctance synchronous machines.
- Everyone in the EMLAB for all the laughs that will forever remain memories.
- My family for their love and support.

Nomenclature

Acronyms

2D	2-dimensional
AI	Artificial intelligence
HAWT	Horizontal-axis wind turbine
HCS	Hill-climb searching
IEC	International Electrotechnical Commission
IG	Induction generator
IM	Induction machine
LVRT	Low-voltage ride through
LPF	Low-pass filter
LUT	Lookup table
MPPT	Maximum power point tracking
PM	Permanent magnet
PMSG	Permanent magnet synchronous generator
PMSM	Permanent magnet synchronous machine
P&O	Perturb-and-observe
PSD	Power spectral density
PSF	Power signal feedback
RMS	Root mean square
RPS	Rapid-prototyping system
RSG	Reluctance synchronous generator
RSM	Reluctance synchronous machine
SCIG	Squirrel-cage induction generator
SEIG	Self-excited induction generator
SMA	Simple moving average
SRM	Switched reluctance machine
SV-PWM	Space vector pulse width modulation
TSR	Tip-speed ratio

NOMENCLATURE

VAWT	Vertical-axis wind turbine
VSC	Voltage-source converter
VSD	Variable-speed drive
ZOH	Zero-order hold

Symbols

B	Friction coefficient
F_s	Switching frequency [Hz]
J	Moment of inertia [kg·m ²]
T	Torque [Nm]
T_s	Sampling period
U_{dc}	DC bus voltage [V]
f_s	Sampling frequency [Hz]
i	Current [A]
k_{cc-d}	Current controller d-axis proportional gain
k_{cc-q}	Current controller q-axis proportional gain
k_{sc-i}	Speed controller integral gain
k_{sc-p}	Speed controller proportional gain
n_g	Gearbox ratio
t	Time [s]
u	Voltage [V]
v_w	Instantaneous wind velocity [m/s]
θ	Current angle [Degrees]
λ	Tip-speed ratio
ψ	Flux linkage [T]
ω	Angular speed [rad/s]

Subscripts

a	Aerodynamic
ls	Low-speed
hs	High-speed
g	With reference to the generator
t	With reference to the turbine hub
d, q	Synchronously-rotating dq-reference frame

Table of Contents

Declaration	i
Abstract	ii
Acknowledgements	iv
Nomenclature	v
Table of Contents	vii
List of Figures	x
1 Introduction	1
1.1 Small-scale wind turbine topologies	2
1.1.1 Drivetrain topologies	2
A Horizontal- and vertical-axis wind turbines	2
B Geared and direct-drive topologies	3
C Fixed- and variable-speed operation	4
1.1.2 The generator	5
A Squirrel-cage induction generator	5
B Permanent magnet synchronous generator	6
1.1.3 Wind turbine control methods	6
A Region 2 - Maximum power capture	7
B Region 3 - Power limiting	9
1.2 The reluctance synchronous machine	10
1.3 Problem statement	11
1.4 Aim and objectives	11
1.5 Thesis outline	12
2 RSM-based wind turbine	13
2.1 The reluctance synchronous machine	13
2.1.1 Theory of operation	13
2.1.2 Modelling the RSM	15
A Core losses	16

TABLE OF CONTENTS

2.1.3	Generating power with the RSM	17
2.1.4	Parameter values	18
A	Flux linkage	18
B	Linear inductance	19
C	Instantaneous inductance	20
2.1.5	Performance data	20
A	Current magnitude	20
B	Efficiency	21
C	Power factor	22
2.2	The wind turbine	23
2.2.1	Turbine blades	23
2.2.2	Gearbox ratio	23
3	Design of wind turbine controllers	24
3.1	Current controller	24
3.1.1	Decoupling the voltage equations	25
3.1.2	Zero-order hold	26
3.1.3	Closed-loop model	27
3.2	Speed controller	31
3.2.1	Open-loop model	31
3.2.2	Closed-loop system	32
3.3	Turbine system controller	34
3.3.1	Region 2 - MPPT control	34
3.3.2	Speed limit mode	35
3.3.3	Torque limit control	35
3.3.4	Aerodynamic power estimator	37
3.3.5	Complete wind turbine controller	39
3.3.6	Compensated stator current	41
4	Wind turbine modelling and simulation	42
4.1	Wind generator	43
4.2	Aerodynamics	44
4.3	Drivetrain	46
4.4	Generator	48
4.5	Current controller	49
4.6	Speed controller	50
4.7	Turbine system controller	50
5	Overall wind turbine results	51
5.1	Simulation results	51
5.1.1	Power coefficient curve gradient	51

TABLE OF CONTENTS

5.1.2	Gearbox ratio	53
5.1.3	Simple moving average window size	55
5.2	Measurement results	57
5.2.1	Testbench	57
5.2.2	Validity of estimated generator torque	59
5.2.3	Results from test cases ($n_g = 12$)	60
A	Maximum power point tracking operation	61
B	Speed-limited operation	61
C	Torque-limited operation	64
5.2.4	Results from test cases ($n_g = 14$)	66
A	Maximum power point tracking operation	67
B	Speed-limited operation	67
C	Torque-limited operation	67
6	Conclusions and future work	71
6.1	Conclusions	71
6.2	Future work	72
6.2.1	Blade soiling	72
6.2.2	Air density	72
6.2.3	Torque control MPPT	74
	Bibliography	75

List of Figures

1.1	Estimated global cumulative installed capacity of small-scale wind turbines [4]. . . .	2
1.2	Illustration of HAWT and VAWT.	3
1.3	Regions of wind turbine operation with curves representing generator power output, the Betz limit, and maximum wind power.	7
2.1	Illustration of the simplest form of an RSM rotor, the “dumb-bell”. The rotor resembles that of a wound-rotor synchronous machine, without the field winding. . .	13
2.2	Quarter-model of RSM rotor and stator as used in FE analysis.	14
2.3	Electrical schematic of ideal RSM dq-axis voltage equations.	15
2.4	Electrical model of RSM incorporating stator core losses represented by R_c	16
2.5	Phasor diagrams illustrating shift in stator current vector as a result of core losses in an RSM for (a) motoring and (b) generating [53].	16
2.6	Phasor diagrams demonstrating the voltage, current, and flux vectors within an RSM for motoring and generating operation.	17
2.7	Flux linkages for 0° (no q-axis flux), 90° (no d-axis flux), and 65° current angles plotted against (a) axis current and (b) stator current magnitudes for the dq-axes. .	18
2.8	Linear inductances for 0° (no q-axis flux), 90° (no d-axis flux), and 65° current angles plotted against (a) axis current and (b) stator current magnitudes for the dq-axes. .	19
2.9	Instantaneous inductances for 0° (no q-axis flux), 90° (no d-axis flux), and 65° current angles plotted against (a) axis current and (b) stator current magnitudes for the dq-axes.	20
2.10	Measured current magnitude versus current angle for motoring and generating modes. Measurements performed at rated speed and torque [53].	21
2.11	Measured efficiency versus current angle for motoring and generating modes. Measurements performed at rated speed and torque [53].	22
2.12	Measured power factor versus current angle for motoring and generating modes. Measurements performed at rated speed and torque [53].	22
2.13	Power curves for the blade set used in the study.	23
3.1	Block diagram of RSM electrical model demonstrating the cross-coupling present between the two axes.	25
3.2	Block diagram of RSM electrical model demonstrating the decoupling procedure used.	25

LIST OF FIGURES

3.3	Equivalent machine block model after decoupling procedure.	26
3.4	Open-loop and gain-scaled responses of RSM d-axis plant.	30
3.5	Gain scheduled values for d-axis current controller k_{cc-d}	30
3.6	Generator torque versus stator current magnitude and torque coefficient K_t versus stator current magnitude at rated current angle of 65° . FEM results.	31
3.7	Plot of the speed controller proportional and integral gains, k_{sc-p} and k_{sc-i} , respectively, against gearing ratio of the turbine gearbox.	34
3.8	Illustrative comparison between torque trajectories for constant power and constant torque limits by means of soft-stalling, plotted against hub speed.	37
3.9	Measured generator reaction torque, as well as simulated generator reaction torque, versus input current.	38
3.10	Flowchart depicting turbine system controller algorithm operation.	40
4.1	Block diagram illustrating relation between the different Simulink blocks of the wind turbine model.	42
4.2	Kaimal power spectral density.	43
4.3	Wind speed time series generated from the Kaimal PSD for mean wind speeds of 12 m/s and 5 m/s.	44
4.4	Wind generator block of the wind turbine Simulink model.	44
4.5	C_p - λ curve of turbine blades used in the study.	45
4.6	Aerodynamics block of Simulink turbine simulator model.	46
4.7	Diagram representation of turbine drivetrain.	46
4.8	Drivetrain block of Simulink turbine simulator model.	47
4.9	Generator block of Simulink turbine simulator model.	48
4.10	Current controller block of Simulink turbine simulator model.	49
4.11	Speed controller block of Simulink turbine simulator model.	50
5.1	Change in tip-speed ratio λ required for a specific reduction in power coefficient C_p at two different operating points.	51
5.2	Comparison between parameter values for near- λ_{opt} and $\lambda < \lambda_{opt}$ operating points for generator speed, torque, and electrical output power.	52
5.3	Scatter-plot of generator electrical power output versus turbine hub speed with gearing ratio as a parameter.	53
5.4	Energy capture versus average wind speed with gear ratio as a parameter over a three-minute interval.	54
5.5	Plots of the effect that the length of the SMA window length has on the generator speed, generator torque output, and power coefficient of the blades.	56
5.6	Photograph of the testbench setup with IM and RSM. A torque sensor connects the two machines.	57
5.7	Photograph of the VSCs used along with the RPS used for controlling the IM. An oscilloscope is used for viewing system parameters in real-time.	58

LIST OF FIGURES

5.8	Photograph of the RPS used for controlling the RSM and implementing the turbine control algorithm.	58
5.9	Comparison between estimated and measured generator torque, plotted against stator current magnitude at rated current angle.	59
5.10	Testbench measured current and voltage angles.	59
5.11	Plots of the simulated wind data, generator speed, rotor power coefficient, and generator torque estimate for a 10-minute run with $n_g = 12$	60
5.12	Closer view of the MPPT region for the $n_g = 12$ test run of figure 5.11.	62
5.13	Closer view of the speed-limit region for the $n_g = 12$ test run of figure 5.11.	63
5.14	Closer view of the torque-limit region for the $n_g = 12$ test run of figure 5.11.	65
5.15	Plots of the simulated wind data, generator speed, rotor power coefficient, and generator torque estimate for a 10-minute run with $n_g = 14$	66
5.16	Closer view of the MPPT region for the $n_g = 14$ test run of figure 5.15.	68
5.17	Closer view of the speed-limit region for the $n_g = 14$ test run of figure 5.15.	69
5.18	Closer view of the torque-limit region for the $n_g = 14$ test run of figure 5.15.	70
6.1	Change in density of dry air versus air temperature.	73

Chapter 1

Introduction

With the increasing unit capacity of utility-scale wind turbines, as well as the expanding total power contribution to the grid from wind farms [1], there is a growing interest in small-scale wind turbines from the general public, small-farm owners, and remote communities [2]. Plotted in figure 1.1 is the estimated global cumulative installed capacity of wind power from small-scale wind turbines. Estimates from 2013 and beyond are forecasted based on current trends.

Considering rural areas where connection to the national power grid is impractical, or prohibitively expensive, diesel generator sets are a well-established source of power. However, concerns for the environment, high operation costs owing to expensive fuel and its transport, and high maintenance costs challenge the viability of this option [3]. Rural communities such as these stand to benefit from the use of stand-alone small-scale wind turbines to reduce their dependence on power derived from fossil fuels. Other users who may benefit from the use of small-scale wind turbines include owners of small farms or small-holdings. Their motives for supplementing their energy consumption from the grid may be to save money or simply to reduce their carbon footprint.

Reducing the cost of energy is an important aspect of any energy conversion system, and an efficient and low-cost generator is important in achieving this aim. Researchers are constantly improving generator technologies and investigating different wind turbine topologies with the aim to produce power at the lowest possible cost per unit. This study considers the use of a reluctance synchronous machine (RSM) for use as a generator, termed a reluctance synchronous generator (RSG), in a variable-speed small-scale wind turbine application. RSGs provide a robust, efficient, low cost, and high power density generator option that have potential applications for wind turbines.

CHAPTER 1. INTRODUCTION

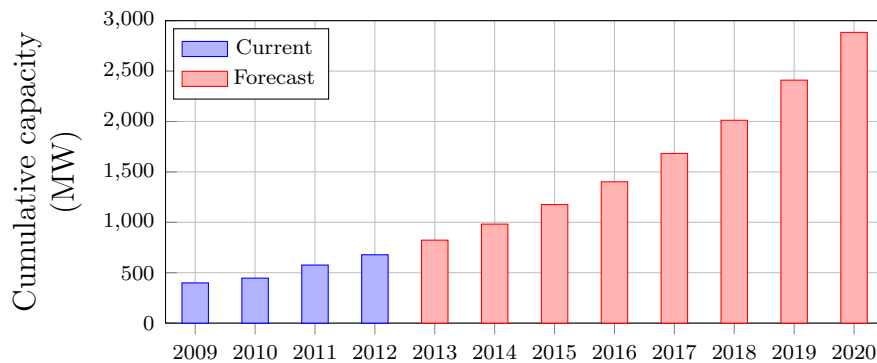


Figure 1.1: Estimated global cumulative installed capacity of small-scale wind turbines [4].

1.1. Small-scale wind turbine topologies

There is no definite power range that describes a wind turbine as being classified as small-scale or otherwise, though the International Electrotechnical Commission (IEC) has defined, in standard IEC 61400-2 [4], the small-scale turbine category as having a rotor swept area less than 200 m^2 , a rated power of around 50 kW , and a generated voltage less than $1000 \text{ V}_{\text{AC}}$ or $1500 \text{ V}_{\text{DC}}$. However, Potgieter [5] considers the power range that classifies small-scale wind turbines to be $1 - 100 \text{ kW}$. The RSM used in this study is rated at 9.2 kW and so the author agrees with the definition by Potgieter. This study, then, focusses on the lower-end of the small-scale turbine range at around 10 kW . This section looks at the typical wind turbine topologies with regards to the small-scale wind turbine category.

1.1.1. Drivetrain topologies

The drivetrain is the mechanical system between the rotor blades (attached to the hub of the turbine) and the generator, and can have a number of different topologies. The topologies discussed are horizontal/vertical axis, geared/direct-drive, and fixed-/variable-speed wind turbine configurations.

A. Horizontal- and vertical-axis wind turbines

A classification of wind turbine topologies may be made according to the axis of rotation of their blades, known as horizontal- (HAWTs) or vertical-axis wind turbines (VAWTs). The difference is illustrated in figure 1.2.

HAWTs are generally able to achieve a higher efficiency from the blades than VAWTs [6]. For this reason, HAWTs are more widespread and commonplace in large utility-scale wind farms, as well for the fact that they are more suited for placement atop tall towers where wind shear is reduced [7]. However, they are dependent on the direction of the wind and thus require mechanisms to orient them into the wind. Larger turbines require active yaw systems which increase the cost and complexity of the turbine. The smaller of the small-scale turbines make use of a simple passive tail-vane system.

CHAPTER 1. INTRODUCTION

VAWTs, however, do have specific advantages. The heavy components such as the gearbox, generator, and control systems are located at the base of the turbine and are thus more suitably placed for access and maintenance. VAWTs operate independently of the wind direction and thus have no need for mechanisms to orient them into the wind, reducing cost and complexity. Low starting wind speed as well as acoustic and aesthetic characteristics add to their advantages [8].

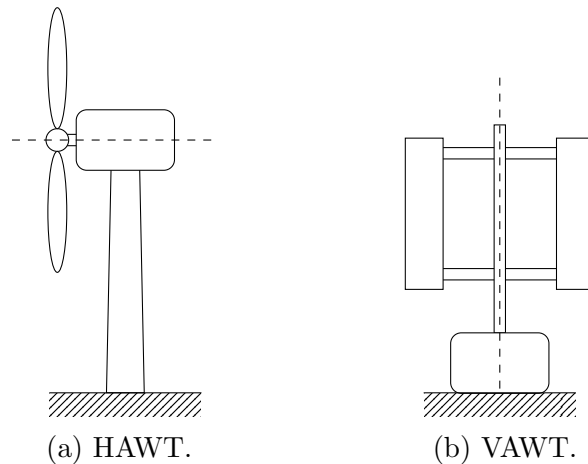


Figure 1.2: Illustration of HAWT and VAWT.

B. Geared and direct-drive topologies

The majority of utility-scale wind turbine designs use a gearbox to increase the slow rotation of the hub to a speed that is more efficient for electrical power production by the generator. Other turbine designs have specially designed slow-speed generators that utilise a direct-drive topology where the generator is coupled directly to the hub and thus operates at the same speed.

There is a notion that gearboxes typically used in wind turbines are unreliable, failure-prone, and the main cause for turbine failures [9, 10]. The addition of a gearbox to a wind turbine is also believed to add weight and cost. However, findings related to utility-scale turbines suggest that a high-speed generator coupled to a three-stage gearbox is the lightest, lowest cost solution when using standard components [10].

A downside to the use of gearboxes is the internal friction from the meshing of the gears. This results in a reduction in power that is transferred to the generator for conversion to electrical power. For this reason, direct-drive wind turbines are considered to be more efficient as losses from the gearbox are omitted. However, the power electronics of the turbine are then required to handle the full power of the turbine, thus shifting the reliability issue from the gearbox to the power electronics [11]. Problematic for direct-drive generators is the increased torque output required, increasing their cost and weight [11].

CHAPTER 1. INTRODUCTION

C. Fixed- and variable-speed operation

It is generally accepted that variable-speed wind turbines exhibit advantages over their fixed-speed counterparts, of which the most touted is their ability to capture more energy from a wider range of wind speeds [12–14]. This is possible as the turbine is able to vary the speed of the blades in accordance with the wind speed so that the blades maintain operation at, or closer to, their peak aerodynamic efficiency. With fixed-speed wind turbines, maximum aerodynamic efficiency can occur only within a small range of wind speeds around the rated wind speed of the turbine.

Variable-speed turbine operation also prevails over fixed-speed with regards to reduced strain on the drivetrain, particularly at above-rated wind speeds [12]. Fixed-speed wind turbines, which typically use direct-grid connected asynchronous generators, are said to have drivetrains that are rigid as very little deviation above rated speed is permitted (limited by the slip rating of the generator) [5]. This means that sudden power peaks, produced from wind gusts, are transmitted through the drivetrain and “absorbed” by the generator. Variable-speed turbines, on the other hand, are able to store excess power from sudden wind gusts by allowing the rotor speed to increase. This mechanically-stored energy is then extracted from the rotor once the gust has passed and the turbine returns to normal operation.

Considered to be somewhat lesser advantages of variable-speed operation is the reduction in noise at lower wind speeds. Power quality is also improved as variable-speed wind turbine operation necessitates the use of electronic power converters which control and condition the power that is fed into the grid [15]. However, while cyclic loading on the drivetrain is reduced as a result of variable-speed operation, it is slightly increased on the tower structure [15]. A drawback to variable-speed turbines is their need for power electronics which add to the cost and reliability of the overall system.

It is difficult to definitively quantify the increase in energy yield of variable-speed over fixed-speed wind turbines. The multitude of topologies between which to compare makes such a comparison cumbersome, even more so as a result of differing wind conditions between sites. At sites where there is little deviation in the wind speed from the average, variable-speed wind turbines gain little over their fixed-speed counterparts as the fixed-speed turbines produce maximum power most of the time anyway.

CHAPTER 1. INTRODUCTION

1.1.2. The generator

This section discusses the two common generator technologies currently used in small-scale wind turbines, that is, the squirrel-cage induction generator (SCIG) and the permanent magnet synchronous generator (PMSG). Table 1.1 presents a summary of the commercially-available HAWT offerings from various manufacturers around the 10 kW output power mark.

Table 1.1: Commercially-available small-scale horizontal-axis wind turbine offerings around 10 kW.

Manufacturer	Model	Power	Generator	Drive	Rotor dia.
Aeolos Wind Turbine [16]	Aeolos-H 10kw	10 kW	PMSG	Direct	8 m
Bergey Windpower [17]	Excel 10	8.9 kW	PMSG	Direct	7 m
Calla Glory [18]	EFD-10KW	10 kW	Induction*	Geared	8 m
Fortis Wind Energy [19]	Alizé	10 kW	PMSG	Direct*	6.9 m
Gaia-Wind [20]	133-11kW	11 kW	Induction*	Geared	13 m
Ghrepower [21]	FD7.5-10/10	10 kW	PMSG	Direct*	7.9 m
Hopeful Wind Energy Technology [22]	H8-10K	10 kW	PMSG	Direct	8 m
Qingdao Windwings Wind Turbine [23]	FZY10KW	10 kW	PMSG	Direct*	7 m
Ventura Wind [24]	VT10-240	10 kW	PMSG	Direct*	6.7 m
WIPO Wind Power [25]	WINForce 10kW	10 kW	PMSG	Direct*	9 m

* Inferred from available data.

A. Squirrel-cage induction generator

The SCIG is a rugged and low maintenance machine on account of its brushless rotor configuration. Its simple construction means it is easier to manufacture than most other generators, therefore reducing its manufacturing costs. The SCIG also has the added benefit of natural protection against short circuits [3].

The SCIG may be operated direct-grid connected or autonomously (self-excited). As the name suggests, the direct-grid connected SCIG is directly connected to the grid with only the need for a soft-starter. The self-excited induction generator (SEIG) uses an external capacitor bank connected to the stator terminals to form a resonant LC circuit that serves to amplify the residual flux in the machine when under operation [2].

SCIGs require a source of reactive power in order to excite the rotor circuit. If directly grid-connected, then this reactive power is taken from the grid which makes the SCIG susceptible to voltage sag, resulting in poor low-voltage ride through (LVRT) capabilities [26]. Therefore, power factor correcting equipment, such as a capacitor bank (the simplest solution), is needed for reactive power compensation [27]. In the case of SEIGs, the existing external capacitor bank supplies the reactive power.

A disadvantage of the SCIG is that the stator windings are required to handle both the active power produced by the energy conversion as well as the reactive power for rotor excitation. This results in higher stator losses and means larger copper cross sections and slot spaces are required in the stator [28]. A further disadvantage of SCIG-based wind turbines is that they generally require a gearbox to increase the rotor speed for more efficient electrical power generation by the generator, adding complexity to the system.

CHAPTER 1. INTRODUCTION

B. Permanent magnet synchronous generator

Currently, the PMSG is the preferred generator topology for small- to medium-scale wind turbines [29]. A review of currently available commercial small-scale wind turbine offerings, summarised in table 1.1, emphasises this paradigm shift.

PMSGs utilise permanent magnets (PMs) on the rotor to supply the flux inside the machine. As with the SCIG, these generators are brushless as well and thus have no maintenance costs associated with brushes and slip-rings. They are thus reliable and compact. Since the flux in the machine is provided internally by the permanent magnets and not “externally” via the stator windings, PMSGs experience better efficiency, improved power factor, and increased power density [29–32]. PMSGs also allow for multi-pole designs that cater for effective low-speed operation and are thus better suited for direct-drive, gearless wind turbine topologies [33]. Furthermore, the cost of the permanent magnet material has been decreasing over the years, making the PMSG an attractive topology particularly for small-scale wind turbines [32].

The active mass of a machine is proportional to its nominal torque output. Since PMSGs are typically used in direct-drive wind turbine topologies, their angular speed is slower and thus must produce a higher torque output in order to produce the same power as a higher-speed generator. This raises their need for active material and thus their mass. Therefore, larger PMSGs become extremely heavy as their power rating increases. They also require fully-rated power converters in order to condition the power before use. There is also the risk of demagnetisation of the permanent magnets if the temperature or current within the machine becomes too high.

1.1.3. Wind turbine control methods

This section discusses some of the common control methods applicable to maximum power capture under variable-speed operation as well as for power capture limiting. A brief description of the regions of operation of an ideal variable-speed wind turbine follows in the next paragraph.

To aid in the description, an example of power versus wind speed curves is plotted in figure 1.3. The curves illustrate the real power of the wind, the theoretical maximum power that can be captured by a wind turbine, and the actual power captured by a turbine. Region 1 is characterised by wind speeds whereby effective power production by the turbine is not possible. In this region, the turbine is in a parked state and monitors the wind speed until conditions are suitable for power production. Region 2 is characterised by wind speeds below the rated wind speed of the turbine but above those of region 1. In this region, the primary goal of the turbine is to extract the maximum amount of energy from the vary wind speed by altering the speed of the rotor to maintain optimal aerodynamic efficiency of the blades. Different algorithms and methods of implementation have been developed to achieve this aim. When the power captured by the turbine begins to exceed the limit of the generator under excessive wind speeds, power limiting techniques need to be employed, which characterise region 3. Finally, when the turbine

CHAPTER 1. INTRODUCTION

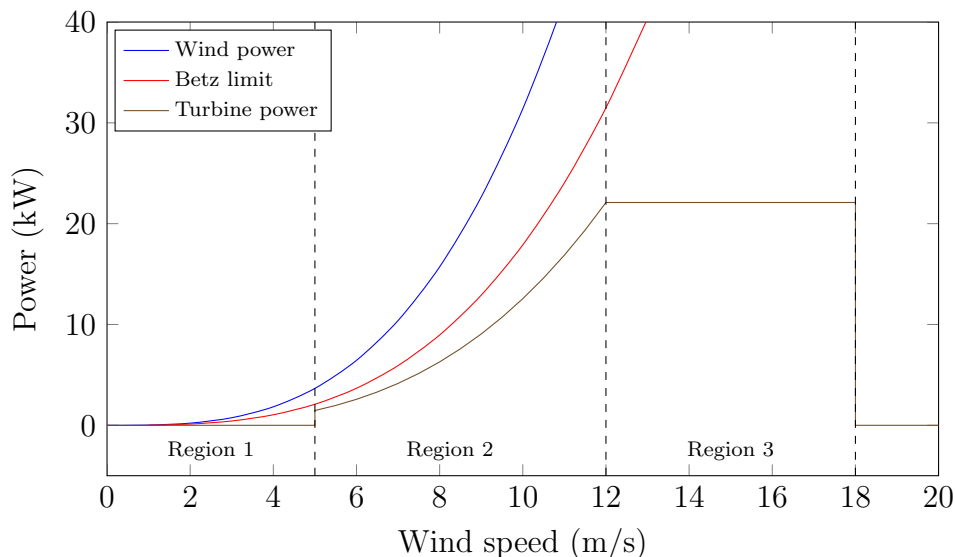


Figure 1.3: Regions of wind turbine operation with curves representing generator power output, the Betz limit, and maximum wind power.

can no longer limit the power to an acceptable limit under extreme wind speeds, it shuts down and ceases power production, returning to the parked state.

A. Region 2 - Maximum power capture

With the advent of variable-speed wind turbines that are capable of operating their rotor blades closer to their peak aerodynamic efficiency across a range of wind speeds, there has been a drive to develop control algorithms with the goal to operate the turbine at its most efficient operating point [34–41]. These control algorithms are classified as maximum power point tracking (MPPT) algorithms. From the literature, three predominant methods of MPPT exist: Tip-speed ratio (TSR) control [42], power signal feedback (PSF) control, and hill-climb searching (HCS) control [38].

MPPT algorithms generally require knowledge of the wind speed and the rotor blade characteristics as input parameters, and thus generally perform well [40]. An MPPT algorithm that requires the aforementioned inputs is known as TSR control. The inputs are used to adjust the rotor speed so as to maintain optimal power coefficient operation of the blades. However, measuring wind speed is problematic as readings from anemometers placed atop nacelles of wind turbines are affected by wake currents from the blades, for both up- and down-wind rotor configurations. Alternatively, anemometers can be placed on meteorological masts situated around the wind turbine. However, this then has the disadvantage that the initial cost of the wind turbine is increased and the value of the measured wind speed does not represent the immediate wind speed present at the hub of the turbine [41].

It is possible to do away with the need for physically measuring the wind speed by means of estimation. In this way, the wind speed is estimated based on other available system measurements. The method proposed by Bhowmik and Spée [43] takes the measured electrical power of the generator and uses the overall efficiency of the system to estimate the aerodynamic power

CHAPTER 1. INTRODUCTION

produced at the hub. The wind turbine aerodynamic power equation along with the tip-speed ratio equation is then used to solve for the wind speed using a polynomial root-finding method. However, mapping efficiency values across all load and speed combinations of the turbine is time-consuming as well as specific to each turbine configuration. Adding to the problem is that the overall efficiency of the system may change over time, impacting the accuracy of the estimation.

Alternatively, the control system may be designed so as not to require knowledge of the wind speed at all [36, 41]. This leads to two different forms of control algorithms, speed and torque control. With speed control, the aerodynamic power at the hub of the turbine is used to determine the optimal speed. Almost conversely, the torque control approach involves measuring the turbine hub speed and controlling the optimal torque reference of the generator. A performance comparison between these two methods of MPPT control is performed by Arnaltes [14] where it is concluded from simulations that the speed control method, although better for fast MPPT response, results in greater output power variation while the torque control method produces smoother power output albeit with a slower MPPT response.

The PSF method also does not require a value for the wind speed in order to operate. It utilises the optimum power versus shaft speed curve of the turbine to determine the optimum power reference signal for the generator. A drawback to this method is that the optimum power curve needs to be generated either by simulation or offline experimentation on individual turbines [44]. This is a timely and expensive procedure, and makes accurate implementation of the system difficult in practice. However, research by Wang and Chang [38] attempts to obtain this power curve characterisation online.

Finally, the HCS method, also known as the perturb-and-observe (P&O) method, requires neither the wind speed nor optimum power curves of the turbine in order to function. This method constantly adjusts the rotor speed and monitors the resulting change in output power produced by the generator. During operation, the rotor speed is increased or decreased by some amount. If the change in output power is favourable for the change in rotor speed, the controller continues increasing or decreasing the rotor speed until no change in output power is detected. However, if a change in rotor speed results in an unfavourable change in output power, the controller reverses the direction of change of the rotor speed such that it will begin increasing it if it was decreasing and vice versa.

The use of artificial intelligence (AI) techniques such as fuzzy logic, artificial neural networks, and genetic algorithms have been proposed in the literature to implement MPPT algorithms. It is noted from the number of papers in the literature, that fuzzy logic appears to be a popular method [32, 35, 45–47]. A reason for interest in these methods of MPPT algorithm implementation is that they do not require an accurate model of the system, thus making them insensitive toward system parameter variations. This is an advantage as parameters of the turbine may change over the course of its lifetime.

CHAPTER 1. INTRODUCTION

B. Region 3 - Power limiting

When the wind speed becomes excessive, the power captured by the turbine needs to be limited in order to protect the generator as well as the power electronics. A number of strategies exist to achieve this goal, namely pitch control, furling, and passive, active, and soft stall.

The simplest form of power limiting is by means of passive stall. It was primarily used on early fixed-speed Danish concept wind turbines because of its mechanical simplicity [5]. The power coefficient curve of the blades is designed in such a way that when the turbine is operating at rated wind speed and thus producing rated power, the blades are on the verge of stalling. Increasing wind speeds, beyond the rated limit, causes the blades to begin stalling gradually along their length starting at the root of the blade [48]. As the blades stall, lift forces are reduced and drag forces are increased, resulting in reduced efficiency and thus reduced power capture. The advantage of the passive stall approach is that the blades are attached to the hub at a fixed angle. Therefore, there is no pitching mechanism and so the turbine is cheaper to manufacture. The downside, however, is that the blades are aerodynamically very complex to design in order to reduce stall-induced vibrations [48].

An improvement to the passive stall power limiting mechanism is active stall where the angle of attack of the rotor blades is able to be adjusted. To achieve this, the blades are able to pivot around their longitudinal axis on the hub of the rotor. There are two closely related forms of active stall known as active stall itself and pitch control. Active stall, also known as pitch-to-stall, involves increasing the blade's angle of attack under excessive wind speeds to induce stalling. On the other hand, pitch control, also known as pitch-to-feather, involves reducing the angle of attack. The end result is that the blades are made to operate less efficiently and thus limit power capture. Active stall allows the turbine to better control the power captured and reduces the overshoot in power capture that occurs with passive stall [48]. However, the need for actuators and control algorithms to manage the pitch of the blades adds to the capital and maintenance costs of the wind turbine. For this reason, active stall is typically reserved for utility-scale wind turbines.

Furling is a power limiting technique predominantly used on small wind turbines whereby the rotor is made to turn away from the wind to reduce the effective wind speed acting on the rotor. Furling may be implemented passively via a tail vane or actively via a yawing mechanism. The main benefit of furling is that it is a simple method for small turbines. However, a problem with furling is that it is possible for the turbine to enter and leave the furled state in a "bang-bang" style. This has implications of fatigue on the turbine as well as ineffective power capture at wind speeds around the furling limit [49]. An additional problem is that the power produced by the turbine at above rated wind speed is not constant but drops abruptly before increasing again with increasing wind speed [50]. Also, turbines operating at high furling angles tend to be noisy [49].

An alternative method to limit power captured for variable-speed, fixed-pitched wind turbines is by means of a method known as soft stall. At high wind speeds, the rotor speed is controlled to induce a specific amount of stall. In doing so, the power coefficient of the blades

CHAPTER 1. INTRODUCTION

can be manipulated depending on the wind speed, thus limiting the power captured. A downside to the soft stall approach is that maintaining constant power capture at above-rated wind speeds results in some parameters of the generator being exceeded. This will be discussed in a later chapter.

1.2. The reluctance synchronous machine

The reluctance synchronous machine (RSM) is amongst one of the oldest electrical machines. Despite this, it has found little practical use in the past as a result of its dismal performance when compared to induction machines (IMs) of the time. It was generally accepted that RSMs had inherently poor power densities and power factors. Indeed, this is true for RSMs designed for and used under open-loop voltage and frequency scenarios. However, RSMs designed for closed-loop current vector control display marked improvement in performance characteristics [51, 52].

RSMs exhibit some notable advantages over induction machines. Vector control is simpler to implement as there are no rotor parameters that need to be identified. If designed properly, the rotor of the RSM experiences almost no losses. This makes cooling of the machine, theoretically, less of a challenge than the induction machine as all losses are located in the stator. Having no rotor windings, and thus no brushes, gives the RSM the same reliability and ruggedness as the induction machine (IM) as well as being simpler to manufacture and thus has cost saving implications. Also beneficial to the cost of the RSM is that the stator is simply that of an induction machine for which there are already well-established production methods [51]. Torque ripple is also minimised compared to double-salient reluctance machines such as the switched reluctance machine (SRM) as the rotating magnetic field allows for smooth torque at low speeds.

The RSM, however, is not without its drawbacks. The improved performance of the machine is only possible with closed-loop current vector control which requires power electronics and accurate sensing of the rotor position via a rotary encoder; this adds to the overall cost and complexity of the system. Like the IM, the RSM also requires a magnetisation current in the stator to create a magnetic field in order to align the rotor. Another downside to RSMs is the poorer power factor, especially when working as a generator [53]. The result of this is the need for a larger capacity converter on account of the higher reactive power, further increasing cost.

Nevertheless, active research is under way to address the disadvantages of the RSM. The power factor of the RSM can be increased by improved design of the rotor to increased its saliency ratio, or by the use of permanent magnets placed within the rotor [54, 55]. The position encoder can also be eliminated by means of rotor position estimation techniques [56, 57].

CHAPTER 1. INTRODUCTION

1.3. Problem statement

There is a constant effort by researchers to find, or develop, generator technologies that will maximise energy yield from a wind turbine while reducing cost and also weight. To this end, a generator topology that exhibits high efficiency and power density is important. The PMSG is a strong contender in this regard, but the future security of the PM resource, and thus its fluctuating price, is a concern.

The RSG exhibits characteristics that are pertinent to wind turbine systems, namely, their efficiency is good and their torque density is higher than that of a similar-sized IG. By using the existing stator of an IG, RSGs are easier to manufacture than IGs and cheaper than PMSGs since they do not require any PM material to operate.

Utilising an RSM as a generator is not a new concept, however, little published literature exists on the use of RSMs as generators specifically in wind turbine applications. Such literature that could be found includes a FEM simulation of an RSG-based wind turbine [58], a report that Sime Motori has designed and produced a few permanent magnet-assisted RSGs (PMA-RSGs) for use in wind turbines [59] (though these are not for small-scale turbines), and an evaluation of a position sensorless RSM wind generator [60].

The primary problem associated with an RSM with regard to its control is the accurate placement of the current vector in relation to the rotor's d-axis. The placement of this vector is essential to optimal operation of the machine. In addition, the speed-control wind speed sensorless MPPT method is considered to be strenuous on wind turbine drivetrains. A control algorithm that reduces drivetrain fatigue while maintaining fast tracking response is important.

1.4. Aim and objectives

The aim of the research is to evaluate the effectiveness of the RSM as a generator, specifically in a wind turbine application. To achieve this aim, the objectives of the study are summarised as follows:

- Mathematically model the operation of the RSM.
- Develop a modular wind turbine simulator, allowing for simple modification of different aspects of the system such as the aerodynamic performance of the blades or electrical characteristic of the generator.
- Develop a MPPT method for wind speed sensorless control with a secondary goal of minimising drivetrain fatigue.
- Design a wind turbine control algorithm to operate the turbine between the modes of operation, as well as current and speed controllers for control of the RSM.
- Validate simulation results on a testbench set-up.

*CHAPTER 1. INTRODUCTION***1.5. Thesis outline**

The remaining contents of the thesis is laid out as outlined below:

Chapter 2: A more in-depth look at the reluctance synchronous machine is presented in this chapter. Factors contributing to differences in performance between motoring and generating are also discussed. Aspects related to the configuration of the turbine considered in the study is covered as well.

Chapter 3: The design of the various controllers used in the complete wind turbine system is presented in this chapter.

Chapter 4: The modelling of each Simulink subsystem block that makes up the complete wind turbine model is covered. The underlying Simulink implementation of each block is also displayed and background information regarding implementation of some blocks is given.

Chapter 5: Results that compare the simulated to the measured results are presented. The simulated results are used to show differences in performance with variations in turbine parameters. Measured results are used to verify the simulation results.

Chapter 6: Finally, conclusions, limitations of the system, and topics for future work are covered in the last chapter.

Chapter 2

RSM-based wind turbine

2.1. The reluctance synchronous machine

2.1.1. Theory of operation

The principle phenomenon behind the operation of an RSM is that of magnetic reluctance. A metal bar placed arbitrarily inside a magnetic field will tend to align itself within the field in an attempt to create a path of minimum reluctance. Should the magnetic field rotate, the metal bar will rotate synchronously with the field; this is the basic functioning of the RSM. The principle operation of an RSM with the simplest rotor design that produces reluctance torque – a two-pole shape resembling a dumb-bell – is illustrated in figure 2.1. It is seen in the figure

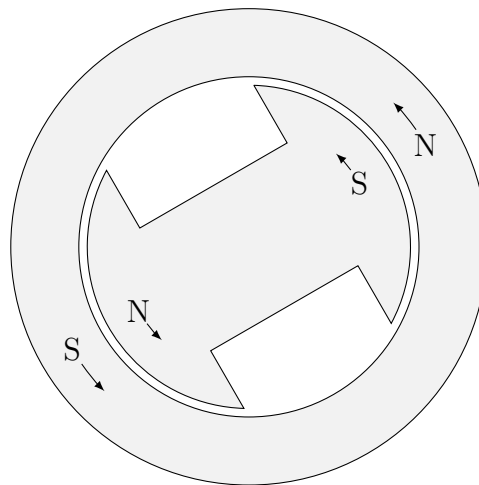


Figure 2.1: Illustration of the simplest form of an RSM rotor, the “dumb-bell”. The rotor resembles that of a wound-rotor synchronous machine, without the field winding.

that the dumb-bell rotor of an RSM resembles that of a wound-rotor of a synchronous machine, but without the field windings. Current applied to the stator windings sets up magnetic poles on the stator. These stator magnetic poles induce opposite poles on the rotor which causes it to align itself with the stator poles. When the current applied to the three-phase windings of

CHAPTER 2. RSM-BASED WIND TURBINE

the stator begins to vary sinusoidally, the stator poles rotate with the field. The induced poles on the rotor cause it to follow the rotating poles of the stator, thus creating torque.

In practical RSMs, however, the aforementioned dumb-bell rotor is not used as its performance is extremely poor. Designing RSM rotors for high performance entails careful positioning of air-filled spaces, known as *flux barriers*, within the rotor to create *flux guides*. This type of RSM rotor is known as an axially-laminated anisotropic (ALA) flux-barrier rotor. These flux barriers and guides serve to minimise the reluctance of the rotor in one direction (or axis) while maximising it in another. With regards to the dq0 reference frame, the axis corresponding to minimum reluctance is known as the *d-axis* of the rotor while the axis of maximum reluctance is the *q-axis*. To illustrate the structure of a typical ALA flux-barrier rotor, a quarter-model of the finite element model of the RSM rotor and stator used in this study is presented in figure 2.2. It may be noticed from the figure that the stator of the RSM is simply that of a three-phase four-pole induction machine though the windings have been chorded.

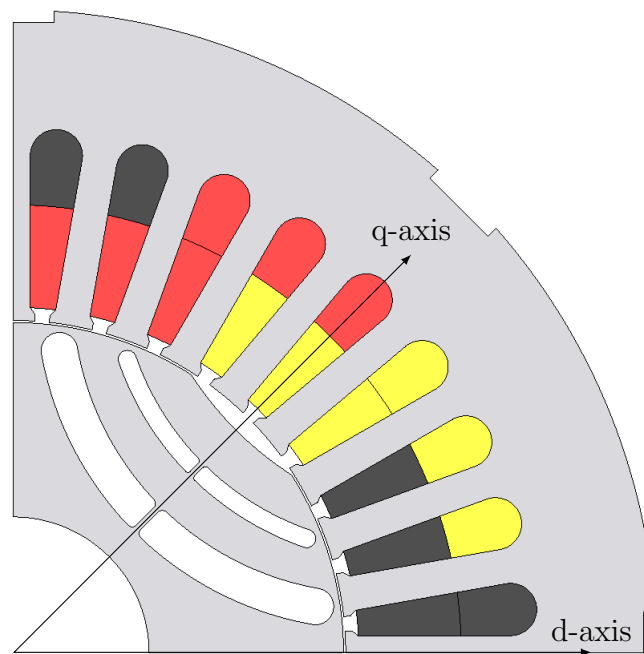


Figure 2.2: Quarter-model of RSM rotor and stator as used in FE analysis.

Table 2.1: Specifications of RSM used in this study.

Parameter	Value	Unit
Current	55.8	A_{peak}
Current angle	67	Degree
Torque	58.1	Nm
Power	9.13	kW
Speed	1500	RPM
Phase resistance	0.15	Ω
Pole pairs	2	-
Saliency ratio	4.63	-

CHAPTER 2. RSM-BASED WIND TURBINE

2.1.2. Modelling the RSM

In order to better facilitate the modelling and control of the RSM, it is beneficial to utilise the dq0 transformation to represent the machine equations in the synchronously-rotating reference frame with respect to the rotor. Since a balanced three-phase system is assumed, the 0-component is zero and may be discarded. The dq voltage equations of the RSM are similar to those of the synchronous machine, except there is no flux-producing component on the rotor of the RSM and so the voltage equations represent only the stator circuit. As a result, the voltage equations of the RSM (excluding the effects of mutual-inductance) can be expressed as [61, 62]

$$u_d = R_s i_d + L'_d \frac{di_d}{dt} - \omega_e \psi_q, \quad (2.1)$$

$$u_q = R_s i_q + L'_q \frac{di_q}{dt} + \omega_e \psi_d, \quad (2.2)$$

where u is the terminal voltage, R_s is the stator resistance, i is current, ω_e is the electrical speed, and ψ is the flux linkage within the machine. Subscripts d and q denote with regards to the d- and q-axes, respectively. The instantaneous self-inductance $L'_{d,q}$ is defined by the equation

$$L'_{d,q} = \frac{\partial \psi_{d,q}}{\partial i_{d,q}}. \quad (2.3)$$

The torque equation of the RSM is given by the equation

$$T_g = \frac{3}{2} p (\psi_d i_q - \psi_q i_d) \quad (2.4)$$

where p is the number of pole pairs present within the machine. Schematic representations of the axis voltage equations of (2.1) and (2.2) are illustrated in figures 2.3a and 2.3b, respectively.

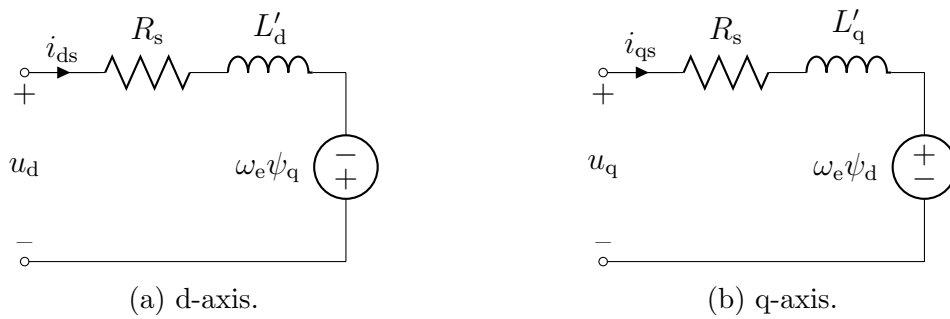


Figure 2.3: Electrical schematic of ideal RSM dq-axis voltage equations.

CHAPTER 2. RSM-BASED WIND TURBINE

A. Core losses

The alternating flux in the core of the machine causes losses in the iron as a result of hysteresis losses and eddy currents. This iron loss manifests itself as an equivalent resistor R_c across the magnetising branches of the dq-axis equivalent electrical circuits, shown in figure 2.4. The core loss resistance R_c creates an additional current path, allowing current to be diverted from the magnetising branches.

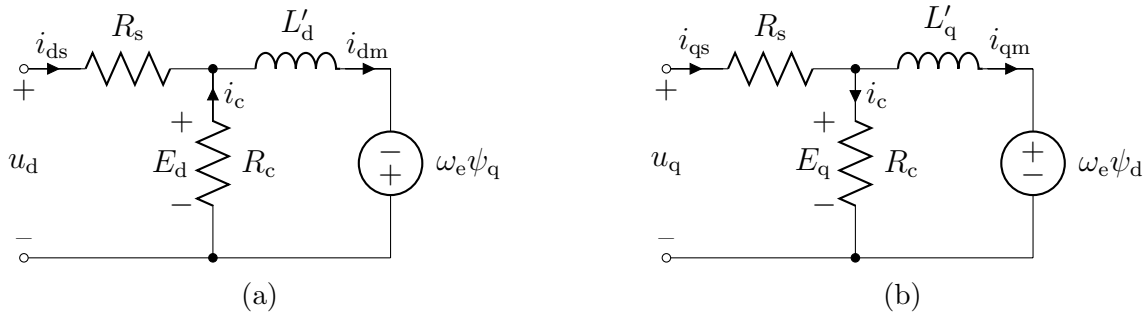


Figure 2.4: Electrical model of RSM incorporating stator core losses represented by R_c .

The effect of the core loss resistance on the angle of the resulting magnetising current i_m acting upon the rotor is seen in the phasor diagrams of figure 2.5. In the theoretical case where core losses are not present, $R_c \rightarrow \infty$ and $i_m = i_s$. It is seen in the figure that the core losses serve to reduce internal current angle when motoring and increase it when generating. This has implications for performance which will be shown later.

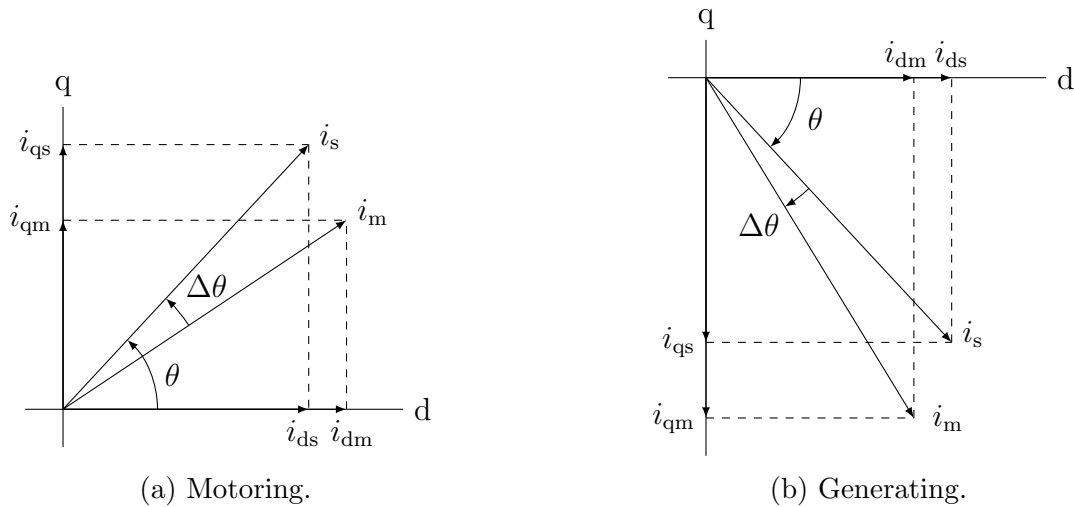


Figure 2.5: Phasor diagrams illustrating shift in stator current vector as a result of core losses in an RSM for (a) motoring and (b) generating [53].

CHAPTER 2. RSM-BASED WIND TURBINE

2.1.3. Generating power with the RSM

When operating as a motor, the current vector is placed ahead of the rotor's d-axis as shown in figure 2.6a. That is, the current vector, as well as the magnetising flux vector ψ_m , leads the rotor and thus acts to pull the rotor in the direction of rotation (counter-clockwise). Quadrant 1 is thus motoring operation when the current vector is located in that quadrant. For the same direction of rotation, generating mode is achieved by placing the current vector, and thus the flux vector, behind the rotor. That is, the flux vector lags the rotor as illustrated in quadrant 4 of figure 2.6b and the torque produced is negative.

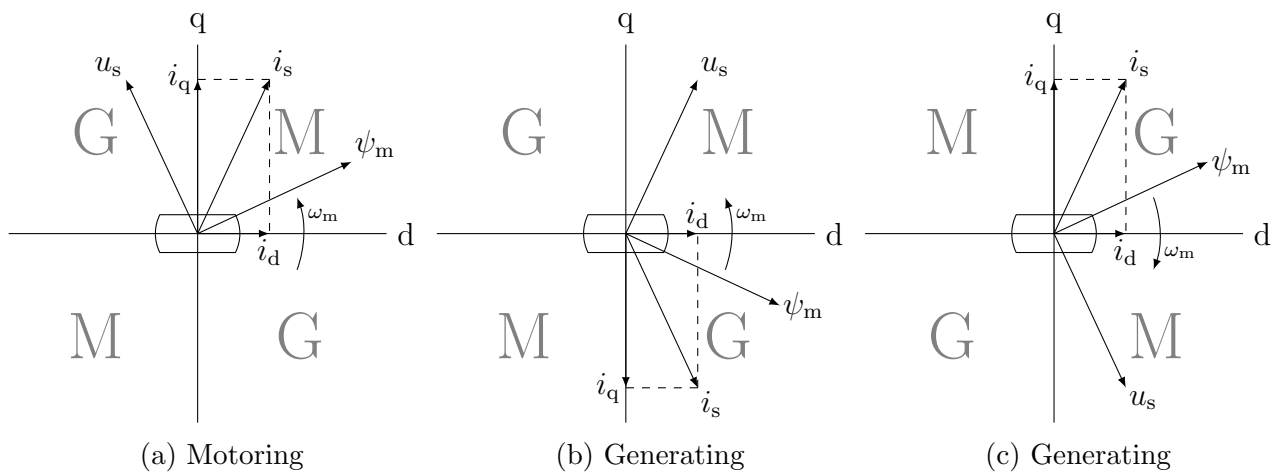


Figure 2.6: Phasor diagrams demonstrating the voltage, current, and flux vectors within an RSM for motoring and generating operation.

When the direction of rotation of the machine is reversed, so are the modes of operation in the different quadrants. Quadrant 1 thus becomes generator mode since the current vector now lags the rotor in this quadrant and leads in quadrant 4. Figure 2.6c represents the configuration of the current vector angle and direction of rotor rotation for the RSM used in this study.

CHAPTER 2. RSM-BASED WIND TURBINE

2.1.4. Parameter values

A. Flux linkage

The d- and q-axis flux linkage magnitudes of the RSM used in this study for current angles of 0° (no q-axis flux), 90° (no d-axis flux), and 65° (rated current angle) are plotted in figure 2.7. The two figures of figure 2.7 essentially represent the same information, however, figure 2.7a plots the axis flux magnitudes against the axis current magnitude while 2.7b plots the same axis flux magnitudes against the stator current magnitude.

The dq-axis flux magnitude plots at 65° of figure 2.7a cannot be compared against one another directly. Doing so would mean that the current in both axes is the same, resulting in a current angle of 45° being considered which is not the current angle of the plotted flux linkage. Figure 2.7b allows for a comparison of the 65° current angle flux magnitudes as the flux magnitude plotted for each axis for a particular stator current magnitude takes into account the reduction in axis current as a result of the current angle.

From figure 2.7a, the demagnetising effect on one axis as a result of flux present in the other axis can be seen; this is a result of the cross-coupling present between the axes. In fact, above 40 A of d-axis current and the d-axis flux magnitude begins to decrease. In both figures of figure 2.7, the d- and q-axis flux linkages at 0° and 90° current angles, respectively, are the same as the stator current is the entire axis current in these two instances.

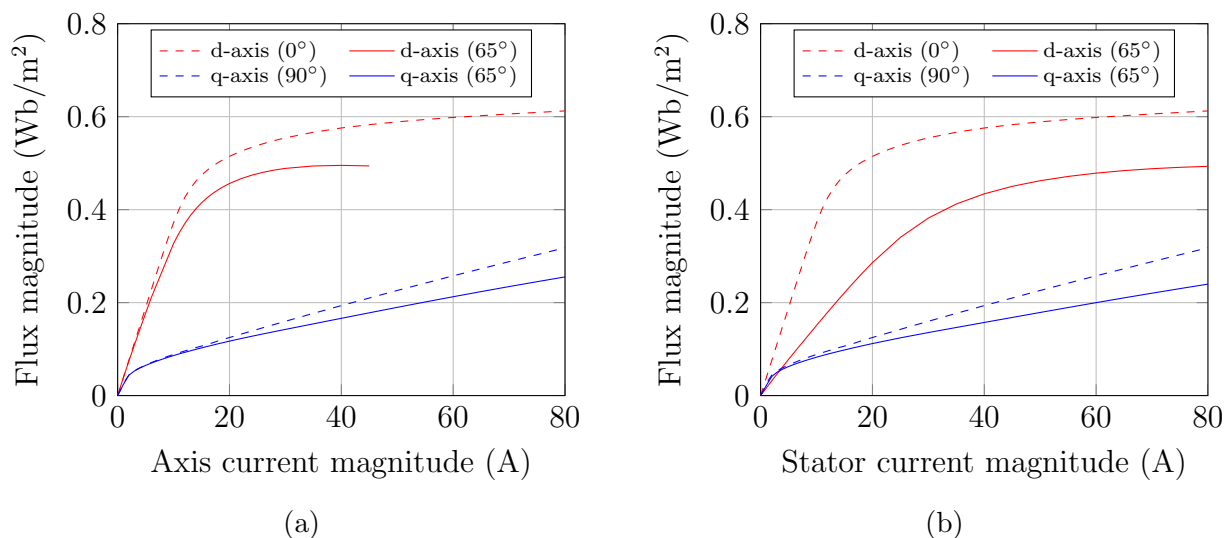


Figure 2.7: Flux linkages for 0° (no q-axis flux), 90° (no d-axis flux), and 65° current angles plotted against (a) axis current and (b) stator current magnitudes for the dq-axes.

From figure 2.7a, it can be seen that the minimal iron present in the q-axis flux path of the rotor saturates at very low current values – roughly 2 A. The d-axis, on the other hand, exhibits a slightly larger linear flux magnitude range owing to the increased amount of magnetic material present d-axis flux path of the rotor. Even so, the d-axis of the machine begins saturating after roughly 12 A. It should be noted that all current values in this study represent peak values and not RMS values.

CHAPTER 2. RSM-BASED WIND TURBINE

B. Linear inductance

Linear inductance is defined by the equation

$$L_{d,q} = \frac{\psi_{d,q}}{i_{d,q}}. \quad (2.5)$$

The linear inductance plots of figure 2.8 are produced by applying (2.5) to the flux linkage magnitude plots of figure 2.7.

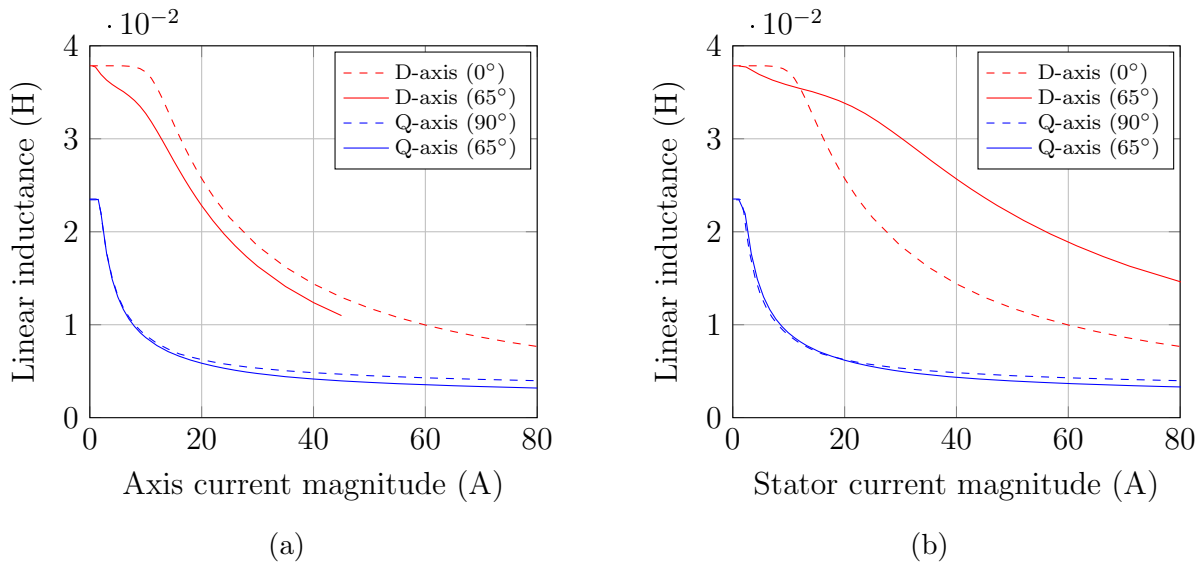


Figure 2.8: Linear inductances for 0° (no q-axis flux), 90° (no d-axis flux), and 65° current angles plotted against (a) axis current and (b) stator current magnitudes for the dq-axes.

The demagnetising effect from the axis cross-coupling on the inductance of the RSM is seen in figure 2.8a. As expected from the reduction in axis flux linkage in figure 2.7a and (2.5), the dq-axis linear inductances at 65° are lower than the linear inductances at 0° and 90° .

When plotting the linear inductance of the axes against the stator current magnitude in figure 2.8b, less change is seen in the q-axis as opposed to the d-axis. The d-axis linear inductance magnitude plot at 65° current angle is greater than the plot at 0° current angle. This is a result of the d-axis current magnitude increasing at a lower rate than the q-axis current magnitude for increasing stator current magnitude. Even though the 65° flux magnitude plot is lower than the 0° plot as a result of cross magnetisation, the lower d-axis current as a result of the 65° current angle causes a larger d-axis linear inductance.

CHAPTER 2. RSM-BASED WIND TURBINE

C. Instantaneous inductance

As defined before in (2.3), the instantaneous inductance equation is repeated for convenience,

$$L'_{d,q} = \frac{\partial \psi_{d,q}}{\partial i_{d,q}}. \quad (2.6)$$

The graphs of figure 2.9 plot the instantaneous inductances of the RSM in the same manner as the linear inductances of figure 2.8.

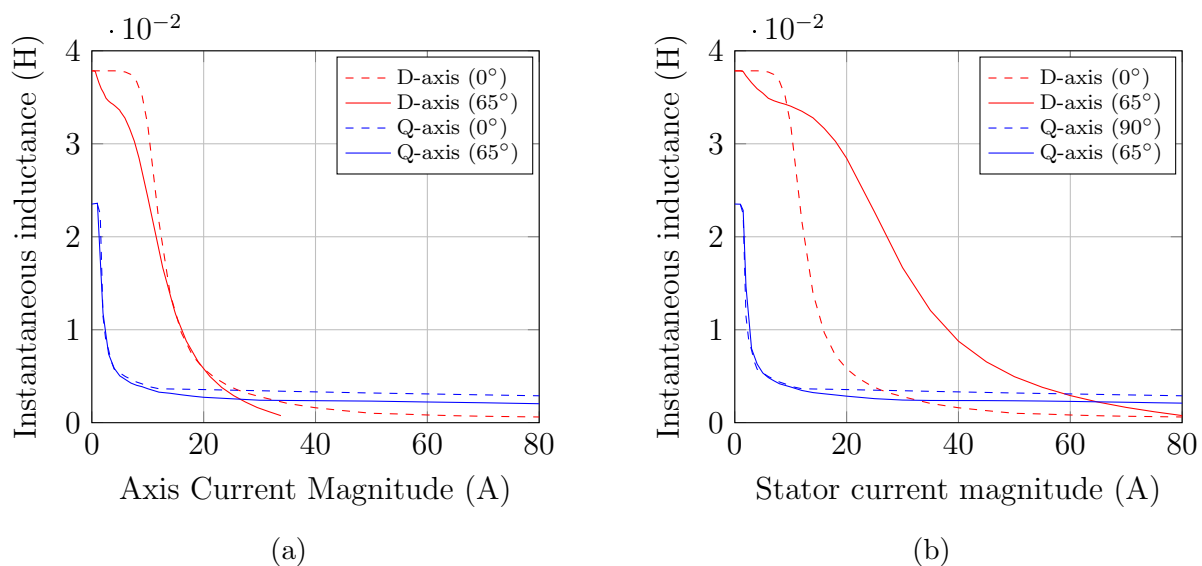


Figure 2.9: Instantaneous inductances for 0° (no q-axis flux), 90° (no d-axis flux), and 65° current angles plotted against (a) axis current and (b) stator current magnitudes for the dq-axes.

2.1.5. Performance data

In order to obtain the measured results presented in this section, a testbench is set up. The testbench comprises an IM and the RSM under test connected to each other via a torque sensor. The IM is controlled to maintain a constant speed while the current magnitude of the RSM is altered and the results from the torque sensor recorded.

A. Current magnitude

In figure 2.10, the current magnitude required by the RSM to output rated torque, 60 Nm, for both motoring and generating modes is plotted. It is quite peculiar that in the figure it is seen that the current magnitude when generating is less than motoring for current angles below rated (65°). The reverse occurs for current angles above rated.

This peculiarity is attributed to iron losses and may be explained with the help of figure 2.5. For a particular angle of the stator current i_s , the angle of the magnetising current i_m in relation to the rotor is smaller than i_s when motoring but larger when generating. The implication of this is that when operating at smaller current angles, the angle of i_m is further away from the

CHAPTER 2. RSM-BASED WIND TURBINE

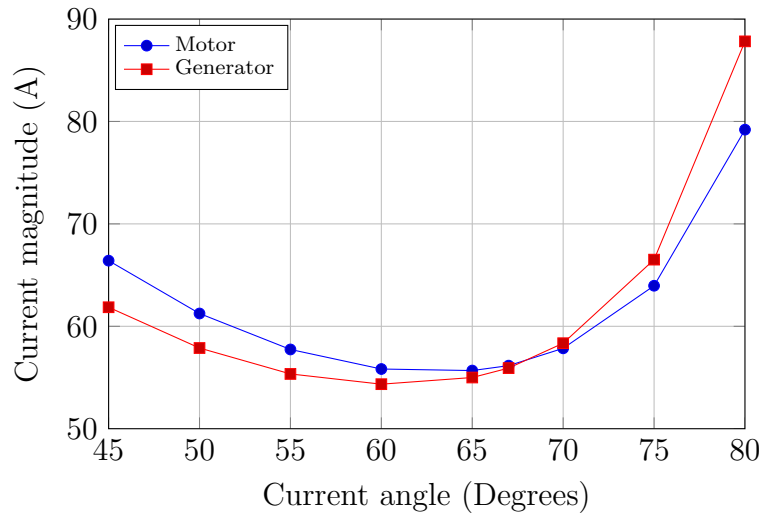


Figure 2.10: Measured current magnitude versus current angle for motoring and generating modes. Measurements performed at rated speed and torque [53].

optimal value than i_s when motoring which degrades performance, requiring increased stator current magnitude. When generating, the angle of i_m is in fact closer to the optimal angle than i_s and so performance is improved.

On the other hand, when operating at larger current angles, the effect is reversed. The increased angle of i_m means it is further away from optimal than i_s when generating and so performance is hindered. Conversely for motoring, the smaller-than- i_s angle of i_m means it is closer to the optimal angle and so performance is enhanced, reducing the required stator current magnitude.

B. Efficiency

The efficiency values of the RSM for motoring and generating are plotted against current angle in figure 2.11. The efficiency of the RSM is acquired by measuring the ratio of the mechanical power at the shaft to the electrical power at the terminals.

The efficiency between motoring and generating matches closely until about 65° current angle where the generating efficiency begins dropping off faster than motoring efficiency with increasing current angle.

CHAPTER 2. RSM-BASED WIND TURBINE

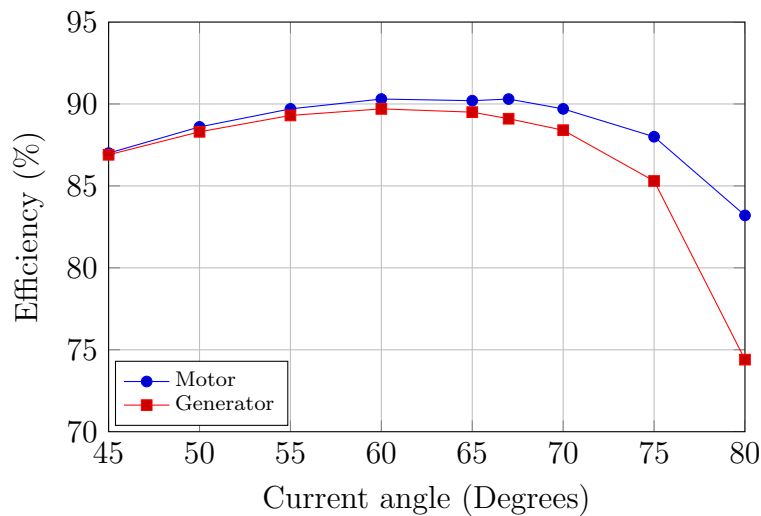


Figure 2.11: Measured efficiency versus current angle for motoring and generating modes. Measurements performed at rated speed and torque [53].

C. Power factor

Using a power analyser, the power factor of the RSM is measured and plotted against current angle in figure 2.12. It is seen in the figure that the power factor of the RSM as a generator is lower than as a motor for all current angles. This agrees with the suggestion made by Boldea [63] that the maximum power generating factor of an RSM is lower than motoring.

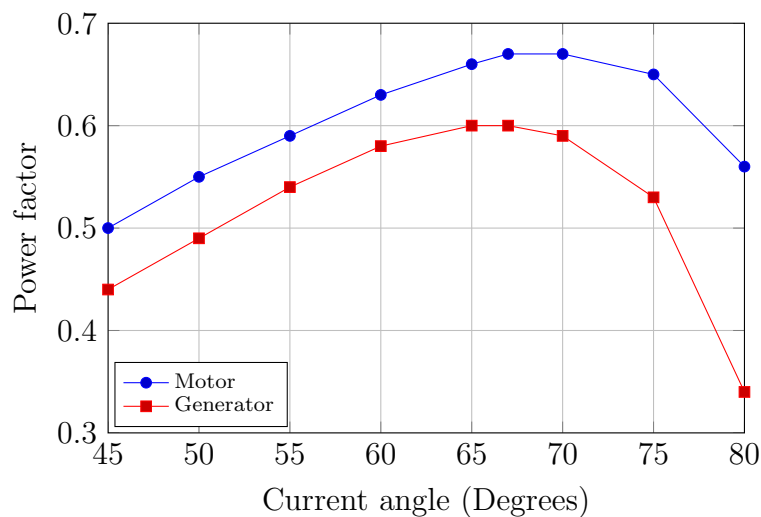


Figure 2.12: Measured power factor versus current angle for motoring and generating modes. Measurements performed at rated speed and torque [53].

CHAPTER 2. RSM-BASED WIND TURBINE

2.2. The wind turbine

This section provides some information regarding the rest of the wind turbine system around which the study is based.

2.2.1. Turbine blades

The turbine blades considered for this study is a horizontal-axis three-bladed set with a diameter of 7.2 m. The power curves of the blades is plotted in figure 2.13. Given that the rated power of the RSM is 9.2 kW, it is seen from the figure that the rated wind speed for the wind turbine should be 9 m/s.

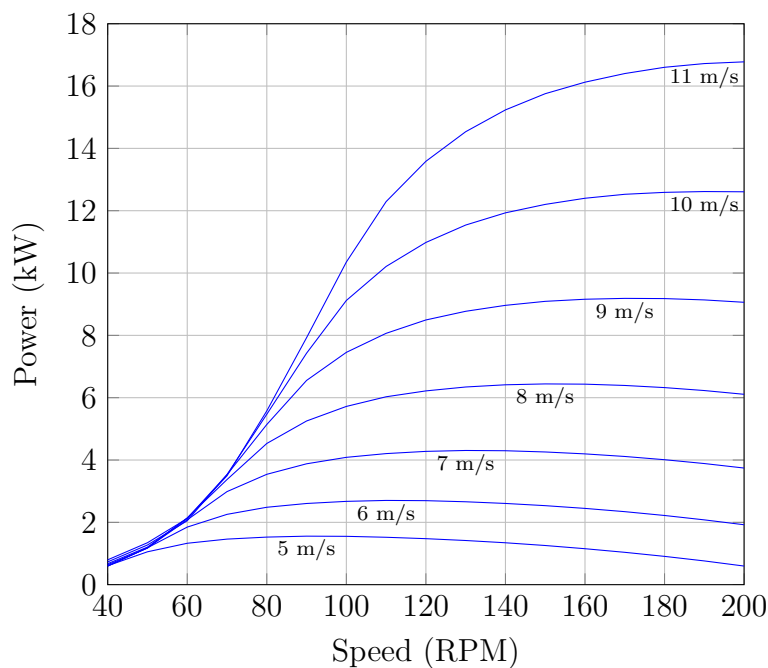


Figure 2.13: Power curves for the blade set used in the study.

2.2.2. Gearbox ratio

The RSM used in the study is a high speed machine, therefore the speed of the turbine rotor needs to be increased by means of a gearbox for effective power production. The rated speed of the generator is 1500 RPM and the speed of the rotor blades at which the generator's rated power is produced is 170 RPM, giving a gear ratio of $n_g = 8.82$. This gear ratio, however, does not multiply the generator's torque output enough to allow it to easily maintain the speed of the system in the event of a wind gust; the torque produced by the blades can easily overpower the generator. For this reason, a larger gear ratio is considered. In this study, a number of gear ratios are evaluated to determine the effect on the turbine system with the ratios considered being $n_g = 10 - 15$.

Chapter 3

Design of wind turbine controllers

In the design of the wind turbine control system, it is decided that three individual controllers will be designed: the current controller, the speed controller, and the wind turbine system controller.

3.1. Current controller

The current controller is responsible for supplying the RSM with the necessary stator voltages in order to effect the reference current magnitude and angle within the stator. The design of the current controller is based on the machine voltage equations of (2.1) and (2.2). However, the effects of cross-coupling between the dq-axes needs to be considered to effectively design the controller. The axis voltage equations, modified to include the effects of mutual-inductance, are known as the non-ideal voltage equations and can be expressed as [61]

$$u_d = R_s i_d + L'_d \frac{di_d}{dt} + M'_d \frac{di_q}{dt} - \omega_e \psi_q, \quad (3.1)$$

$$u_q = R_s i_q + L'_q \frac{di_q}{dt} + M'_q \frac{di_d}{dt} + \omega_e \psi_d, \quad (3.2)$$

where $L'_{d,q}$ is the instantaneous self-inductance defined as

$$L'_d = \frac{\partial \psi_d}{\partial i_d}, \quad L'_q = \frac{\partial \psi_q}{\partial i_q}, \quad (3.3)$$

and $M'_{d,q}$ is the instantaneous mutual inductance defined as

$$M'_d = \frac{\partial \psi_d}{\partial i_q}, \quad M'_q = \frac{\partial \psi_q}{\partial i_d}. \quad (3.4)$$

From the equations of (3.1) and (3.2), it is apparent that one of the problems in designing the current controller is that each axis voltage equation contains terms that are dependent on the other axis. For this reason, the axis voltage equations are coupled and thus need to be decoupled in order to more easily facilitate the design of the current controller.

CHAPTER 3. DESIGN OF WIND TURBINE CONTROLLERS

3.1.1. Decoupling the voltage equations

In order to visualise the cross-coupling present in the electrical model of the RSM, a block diagram representation of equations (3.1) and (3.2) is illustrated in figure 3.1. The decoupling

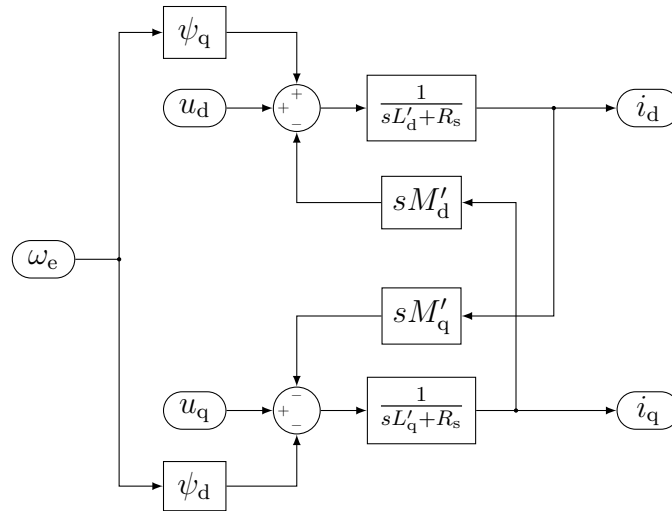


Figure 3.1: Block diagram of RSM electrical model demonstrating the cross-coupling present between the two axes.

procedure followed, as well as the design of the controller, is that developed by de Kock [61]. The method subtracts the speed-dependent and mutual inductance voltages in the controller where they are added in the machine and adds them where they are subtracted. Figure 3.2 illustrates the principle of the decoupling method, again in the form of a block diagram. The

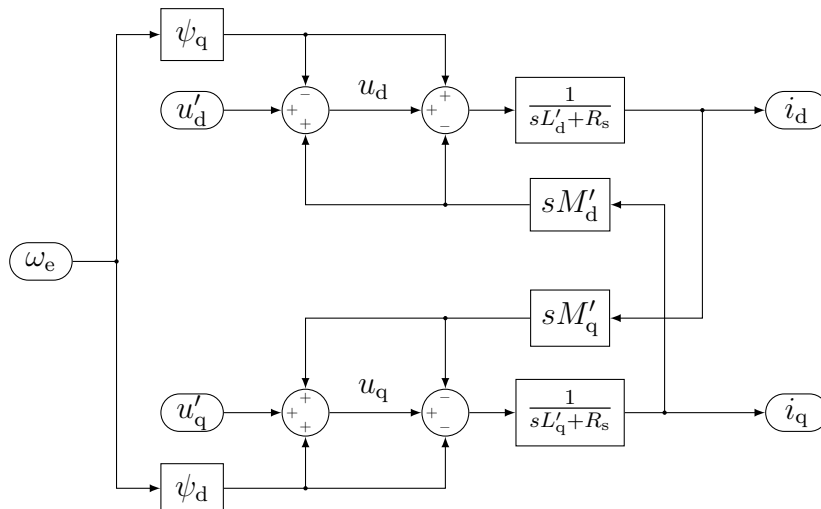


Figure 3.2: Block diagram of RSM electrical model demonstrating the decoupling procedure used.

resulting decoupled differential equations are finally presented by the block diagrams in figure 3.3. The controller for each axis can now be designed individually. The voltages u'_d and u'_q are the compensated control voltages produced by the current controller to be applied to the RSM.

CHAPTER 3. DESIGN OF WIND TURBINE CONTROLLERS

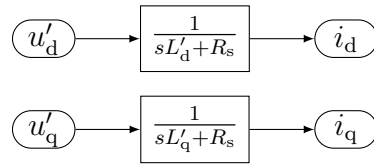


Figure 3.3: Equivalent machine block model after decoupling procedure.

3.1.2. Zero-order hold

In practice, the current controller is implemented digitally and as such does not produce a continuous output signal. In order to interface the digital controller to the analogue plant, digital-to-analogue (DAC) and analogue-to-digital converters (ADC) are necessary. Designs that require high bandwidth, such as the current controller, require the delay effects introduced by the DAC to be taken into account in the design of the controller.

The ADC of the current controller receives a continuous signal as input from the current sensor. This value is sampled at the sampling rate and stored in a buffer with a finite number of bits. The ADC is thus a sampler followed by a quantiser. On account of the quantiser possessing a finite number of bits, only a finite number of values exist to represent the real input. For this reason, the sampled value will not equal the real value exactly and the error depends on the number bits used to represent the number digitally. It is assumed that the time required to sample the input into the buffer is much smaller than the sampling period and that the error because of the quantiser is negligible.

The DAC converts the digital representation of the control voltage u'_{dq} to a continuous signal, with the zero-order hold (ZOH) function being the simplest to achieve this. The value at the input of the ZOH is maintained at its output and is updated only at each sampling instant. In order to include the effects of the ZOH in the system, it may be combined with the plant model and then both transformed to the discrete Z-plane using the equation [61]

$$G(z) = (1 - z^{-1})\mathcal{Z}\left[\frac{G(s)}{s}\right] \quad (3.5)$$

where $G(z)$ is the equivalent plant in the Z-domain including the effects of the ZOH, $\mathcal{Z}[\]$ is the Z-transform operator, and $G(s)$ is the continuous domain plant. To be noted from (3.5) is the addition of a pole to the plant, as well as a time delay.

The transformation above leads to a control system that is represented completely in the Z-plane. It is preferred to design a controller completely in the Z-plane instead of the S-plane as the delay introduced by the ZOH can be included in the system design. However, the system representation can be transformed yet again to the W-plane where frequency response techniques can be used and allows the use of Bode plots to visualise the system response.

For a sampling frequency f_s , input signals with a frequency less than $\frac{f_s}{2}$ (the Nyquist frequency) can be recreated faithfully from the samples. The single pole of the plant (visible in figure 3.3) introduces a 90° phase delay while the ZOH introduces a further 90° phase delay at $\frac{f_s}{2}$. Therefore, at $\frac{f_s}{2}$ there will be a combined phase delay of 180° . Should the loop gain of the system be 1, or 0 dB, at $\frac{f_s}{2}$, then instability will occur since the closed-loop response is defined

CHAPTER 3. DESIGN OF WIND TURBINE CONTROLLERS

by

$$\frac{1\angle 180^\circ}{1 + 1\angle 180^\circ} = \frac{1}{0} = \infty \quad (3.6)$$

To ensure stability of the controller, the loop gain is chosen to be -10 dB at $\frac{f_s}{2}$; the gain margin thus will be 10 dB.

3.1.3. Closed-loop model

The design of the current controller begins with the decoupled continuous-domain S-plane plant model. The d-axis model of the RSM plant is arbitrarily chosen to demonstrate the design process and is given by

$$G_d(s) = \frac{1}{sL'_d + R_s}. \quad (3.7)$$

Utilising the transform of (3.5), the continuous S-plane representation of the plant, including the effects of the ZOH, is transformed to the discrete Z-plane representation:

$$G_d(z) = (1 - z^{-1})\mathcal{Z}\left[\frac{G_d(s)}{s}\right] \quad (3.8)$$

$$= \left(\frac{z-1}{z}\right)\mathcal{Z}\left[\frac{1}{s}\frac{1}{sL'_d + R_s}\right] \quad (3.9)$$

$$= \left(\frac{z-1}{z}\right)\left(\frac{1}{R_s}\right)\mathcal{Z}\left[\frac{\frac{R_s}{L'_d}}{s\left(s + \frac{R_s}{L'_d}\right)}\right]. \quad (3.10)$$

The Z-transform is achieved through the use of a Z-transform table. The time-domain, S-domain, and Z-domain transform pairs are presented in table 3.1 below for ease of reference.

Table 3.1: Z-transform pairs.

$f(t), t \geq 0$	$F(s)$	$F(z)$
$1 - e^{-at}$	$\frac{a}{s(s+a)}$	$\frac{z(1-e^{-aT_s})}{(z-1)(z-e^{-aT_s})}$

The Z-transform can then be carried out, resulting in the equation

$$G_d(z) = \frac{1}{R_s}\left(\frac{z-1}{z}\right)\left(\frac{z\left(1 - e^{-\frac{R_s T_s}{L'_d}}\right)}{(z-1)\left(z - e^{-\frac{R_s T_s}{L'_d}}\right)}\right) \quad (3.11)$$

$$= \frac{1 - e^{-\frac{R_s T_s}{L'_d}}}{R_s\left(z - e^{-\frac{R_s T_s}{L'_d}}\right)}. \quad (3.12)$$

A sampling period T_s is needed in order to complete the transformation. The smaller the sampling period, the closer the approximation of the Z-plane representation to the S-plane model. There is, however, a limit to the maximum sampling rate $f_s = \frac{1}{T_s}$ that may be chosen

CHAPTER 3. DESIGN OF WIND TURBINE CONTROLLERS

which is imposed by the maximum switching capability of the variable-speed drive (VSD) as well as the processing speed of the digital controller. The sampling rate is set to be 10 kHz which results in a switching frequency of the VSD of 5 kHz. This equates to a sampling period of $T_s = 100 \mu\text{s}$.

Next, the W-transform is used to transform the discrete Z-plane transfer function back to an equivalent continuous domain. It is a bilinear transformation and is therefore an accurate mapping between the discrete and continuous domains [61]. The equation for the W-transform is given by

$$z = \frac{1 + \frac{T}{2}w}{1 - \frac{T}{2}w}. \quad (3.13)$$

Substituting (3.13) into (3.12) results in the transformation of the discrete Z-plane plant transfer function to the continuous W-domain. The equation is given by

$$G_d(w) = \frac{1 - e^{-\frac{R_s T_s}{L'_d}}}{R_s \left(\frac{1 + \frac{T_s}{2}w}{1 - \frac{T_s}{2}w} - e^{-\frac{R_s T_s}{L'_d}} \right)}. \quad (3.14)$$

Since the W-plane is a continuous frequency-domain representation, it could just as well be represented by the letter s . However, the variable w is maintained to remind of the fact that the frequency axis of the W-plane is distorted. In order to evaluate the W-plane plant transfer function at the Nyquist frequency, w is set to ∞ in (3.14), thus

$$G_d(\infty) = \frac{1 - e^{-\frac{R_s T_s}{L'_d}}}{R_s \left(\frac{1 + \frac{T_s}{2}\infty}{1 - \frac{T_s}{2}\infty} - e^{-\frac{R_s T_s}{L'_d}} \right)}, \quad (3.15)$$

$$= \frac{1 - e^{-\frac{R_s T_s}{L'_d}}}{R_s \left(-1 - e^{-\frac{R_s T_s}{L'_d}} \right)}. \quad (3.16)$$

In order to maintain fast response of the current controller, it is chosen that a proportional-only controller will be used. Thus, there is only one gain variable which needs to be calculated, k_{cc-d} . In order to achieve the loop gain of -10 dB at the Nyquist frequency, the gain of k_{cc-d} is calculated as follows:

$$20 \log_{10} \left(k_{cc-d} \left| \frac{1 - e^{-\frac{R_s T_s}{L'_d}}}{R_s \left(-1 - e^{-\frac{R_s T_s}{L'_d}} \right)} \right| \right) = -10. \quad (3.17)$$

CHAPTER 3. DESIGN OF WIND TURBINE CONTROLLERS

The equation is rearranged to solve for k_{cc-d} so that

$$k_{cc-d} = 10^{-\frac{10}{20}} \left| \frac{R_s \left(-1 - e^{-\frac{R_s T_s}{L'_d}} \right)}{1 - e^{-\frac{R_s T_s}{L'_d}}} \right| \quad (3.18)$$

$$= 10^{-\frac{10}{20}} R_s \frac{1 + e^{-\frac{R_s T_s}{L'_d}}}{1 - e^{-\frac{R_s T_s}{L'_d}}} \quad (3.19)$$

$$= 10^{-\frac{10}{20}} R_s \coth\left(\frac{R_s T_s}{2L'_d}\right) \quad (3.20)$$

$$= \frac{10^{-\frac{10}{20}} R_s}{\tanh\left(\frac{R_s T_s}{2L'_d}\right)} \quad (3.21)$$

Evaluating (3.21) for the RSM at rated conditions of $R_s = 150 \text{ m}\Omega$ and $L'_d = 3.807 \text{ mH}$ with $T_s = 100 \text{ }\mu\text{s}$ results in the d-axis current controller gain being

$$k_{cc-d} = \frac{10^{-\frac{10}{20}} \cdot 0.15}{\tanh\left(\frac{0.15 \cdot 100 \cdot 10^{-6}}{2 \cdot 3.807 \cdot 10^{-3}}\right)} \quad (3.22)$$

$$= 24.078 \quad (3.23)$$

For the aforementioned rated conditions of the RSM's decoupled d-axis plant, figure 3.4 graphs the Bode plot of the open-loop and scaled responses. It is seen that the gain, and thus performance of the plant, is increased at lower phase angles while the gain margin of 10 dB is achieved at 180° of phase shift, ensuring stability.

Likewise, with $L'_q = 2.331 \text{ mH}$ at rated conditions, the q-axis current controller gain is calculated to be

$$k_{cc-q} = 14.743 \quad (3.24)$$

With reference to figure 2.9b, it must be noted that the inductances of the two axes do not remain constant with changes in current magnitude on account of saturation and cross-coupling present in the core of the machine. Since the q-axis flux path is predominantly air, the q-axis inductance is considerably constant for a wide range of stator currents as plotted in figure 2.9b. For this reason, the current controller's q-axis gain k_{cc-q} may be computed only once. However, the d-axis inductance exhibits a more significant change in inductance over the entire stator current range of the RSM. It is thus necessary that the d-axis current controller gain k_{cc-d} not be static. Values of k_{cc-d} are calculated for a number of d-axis current magnitudes and stored in an LUT, ensuring the current controller remains stable for all current values. A graph illustrating the change in k_{cc-d} versus d-axis current is plotted in figure 3.5.

CHAPTER 3. DESIGN OF WIND TURBINE CONTROLLERS

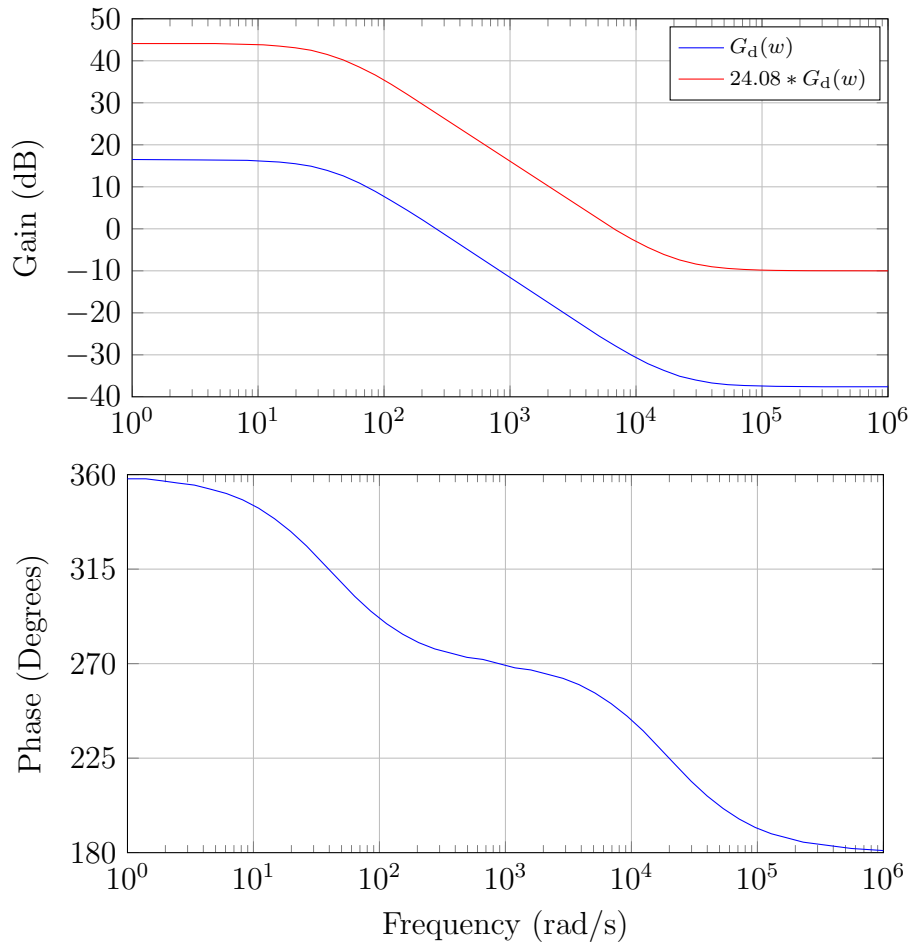
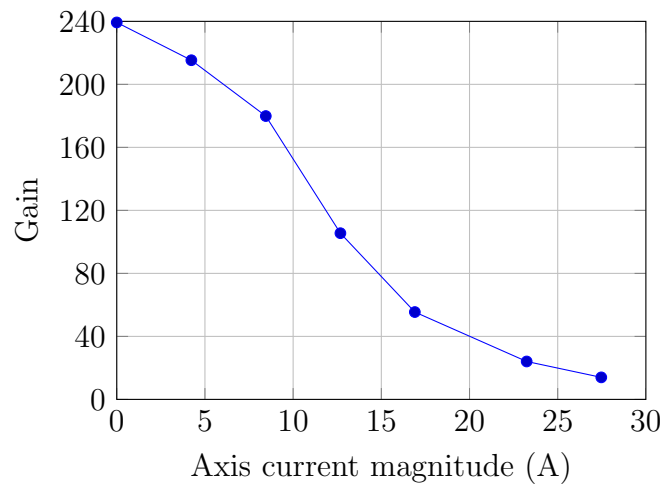


Figure 3.4: Open-loop and gain-scaled responses of RSM d-axis plant.

i_d	k_{cc-d}
0.0	239.302
4.23	215.313
8.45	179.877
12.68	105.513
16.90	55.454
23.24	24.078
27.47	13.990


 Figure 3.5: Gain scheduled values for d-axis current controller k_{cc-d} .

3.2. Speed controller

The speed controller produces a current reference value for the current controller from the speed reference that it receives as input.

3.2.1. Open-loop model

The mechanical system of the wind turbine system can be modelled as a simple first-order system. To simplify the model further, the drivetrain shafts are assumed to be rigid with no spring component. The equation of the open-loop mechanical system is given by the equation

$$n_g T_g = T_a - J_{\text{eq-t}} \dot{\omega}_t - B_{\text{eq-t}} \omega_t \quad (3.25)$$

where n_g is the gearbox ratio, T_g is the reaction torque produced by the generator, ω_t is the angular speed and $\dot{\omega}_t$ is the angular acceleration of the turbine hub, T_a is the aerodynamic torque produced by the turbine blades, and $J_{\text{eq-t}}$ and $B_{\text{eq-t}}$ are the equivalent system inertia and friction coefficients, respectively, referred to the turbine side. It is possible to relate the generator torque to the stator current by the follow function

$$T_g = K_t(i_s) \cdot i_s \quad (3.26)$$

where K_t is the torque coefficient as a function of stator current i_s . Plotted in figure 3.6a is the FE-simulated torque output of the generator against stator current and plotted in figure 3.6b is the torque coefficient K_t against stator current. It is seen in figure 3.6b that K_t begins

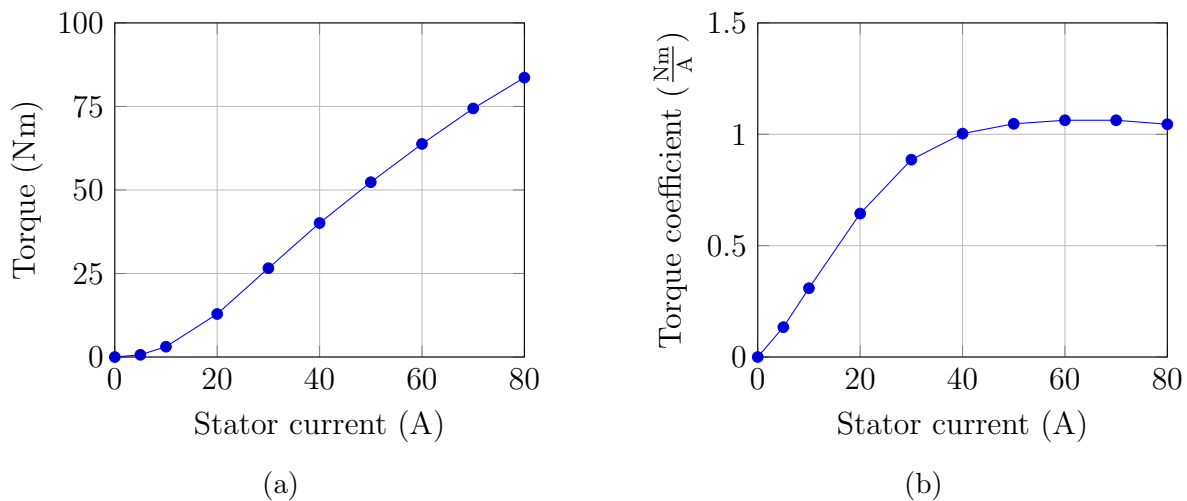


Figure 3.6: Generator torque versus stator current magnitude and torque coefficient K_t versus stator current magnitude at rated current angle of 65° . FEM results.

to flatten out after 40 A. It is decided to design the speed controller around the rated stator current of 55 A. This will ensure optimal performance when soft-stalling is employed (covered later). The value of the torque coefficient is chosen to be $K_t = 1$ and therefore $T_g = i_s$. It

CHAPTER 3. DESIGN OF WIND TURBINE CONTROLLERS

should be noted that this relation between generator torque output and stator current (and thus torque coefficient and stator current) is valid only for 65° current angle.

With the aforementioned simplification and taking the aerodynamic torque input T_a to be 0, equation (3.25) becomes

$$n_g i_s = -J_{\text{eq-t}} \dot{\omega}_t - B_{\text{eq-t}} \omega_t. \quad (3.27)$$

Taking the Laplace transform of (3.27) and rearranging, the open-loop transfer function of the mechanical system for the wind turbine is

$$G(s) = \frac{n_g}{sJ_{\text{eq-t}} + B_{\text{eq-t}}} \quad (3.28)$$

$$= \frac{\frac{n_g}{J_{\text{eq-t}}}}{s + \frac{B_{\text{eq-t}}}{J_{\text{eq-t}}}} \quad (3.29)$$

Inspection of (3.29) reveals that the dynamics of the mechanical system is dependent on the ratio of the gearbox. This should be no surprise as the gearing ratio affects the equivalent inertia of the system that is acted upon by the generator.

3.2.2. Closed-loop system

For the speed controller, it is chosen that a PI controller is to be used so that the turbine system will have improved tracking performance. Thus, the transfer function $D(s)$ of the speed controller will be of the form

$$D(s) = k_{\text{sc-p}} + \frac{k_{\text{sc-i}}}{s} \quad (3.30)$$

$$= \frac{sk_{\text{sc-p}} + k_{\text{sc-i}}}{s} \quad (3.31)$$

where $k_{\text{sc-p}}$ and $k_{\text{sc-i}}$ are the proportional and integral gain constants of the controller, respectively. The loop transfer function $L(s)$ of the system is then given by

$$L(s) = D(s)G(s) \quad (3.32)$$

$$= \left(\frac{sk_{\text{sc-p}} + k_{\text{sc-i}}}{s} \right) \left(\frac{\frac{n_g}{J_{\text{eq-t}}}}{s + \frac{B_{\text{eq-t}}}{J_{\text{eq-t}}}} \right) \quad (3.33)$$

$$= \frac{s \frac{k_{\text{sc-p}} n_g}{J_{\text{eq-t}}} + \frac{k_{\text{sc-i}} n_g}{J_{\text{eq-t}}}}{s \left(s + \frac{B_{\text{eq-t}}}{J_{\text{eq-t}}} \right)} \quad (3.34)$$

$$= \frac{n_L(s)}{d_L(s)}. \quad (3.35)$$

CHAPTER 3. DESIGN OF WIND TURBINE CONTROLLERS

Then, the transfer function of the closed-loop system is given by

$$G_{cl}(s) = \frac{L(s)}{1 + L(s)} \quad (3.36)$$

$$= \frac{\frac{n_L(s)}{d_L(s)}}{1 + \frac{n_L(s)}{d_L(s)}} \quad (3.37)$$

$$= \frac{n_L(s)}{d_L(s) + n_L(s)} \quad (3.38)$$

$$= \frac{s \frac{k_{sc-p} n_g}{J_{eq-t}} + \frac{k_{sc-i} n_g}{J_{eq-t}}}{s^2 + s \left(\frac{B_{eq-t} + k_{sc-p} n_g}{J_{eq-t}} \right) + \frac{k_{sc-i} n_g}{J_{eq-t}}} \quad (3.39)$$

The closed-loop system is thus of second order and the characteristic polynomial (denominator of (3.39)) can be re-parametrised so that it may be defined as

$$d_L(s) + n_L(s) = s^2 + 2\zeta\omega_n s + \omega_n^2 \quad (3.40)$$

where ζ is the damping ratio and ω_n is the natural frequency of the system. Associating terms in (3.40) with those in the denominator of (3.39), the following equations may be derived for the proportional and integral gains k_{sc-p} and k_{sc-i} , respectively,

$$k_{sc-p} = \frac{2\zeta\omega_n J_{eq-t} - B_{eq-t}}{n_g} \quad (3.41)$$

$$k_{sc-i} = \frac{\omega_n^2 J_{eq-t}}{n_g} \quad (3.42)$$

From the presence of the gearing ratio n_g in the open-loop model of the mechanical system, it is to be expected that n_g would be present in the controller gains of (3.41) and (3.42). This is because the effect that n_g has on the system dynamics needs to be counteracted through the controller gains.

The damping ratio ζ is chosen to be 0.707 and the undamped natural frequency ω_n is chosen to be 1 rad/s. The resulting controller gains for the range of gear ratios considered in this study are plotted in figure 3.7. The figure shows a general reduction in the controller gains with increasing gearing ratio. This can possibly be explained by the fact that a larger gearing ratio means that the effects of the generator on the rotor hub in terms of torque production are amplified more and therefore less control effort is required.

CHAPTER 3. DESIGN OF WIND TURBINE CONTROLLERS

n_g	k_{sc-p}	k_{sc-i}
10	9.15	6.48
11	8.32	5.89
12	7.63	5.40
13	7.04	4.98
14	6.54	4.63
15	6.10	4.32

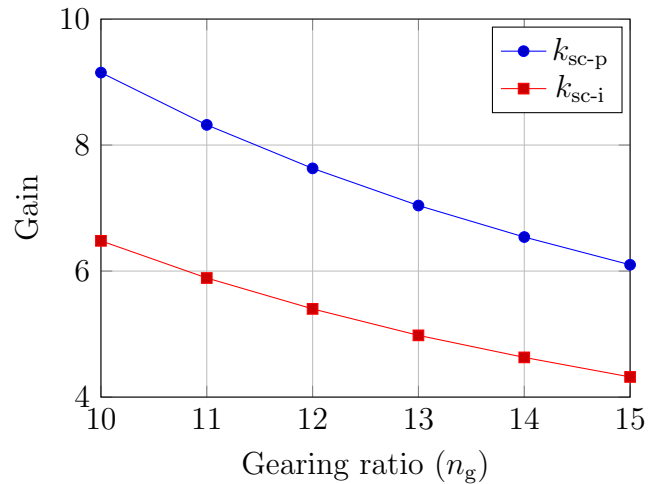


Figure 3.7: Plot of the speed controller proportional and integral gains, k_{sc-p} and k_{sc-i} , respectively, against gearing ratio of the turbine gearbox.

3.3. Turbine system controller

The turbine system controller is responsible for controlling the wind turbine's overall operation. It ensures that the turbine transitions smoothly between the two different control algorithms of regions 2 and 3. The controller has three distinct modes of operation, namely MPPT, speed limiting, and torque limiting.

3.3.1. Region 2 - MPPT control

When operating under region 2, the turbine controller is required to control the speed of the rotor for maximum power capture from the wind. In order to determine the reference speed for the generator, it is necessary to begin with the aerodynamic power equation, i.e. the power captured directly from the wind by the blades, which is described by the equation

$$P_a = \frac{1}{2} \rho \pi R^2 v_w^3 C_p(\lambda) \quad (3.43)$$

where ρ is air density, R is the radius of the rotor swept area, v_w is the wind speed, and $C_p(\lambda)$ is the power coefficient function of the blades. The power coefficient is a function of what is known as the tip-speed ratio (TSR) λ . It is defined as the ratio of the linear speed of the blade tip to the speed of the wind and is given mathematically by the equation

$$\lambda = \frac{\omega_t R}{v_w} \quad (3.44)$$

where ω_t is the angular velocity of the hub.

It is possible to substitute (3.44) into (3.43) for wind speed v_w . The derived equation,

$$P_a = \frac{1}{2} \rho \pi R^5 \omega_t^3 \frac{C_p(\lambda)}{\lambda^3}, \quad (3.45)$$

still depends on the wind speed because of the the λ variable that is present. However, substituting C_p and λ for their optimal values, the equation then represents the optimal power that

CHAPTER 3. DESIGN OF WIND TURBINE CONTROLLERS

may be produced by the blades for a given rotor speed. The resulting equation is presented more concisely as

$$P_a = K_{\text{opt}}\omega_t^3 \quad (3.46)$$

where

$$K_{\text{opt}} = \frac{1}{2}\rho\pi R^5 \frac{C_{p\text{-opt}}}{\lambda_{\text{opt}}^3}, \quad (3.47)$$

and $C_{p\text{-opt}}$ and λ_{opt} are the optimal power coefficient and TSR values for maximum power capture from the wind. Equation (3.46) is rearranged so as to represent the optimal rotor speed required in order to extract the given aerodynamic power such that

$$\omega_t[k+1] = \sqrt[3]{\frac{P_a[k]}{K_{\text{opt}}}}. \quad (3.48)$$

Given that the speed controller is implemented digitally, equation (3.48) is the discrete representation of the speed control law such that $\omega_t[k+1]$ is the speed reference of the rotor hub for the following sampling instant and $P_a[k]$ is the aerodynamic power present at the rotor for the current sampling instant. The hub speed of the turbine follows the reference speed of (3.48) when operating in region 2 and the generator speed reference $\omega_{g\text{-ref}}$ is simply multiplied by the gearing ratio n_g .

3.3.2. Speed limit mode

There are wind speeds where the optimal speed reference from the MPPT is higher than what the generator may safely handle, but maximum power production by the generator has not yet occurred. When the wind reaches a speed that causes the MPPT to command a speed reference higher than the generator's rated speed, the controller simply limits the speed reference to the generator's limit of 157.07 rad/s (1500 RPM). This is done to protect the generator mechanically. When the speed is limited, any further increase in wind speed results in the blades beginning to stall as they are no longer allowed to continue operating at their optimal but reduced power coefficient instead. When the wind speed decreases and the optimal rotor reference speed calculated by the MPPT controller drops below the speed limit of the generator, the turbine will once again be allowed to follow the optimal speed reference.

3.3.3. Torque limit control

When the turbine is operating under the speed limit mode and the wind speed increases to the point where the current within the generator exceeds its rated value, action is taken to protect the generator electrically. Given the small-scale nature of the turbine, the blades do not allow for any physical aerodynamic control features (such as flaps on or pitching of the blades). An alternative technique is required to limit the power captured by the blades.

The technique used in this study to limit power capture is known as *soft-stall* [36] whereby the blades of the turbine are made to operate at a sub-optimal power coefficient. To this end,

CHAPTER 3. DESIGN OF WIND TURBINE CONTROLLERS

the angular speed of the turbine's rotor is controlled relative to the wind speed. This provides the turbine controller with the ability to control the effective power coefficient of the blades and thus the amount of power captured from the wind. With reference to figure 2.13, it can be seen that for a wind speed of 9 m/s the power captured by the turbine can be reduced by simply slowing the speed of the turbine hub. However, soft-stall presents a problem when used for constant power capture.

Maintaining constant power capture by means of soft-stall control is not possible for extended periods of time. The reason behind this is a consequence of the mechanical power equation

$$P = T\omega. \quad (3.49)$$

For the sake of the argument, let it be assumed that the conversion from mechanical to electrical power in the generator is lossless. When the generator is producing rated torque at rated speed, rated power is being produced. Excessive wind speeds cause above-rated power to be produced by the generator and so the speed of the blades need to be reduced in order to diminish the power coefficient of the blades, and thus their ability to capture power. However, it can be seen from (3.49) that in order to maintain rated power output at below-rated generator speed, the torque output of the generator needs to be increased above the rated value as the wind speed increases. Since the torque produced by generators is typically a function of current, above-rated torque equates to above-rated current. Therefore, although constant power limit by means of soft-stall is possible, the thermal handling capabilities of the generator dictates the maximum wind speed up to which the generator may produce constant power as well as the duration for which it can maintain it.

Plotted in figure 3.8 is the difference in torque trajectories followed by the rotor between the constant power and constant torque soft-stall approaches. Also plotted are the torque trajectories produced by the blades for a number of wind speeds. When implementing the constant-power soft-stall approach, the torque produced at the hub by the generator increases with decreasing rotor speed for increasing wind speed. In the figure, the minimum speed to which the rotor may slow under constant-power soft-stall is limited by the peak current handling capability of the generator. This peak torque limit may be 1.5 per unit (PU) of the rated torque for a short period of time. When considering the constant-torque soft-stall approach, the rotor may slow to a slower speed since the current in the generator is limited to its rated value. The turbine is thus able to maintain operating in winds where the constant-power limiting approach may have required the turbine to shut down from thermal overload. The disadvantage of the constant-torque approach is that the power output from the generator decreases with reducing rotor speed.

Constant-torque limiting, instead of constant-power limiting, is implemented as it allows the generator to operate throughout the duration of excessive wind speed as no electrical limits are exceeded for extended periods of time. The downside to this approach, however, is that the electrical power produced by the generator is decreased with decreasing hub speed. The potential advantage is that the constant-torque limit will allow the turbine to continue

CHAPTER 3. DESIGN OF WIND TURBINE CONTROLLERS

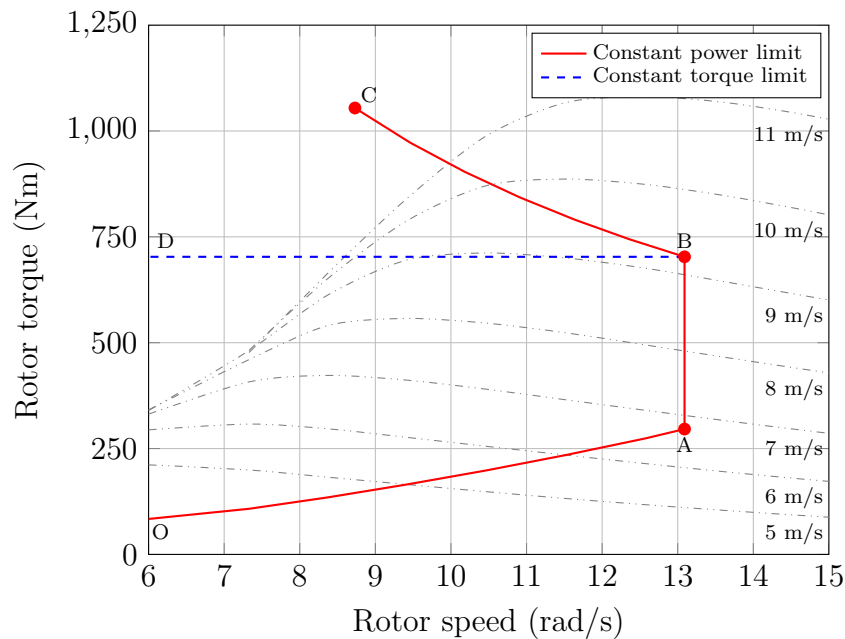


Figure 3.8: Illustrative comparison between torque trajectories for constant power and constant torque limits by means of soft-stalling, plotted against hub speed.

generating power where the constant-power soft-stall approach may have required the turbine to be shut down from thermal overload concerns if operated at above-rated torque (and thus current) for prolonged periods.

3.3.4. Aerodynamic power estimator

The MPPT controller requires the aerodynamic power acting on the blades of the turbine as input for calculating the optimal rotor speed under region 2 operation. Since it is not feasible to directly measure the aerodynamic power, it is instead estimated. Knowledge of the inertia of the system as well as the speed and acceleration of the hub is needed in order to estimate the aerodynamic power being produced by the blades.

The derivation of the equation that will be used to estimate the aerodynamic power P_a begins with the torque equation:

$$T_a - n_g T_g = J_{\text{eq-t}} \dot{\omega}_t \quad (3.50)$$

$$T_a = J_{\text{eq-t}} \dot{\omega}_t + n_g T_g \quad (3.51)$$

where T_a is the aerodynamic torque produced by the blades, T_g is the reaction torque produced by the generator, n_g is the gearing ratio, $J_{\text{eq-t}}$ is the equivalent system inertia referred to the rotor side, and $\dot{\omega}_t$ is the angular acceleration of the hub. Utilising the mechanical power equation of (3.49), (3.51) can be expressed as

$$P_a = \omega_t (J_{\text{eq-t}} \dot{\omega}_t + n_g T_g). \quad (3.52)$$

CHAPTER 3. DESIGN OF WIND TURBINE CONTROLLERS

The turbine hub speed and acceleration is then transferred to the generator side of the gearbox such that

$$P_a = \frac{\omega_g}{n_g} \left(J_{\text{eq-t}} \frac{\dot{\omega}_g}{n_g} + n_g T_g \right). \quad (3.53)$$

Finally, after some rearranging, the equation used to estimate the aerodynamic power is given by

$$P_a = \omega_g \left(\dot{\omega}_g \frac{J_{\text{eq-t}}}{n_g^2} + T_g \right). \quad (3.54)$$

Equation (3.54) requires the reaction torque produced by the generator. This value, however, is not measured and is itself an estimate as well. A mapping between the torque output and current magnitude input at the rated current angle is stored in an LUT for the torque estimate. Torque measurements at rated current angle are performed utilising finite element analysis (FEA) and validated against physical measurements. Physical torque measurements are performed at 1500 RPM, 1000 RPM, and 500 RPM, and plotted in figure 3.9 along with the FEA results. From the figure, no discernible difference can be seen between the physical

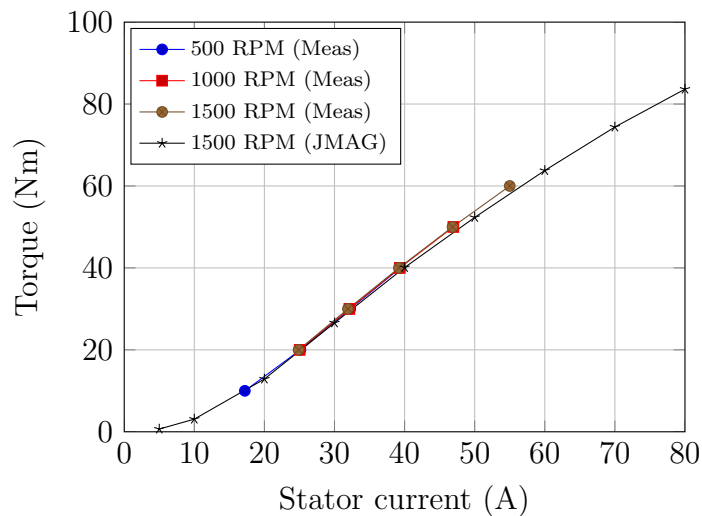


Figure 3.9: Measured generator reaction torque, as well as simulated generator reaction torque, versus input current.

torque measurements at the different generator speeds. However, the FEA torque result starts to diverge slightly from the measured torque readings from about 40 A and greater. The turbine controller thus requires two inputs to operate – the generator stator current and speed.

CHAPTER 3. DESIGN OF WIND TURBINE CONTROLLERS

3.3.5. Complete wind turbine controller

An overview of the turbine system controller algorithm is presented as a flowchart in figure 3.10. The turbine controller is responsible for controlling the rotor speed when maximum power is to be extracted from the wind under region 2 and when power capture must be reduced under region 3. The inputs to the turbine controller are generator speed and stator current.

The routine begins at the *Sampling instant* entry point and is called every sampling instant which is 10 kHz, or every 100 μ s. The first task is to predict the current aerodynamic power value and update the simple moving average (SMA) of the estimated aerodynamic power. The SMA filter is generally considered to be better suited at reducing random noise while maintaining a sharper step response than a simple single-pole low-pass filter (LPF). The SMA filter is implemented as a circular buffer that is updated with the new estimated aerodynamic power value at a rate of 100 Hz, that is, every 100th sampling instant. The length of the SMA window affects its ability to reject random changes but also its dynamic response to larger variations.

The turbine controller then determines whether the stator current limit is being exceeded. If it is, the controller will only set the current-limit-active flag if the speed of the turbine is already being limited. Should current limiting not be active, the turbine controller commands the generator reference speed ω_{g-ref} to follow the optimal speed for maximum power capture. Should the optimal generator speed reference exceed the limit, the speed reference will be capped at the limit and the speed-limit-active flag set, otherwise the flag is cleared and no limiting takes place.

If current limiting is active, the turbine controller calculates the compensated generator stator current i_s^* and computes the change in generator speed reference that should occur. If i_s^* is above the limit, the calculated change in generator speed is rate-limited and subtracted from the current speed reference value. On the other hand, should i_s^* be below the limit, the change in generator speed is again rate-limited but added to the current generator speed reference. A check is done to determine if the speed reference has returned to the maximum value and if it has, the current-limit-active flag is cleared.

CHAPTER 3. DESIGN OF WIND TURBINE CONTROLLERS

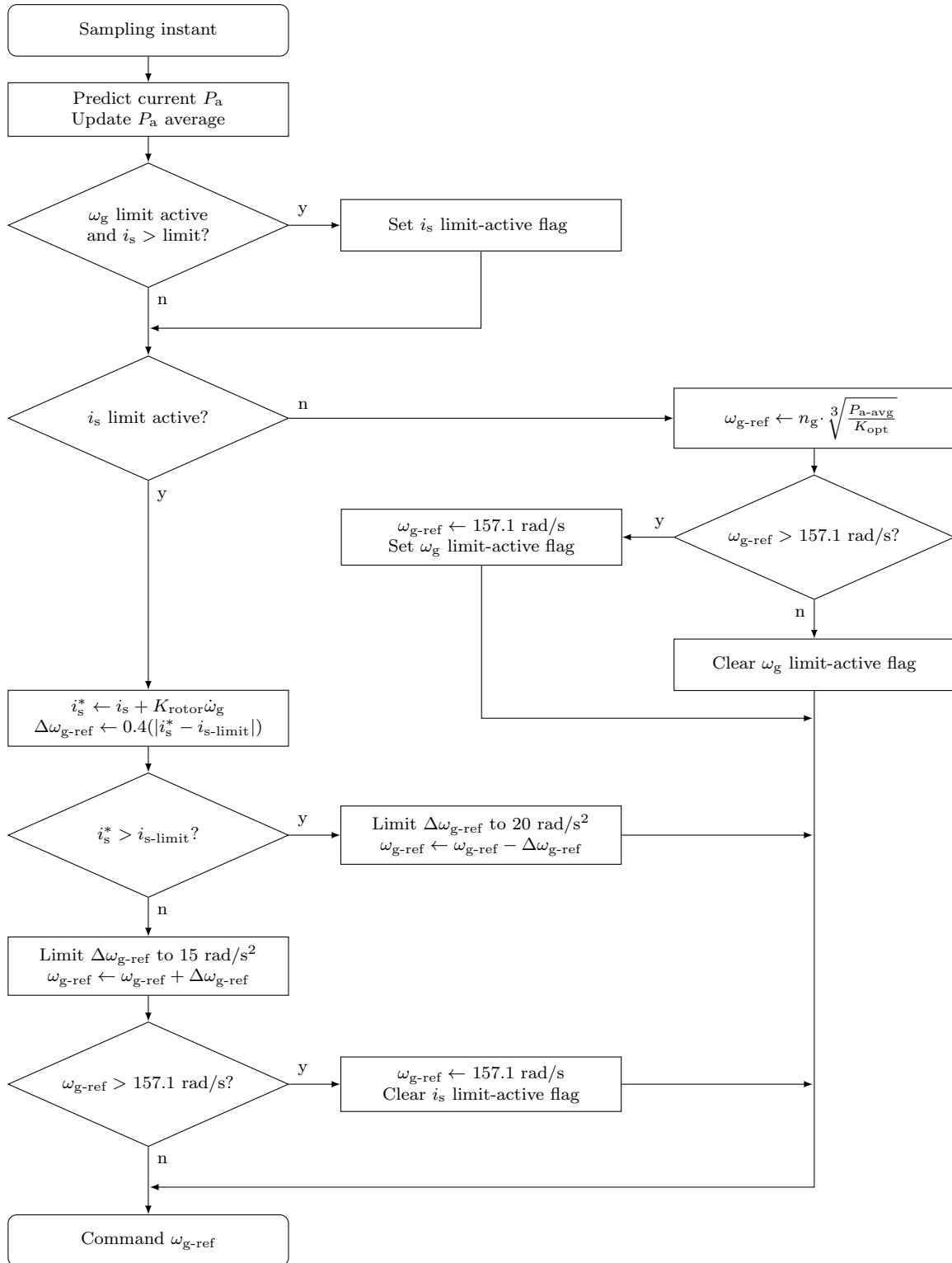


Figure 3.10: Flowchart depicting turbine system controller algorithm operation.

CHAPTER 3. DESIGN OF WIND TURBINE CONTROLLERS

3.3.6. Compensated stator current

The explanation of the turbine controller in the previous section mentions the calculation of a compensated RSM stator current. This is needed as instability in the speed control of the generator may occur when constant-torque limiting is active and a change in the generator speed is commanded. If a decrease in generator speed is commanded, kinetic energy needs to be extracted from the system. This is accomplished by raising the generator's current reference to exert more torque upon the system. However, the turbine controller is monitoring the stator current in order to determine if the generator speed should be increased or decreased. This commanded increase in current will result in the turbine controller attempting to reduce the generator speed even further in an attempt to reduce the stator current. This positive feedback effect continues while the stator current is above the generator current limit threshold. When the measured stator current value drops below the limit, the turbine controller reduces the current reference in order to increase the generator speed. The process repeats and the result is an unstable system.

In order to remedy the problem, a form of derivative control is implemented in the constant-torque limiting routine of the turbine controller. An altered stator current value i_s^* is computed and used by the turbine controller to determine if the rotor speed should be increased or decreased when operating under torque-limit mode. The net torque perceived by the generator is a function of its own acceleration and inertia of the system related to the generator side. It is given by the equation

$$T_{g\text{-net}} = \frac{J_t}{n_g^2} \dot{\omega}_g. \quad (3.55)$$

Similar to the design procedure of the speed controller in section 3.2, the net torque of (3.55) can be represented by an equivalent generator stator current. Since constant-current control occurs at the rated generator current of 55 A, the torque coefficient K_t is again equal to 1 and so $i_{s\text{-offset}} = T_{g\text{-net}}$. Equation 3.55 then becomes

$$i_{s\text{-offset}} = \frac{J_t}{n_g^2} \dot{\omega}_g, \quad (3.56)$$

$$= K_{\text{rotor}} \dot{\omega}_g. \quad (3.57)$$

The value $i_{s\text{-offset}}$ can be thought of as a relation between the acceleration/deceleration of the generator and the current value that is superimposed upon a steady-state current value if the generator were not accelerating/decelerating. This compensation current is added to the measured current value in order to cancel out the change in stator current as a result of the acceleration/deceleration commanded from the generator. The turbine controller's logic thus operates on an equivalent current value as if the generator was not accelerating/decelerating.

Chapter 4

Wind turbine modelling and simulation

The entire wind turbine is modelled and simulated in MathWorks's Simulink. The model is divided into modules, each pertaining to a specific aspect of simulation, that is, the wind generator, aerodynamics interaction, drivetrain dynamics, the reluctance synchronous generator model, and the current, speed, and turbine system controllers. Figure 4.1 illustrates the interaction between the Simulink blocks that make up the wind turbine simulator as a whole.

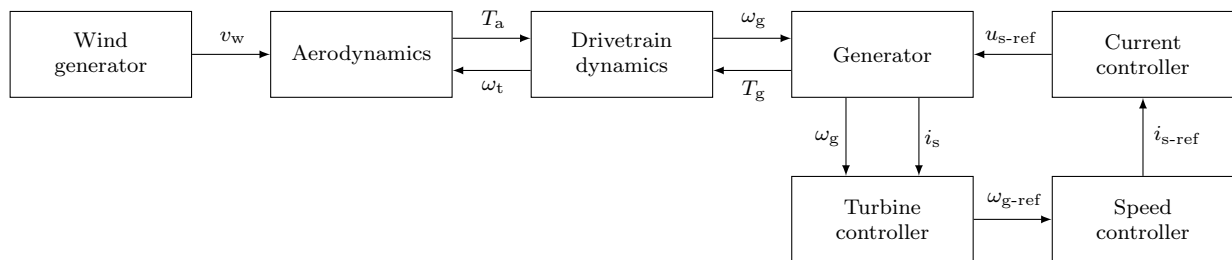


Figure 4.1: Block diagram illustrating relation between the different Simulink blocks of the wind turbine model.

The wind generator simulates a wind velocity time-series that is sent to the aerodynamics block. The aerodynamics block calculates the resulting aerodynamic torque which is sent to the drivetrain block. In return, the drivetrain block updates the aerodynamic block with the hub speed and the generator block with the speed of the generator. The generator block provides the drivetrain block with its reaction torque. The turbine controller takes the speed and stator current of the RSM and based on its implemented algorithm, determines the reference speed of the generator. This reference speed is fed into the speed controller which produces a current reference. Finally, the current controller produces a voltage reference from the current reference input which is finally applied to the stator of the generator.

4.1. Wind generator

The wind generator block outputs a simulated wind velocity time-series. This time-series data is the result of the equation

$$v_w = V_0 + v_t \quad (4.1)$$

where V_0 is the mean wind speed and v_t is the “fluctuating” component, known as turbulence. The turbulence component may be generated by applying a filter, that has a specific power spectral density (PSD), to a white noise signal.

A number of spectra exist for the simulation of wind turbulence such as the van der Hoven, von Karman, and Kaimal models. The Kaimal model is a popular choice and is chosen here for its simplicity. In order to simplify the modelling of the wind speed, only the longitudinal direction of the wind speed is considered; wind components in the lateral and upward directions are not modelled. The PSD of the Kaimal model used in this study is given by the equation [64]

$$S(f) = \sigma^2 \frac{\frac{4L_k}{V_0}}{\left(1 + \frac{6fL_k}{V_0}\right)^{5/3}} \quad (4.2)$$

where f is the frequency, σ is the velocity standard deviation, and L_k is the velocity integral scale parameter. An example Kaimal PSD is plotted in figure 4.2 and sample wind speed time-series are plotted in figure 4.3 for average wind speeds of 5 m/s and 12 m/s.

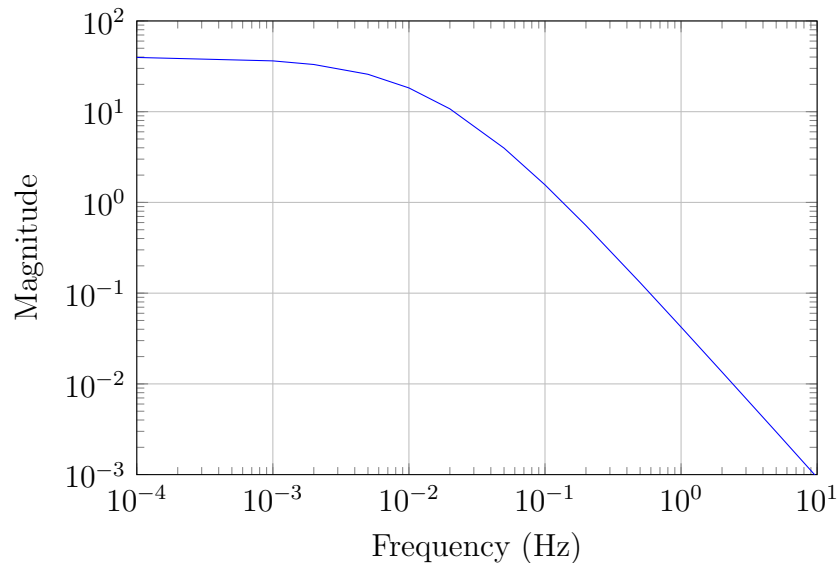


Figure 4.2: Kaimal power spectral density.

Depicted in figure 4.4 is the implementation of the wind speed generator in Simulink. The block receives no inputs and has a single output. It simply adds the turbulence component v_t to the mean wind speed V_0 according to (4.1). The turbulence component is first passed through a low-pass filter in order to smooth it. The turbulence component data is generated by a MATLAB script that allows the velocity standard deviation σ , velocity integral scale parameter L_k , and average wind velocity V_0 of the wind generator to be modified.

CHAPTER 4. WIND TURBINE MODELLING AND SIMULATION

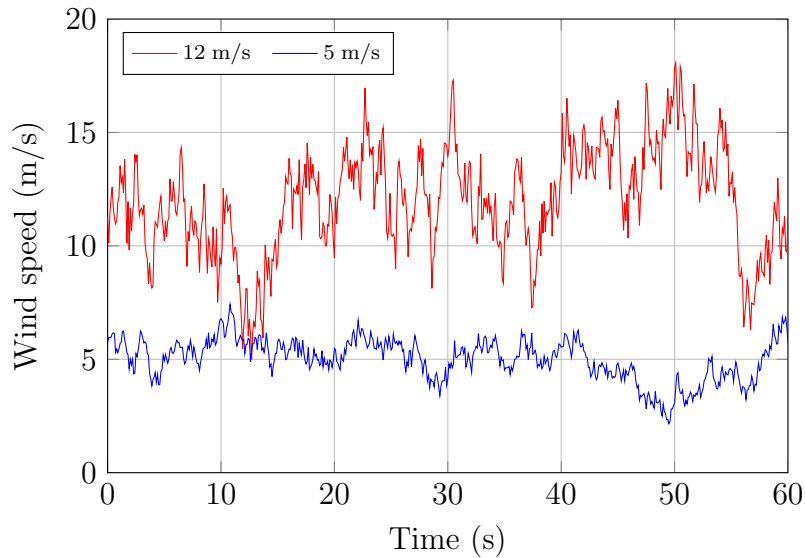


Figure 4.3: Wind speed time series generated from the Kaimal PSD for mean wind speeds of 12 m/s and 5 m/s.

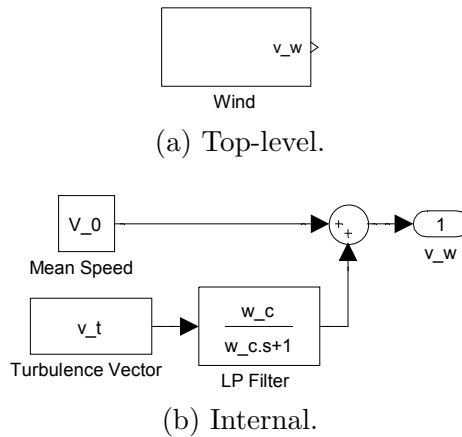


Figure 4.4: Wind generator block of the wind turbine Simulink model.

4.2. Aerodynamics

The aerodynamics block models the interaction between the turbine blades and the wind. The aerodynamic torque produced at the hub is described by the conversion of the aerodynamic power equation of (3.43),

$$P_a = \frac{1}{2} \rho \pi R^2 v_w^3 C_p(\lambda), \quad (4.3)$$

to the aerodynamic torque equation by means of the mechanical power equation of (3.44),

$$P = T\omega. \quad (4.4)$$

The torque produced by the blades at the hub as a result of the incident wind is thus described by the equation

$$T_a = \frac{\frac{1}{2} \rho \pi R^2 v_w^3 C_p(\lambda)}{\omega_t}. \quad (4.5)$$

CHAPTER 4. WIND TURBINE MODELLING AND SIMULATION

This equation can be expressed using the torque coefficient function $C_t(\lambda)$, defined by $C_t = \frac{C_p}{\lambda}$, nevertheless, (4.5) is used as is in the aerodynamics block.

In order to simplify the interaction between the wind and the blades, it is assumed that the wind interacts evenly across and perpendicularly to the plane in which the blades rotate (no wind shear effects). Furthermore, cyclic effects such as torque reduction owing to tower shadow are not considered.

Apart from directly affecting the power produced by the blades, the wind speed relative to the speed of the hub also affects the efficiency of the blades. As covered in a previous chapter, the tip-speed ratio is the ratio of the linear speed of the blade tip to the passing wind speed, given mathematically by the equation

$$\lambda = \frac{\omega_t R}{v_w}. \quad (4.6)$$

For each value of the tip-speed ratio λ of a turbine, there is a unique efficiency value at which the turbine blades operate. The C_p - λ relationship of the turbine blades used in this study is plotted in figure 4.5.

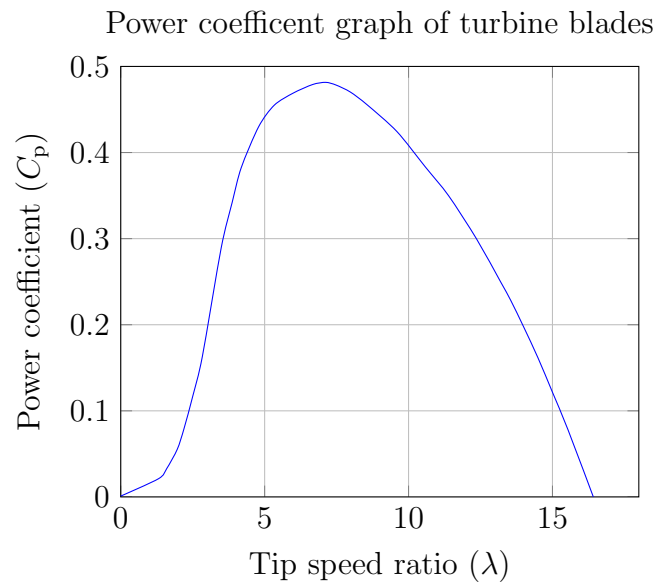


Figure 4.5: C_p - λ curve of turbine blades used in the study.

The aerodynamics block receives the simulated wind velocity and turbine hub speed as inputs and outputs the corresponding torque that is produced at the hub of the turbine. The top-level block is shown in figure 4.6a and the underlying Simulink implementation is shown in figure 4.6b. Using the two inputs to the block, λ is calculated according to (4.6) and applied to the lookup table containing the C_p - λ curve. The returned C_p value is multiplied by other variables and divided by ω_t as defined by (4.3) before the aerodynamic torque value is finally outputted.

CHAPTER 4. WIND TURBINE MODELLING AND SIMULATION

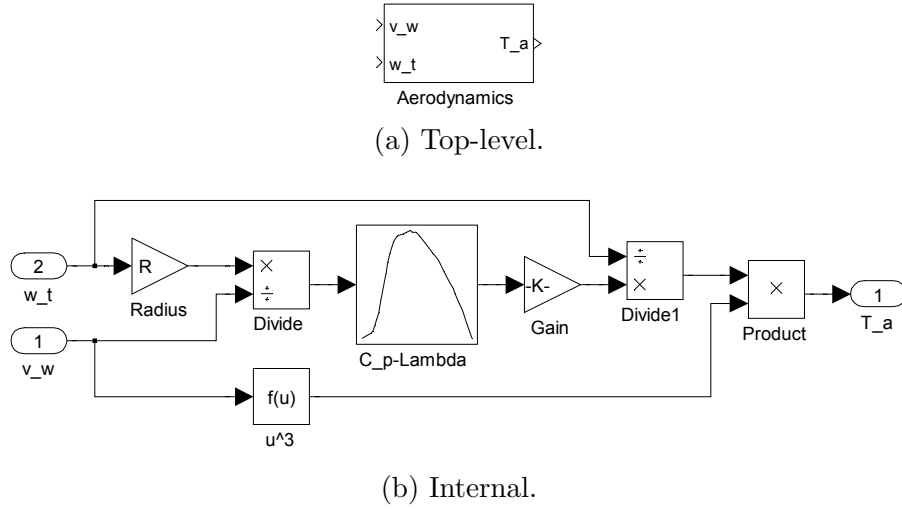


Figure 4.6: Aerodynamics block of Simulink turbine simulator model.

4.3. Drivetrain

The drivetrain block models the mechanical dynamics of the turbine hub, gearbox, and generator. Only the friction and inertia of the system are considered while the shafts are assumed to be rigid with no spring component.

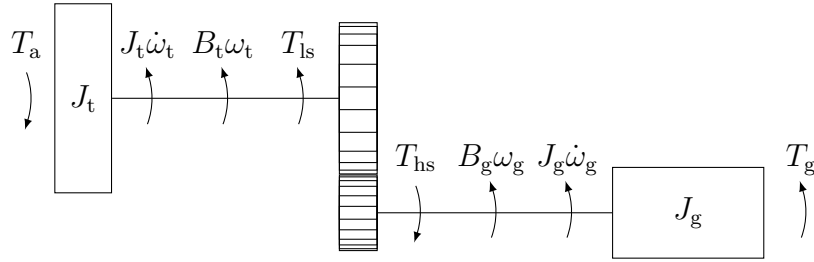


Figure 4.7: Diagram representation of turbine drivetrain.

To arrive at the differential equation that describes the dynamics of the mechanical system, the schematic representation of the mechanical system in figure 4.7 is expressed by the equations

$$T_a - T_{ls} = B_t \omega_t + J_t \dot{\omega}_t, \quad (4.7)$$

$$T_{hs} - T_g = B_g \omega_g + J_g \dot{\omega}_g, \quad (4.8)$$

where T is torque, B is the friction coefficient, and J is inertia. The subscripts a, ls, hs, g, and t denote aerodynamic, low-speed, high-speed, generator, and turbine, respectively. Equations (4.7) and (4.8) are rearranged such that

$$T_{ls} = T_a - B_t \omega_t - J_t \dot{\omega}_t, \quad (4.9)$$

$$T_{hs} = T_g + B_g \omega_g + J_g \dot{\omega}_g. \quad (4.10)$$

The torque acting on the high- and low-speed gears are related by the gearing ratio n_g of the gearbox. This ratio is defined as

$$n_g = \frac{T_{ls}}{T_{hs}} = \frac{\omega_g}{\omega_t}. \quad (4.11)$$

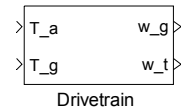
CHAPTER 4. WIND TURBINE MODELLING AND SIMULATION

By using the definition of the gearing ratio in (4.11), (4.10) is related to the low-speed side of the gearbox by $T_{hs} = \frac{T_{ls}}{n_g}$ before being used to substitute for T_{ls} in (4.9). Also, $\frac{\omega_g}{n_g}$ is substituted for ω_t in (4.9) before writing the resulting equation in terms of the generator speed derivative $\dot{\omega}_g$. The final equation that describes the mechanical model of the turbine is given by

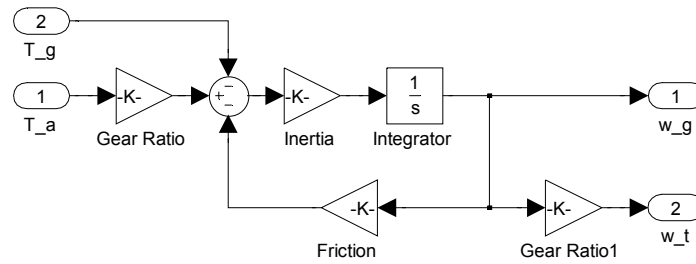
$$\dot{\omega}_g = \frac{\left[\frac{1}{n_g} T_a - T_g \right] - \left[B_g + \frac{1}{n_g^2} B_t \right] \omega_g}{\left[J_g + \frac{1}{n_g^2} J_t \right]}. \quad (4.12)$$

In (4.12), the inertia J_t and friction coefficient B_t of the turbine's low-speed shaft are related to the generator's high-speed shaft by the square of the gearing ratio, n_g^2 .

The Simulink block of the drivetrain model receives the aerodynamic torque from the aerodynamics block and the reaction torque from the generator as inputs and outputs the resulting generator and turbine hub speeds. The top-level view of the drivetrain block is shown in figure 4.8a and the underlying Simulink implementation is shown in figure 4.8b.



(a) Top-level.



(b) Internal.

Figure 4.8: Drivetrain block of Simulink turbine simulator model.

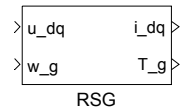
CHAPTER 4. WIND TURBINE MODELLING AND SIMULATION

4.4. Generator

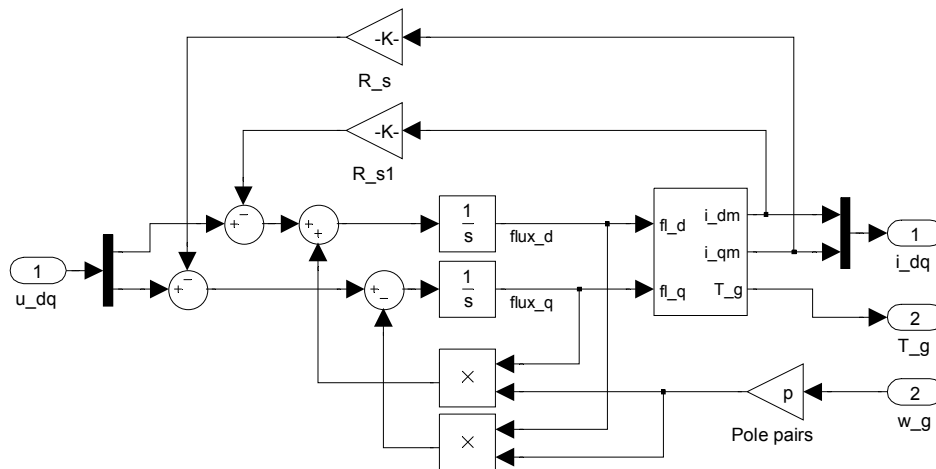
The Simulink model of the RSM is taken from a previous study [56] and modified slightly. Only the electrical behaviour of the generator is modelled in the generator block as the mechanical behaviour is lumped together with the rest of the mechanical system in the drivetrain block. Iron losses are not modelled as they are difficult to model accurately and not strictly necessary for the purpose of the study.

The Model of the RSM used in Simulink avoids the need for the calculation of inductances. The effects owing to saturation and cross-coupling, for all operating points, are handled through the use of 2D lookup tables (LUTs). The flux linkages are simulated from a finite element model of the RSM before being transformed for use in the Simulink model's LUTs.

Figure 4.9 presents the top-level and internal views of the generator's electrical model in Simulink. The model receives the stator voltage from the current controller as well as the generator speed from the drivetrain model. The model outputs the dq-axis stator currents.



(a) Top-level.



(b) Internal.

Figure 4.9: Generator block of Simulink turbine simulator model.

4.5. Current controller

The current controller’s purpose is to take the reference current value and output the set of dq-axis voltages that will effect the reference current value at the rated current angle within the RSM. The block- and low-level representations of the current controller as implemented in the Simulink wind turbine model are shown in figure 4.10.

Inspection of figure 4.10b reveals that the decoupling of the mutual inductance voltages between the axes have not been included in the current controller. The reason is that the effects from the mutual coupling is incredibly small and so does not play a significant role in the cross-coupling present between the two axes.

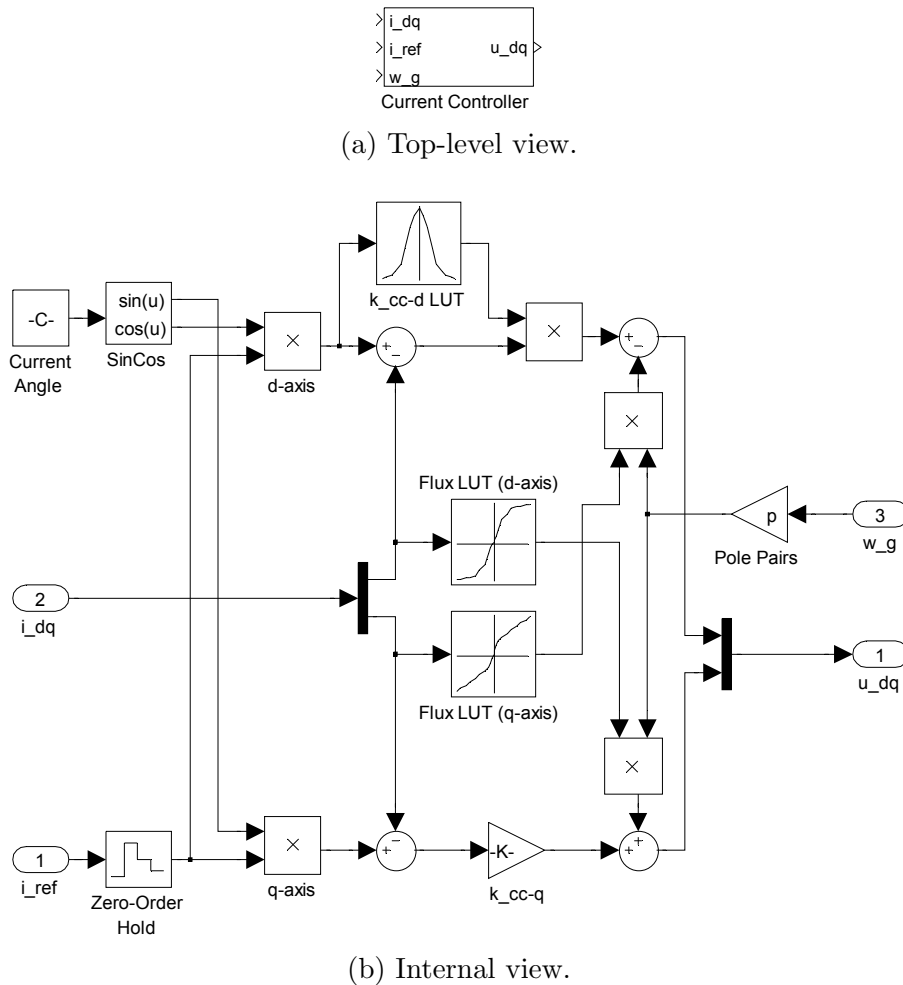
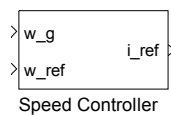


Figure 4.10: Current controller block of Simulink turbine simulator model.

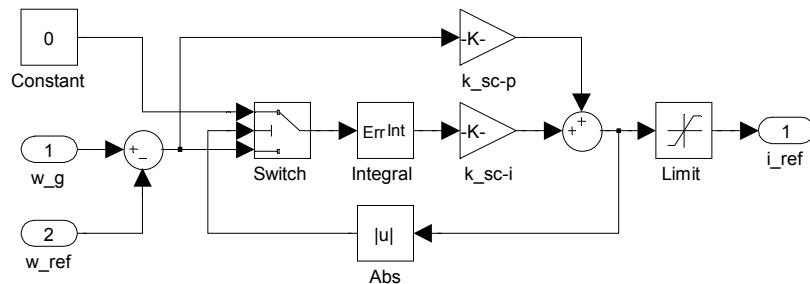
CHAPTER 4. WIND TURBINE MODELLING AND SIMULATION

4.6. Speed controller

The generator speed reference output from the turbine system controller is input to the speed controller where a current reference is generated at its output. The switch in the speed controller is part of the integral anti-windup implementation. When the output of the speed controller exceeds the maximum current limit for the generator, the switch switches to the zero input so that integration is halted. When the output stops saturating, the switch changes back to allow the integral part of the controller to continue. Figure 4.11 presents the top-level and internal views of the speed controller block in the Simulink wind turbine model.



(a) Top-level.



(b) Internal.

Figure 4.11: Speed controller block of Simulink turbine simulator model.

4.7. Turbine system controller

The turbine controller is implemented as an S-function in MATLAB for ease of implementing the algorithm. The inputs received by the turbine controller are the generator current and speed and the generator speed reference is output. The aerodynamic estimated power is calculated from the torque estimated from the stator current

Chapter 5

Overall wind turbine results

5.1. Simulation results

This section presents simulated results from the Simulink wind turbine model. Comparisons between the simulated and measured results is saved for the following section. This section, however, looks at the effects that the system parameters have on the operation of the wind turbine as a whole.

5.1.1. Power coefficient curve gradient

When the turbine is operating near its optimal point, that is to say when λ is close to λ_{opt} , larger variations in the turbine parameters can be observed. However, when operating under strong stall conditions such that $\lambda < \lambda_{\text{opt}}$, these variations are greatly attenuated. Differences in variation of the generator speed, torque, and electrical power output are plotted in figure 5.2. For the near- λ_{opt} scenario, defined as $\Delta\lambda_1$, the average wind speed is 8.25 m/s while for

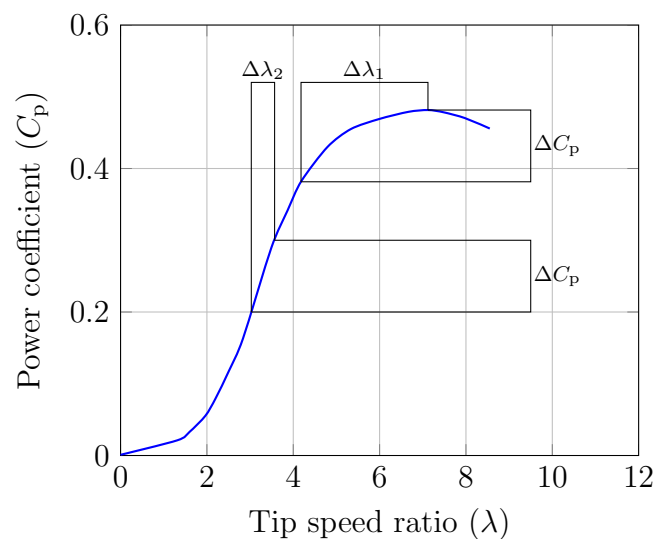


Figure 5.1: Change in tip-speed ratio λ required for a specific reduction in power coefficient C_p at two different operating points.

CHAPTER 5. OVERALL WIND TURBINE RESULTS

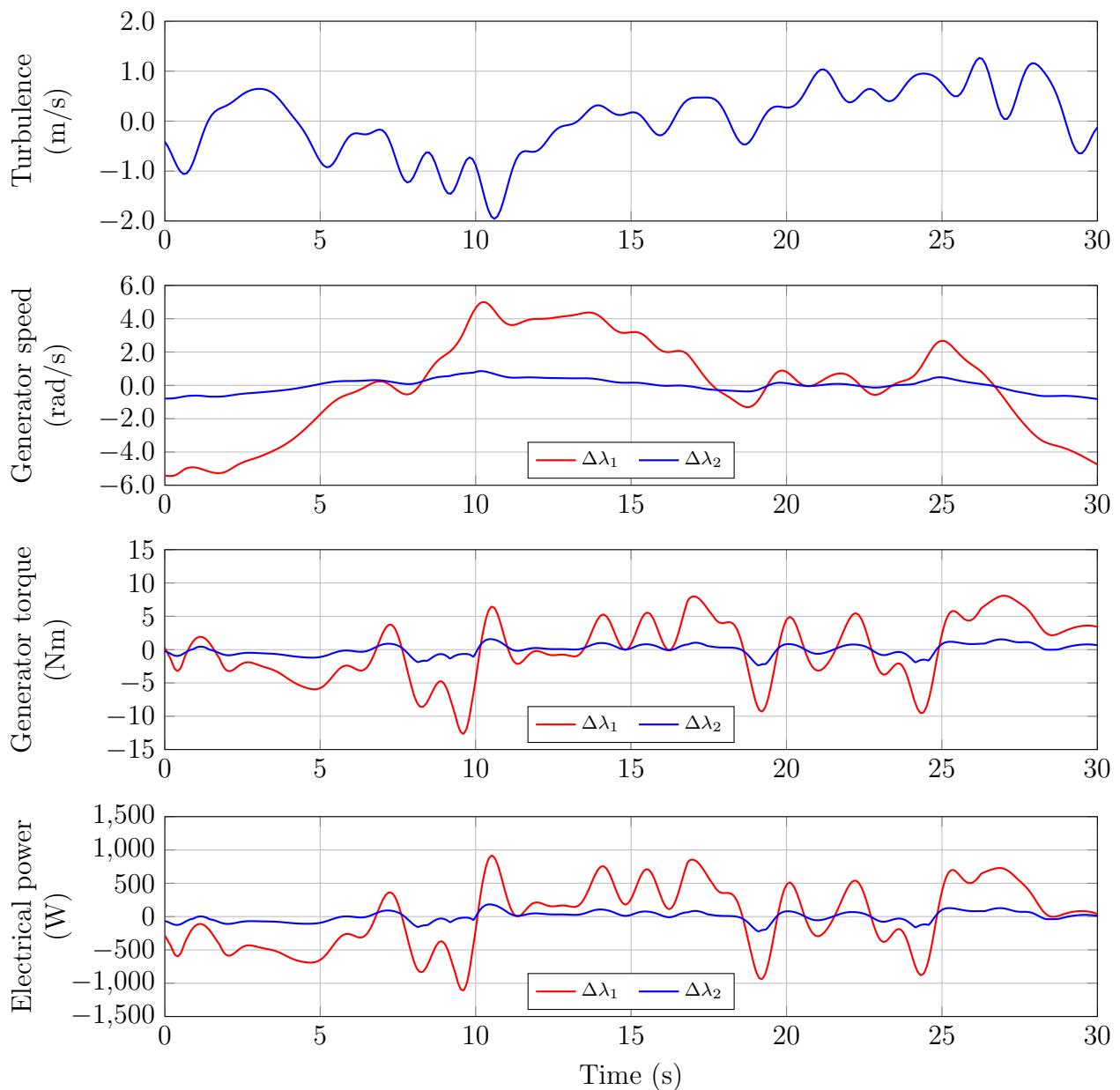


Figure 5.2: Comparison between parameter values for near- λ_{opt} and $\lambda < \lambda_{\text{opt}}$ operating points for generator speed, torque, and electrical output power.

the $\lambda < \lambda_{\text{opt}}$ scenario, defined as $\Delta\lambda_2$, it is 11 m/s. The turbulence graph in figure 5.2 is the turbulence component that is used for both average wind speeds and the gearing ratio tested is $n_g = 12$.

Each graph in figure 5.2 is a plot of the deviation of that parameter across the sampled period. This eliminates the steady-state component of the values and allows a more direct comparison of the changes in magnitude. It is seen in the figure that each parameter examined exhibits a larger variation when the turbine is operating closer to its optimal TSR than when operating at a more reduced TSR.

Illustrated in figure 5.1 is the reason for the effects seen in figure 5.2. When a particular reduction in power coefficient ΔC_p is required, a change in rotor speed, and thus λ , is required. This means that a large change $\Delta\lambda_1$ is required when operating near λ_{opt} to effect the reduction

CHAPTER 5. OVERALL WIND TURBINE RESULTS

in C_p . However, when operating at an already reduced λ value, a smaller change $\Delta\lambda_2$ is required to effect the same reduction in power coefficient.

5.1.2. Gearbox ratio

The ratio of the gearbox has an impact on the energy capture capability of the turbine. Figure 5.3 is a 10-second average scatter plot of the electrical power produced by the generator versus the turbine hub speed with gearing ratio as a parameter.

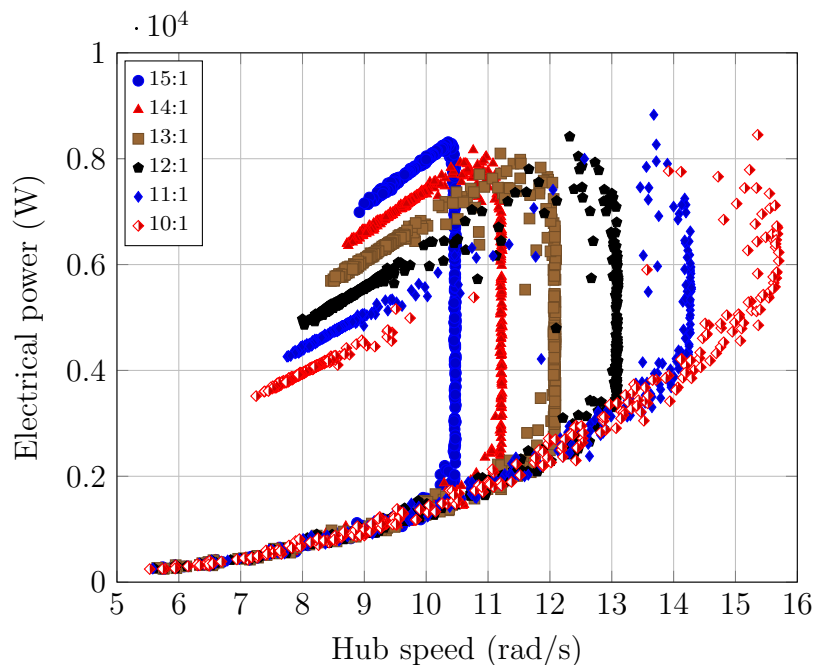


Figure 5.3: Scatter-plot of generator electrical power output versus turbine hub speed with gearing ratio as a parameter.

Perhaps most prominently visible in figure 5.3 is the difference in definition between the different operating regions for each gearing ratio. The 15:1 gearing ratio power trajectory shows the sharpest definition while the 10:1 gearing ratio power trajectory shows the least. The 15:1 gearing ratio exhibits the sharpest definition between regions as the torque produced by the generator is amplified by the gearbox the most and is thus better able to control the rotor speed. The blades are also operating under stronger stall conditions by the time the current limit of the generator is being exceeded and so less control effort is required to reduce the power captured as described in section 5.1.1. On the other hand, the generator torque is less amplified by the gearbox for the 10:1 gearing ratio as well as operating closer to λ_{opt} when the generator current limit begins to be exceeded. The turbine thus needs to reduce the rotor speed more drastically in order to reduce the power coefficient. These factors result in the generator barely operating consistently near its rated power, resulting in few data points around that region.

The aforementioned phenomenon has an impact on the energy capture capacity of the turbine. The energy captured for different average wind speeds and gearing ratio combinations

CHAPTER 5. OVERALL WIND TURBINE RESULTS

over a three-minute period is plotted in figure 5.4. Despite the 10:1 gearing ratio resulting in the turbine operating in the MPPT mode for a wider range of wind speeds, the 15:1 gearing ratio still exhibits a higher energy yield. The explanation for this can be seen in figure 5.3 where there are very few data points around the rated power region of the generator for the 10:1 gearing ratio whereas there are plenty more for the 15:1 gearing ratio. The rate of increase of energy capture with increasing average wind speed for each successive gearing ratio is shallower. This is because with each increase in gearing ratio, the blades experience a higher degree of stall the closer to maximum power the generator gets. Also visible in figure 5.4 is the difference in drop-off rates of energy capture at excessive wind speeds. The 10:1 gearing ratio exhibits the steepest reduction while the 15:1 gearing ratio exhibits the most gradual. An explanation can be given with yet another reference to figure 5.3. Simply put, the smaller gearing ratio requires more drastic stalling in order to reduce energy capture since it is operating closer to C_{p-max} when soft-stalling is employed than the larger gearing ratios.

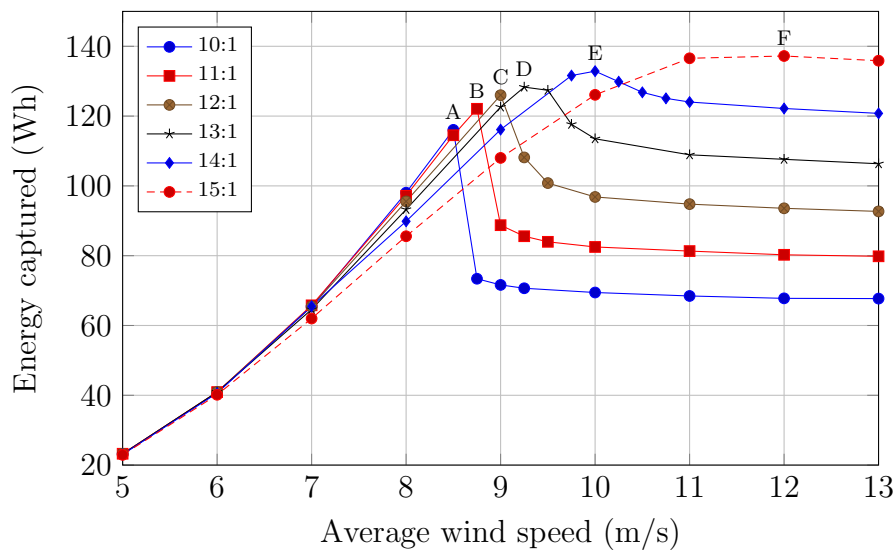


Figure 5.4: Energy capture versus average wind speed with gear ratio as a parameter over a three-minute interval.

CHAPTER 5. OVERALL WIND TURBINE RESULTS

5.1.3. Simple moving average window size

The turbine controller utilises a simple moving average (SMA) filter to smooth the estimated aerodynamic power so that the obtained generator speed reference in (3.48) will be less erratic. The window length of the SMA affects the speed response of the turbine to changes in wind speed. A narrower window causes the turbine to react faster to changes in wind speed while a wider window causes the turbine to react slower.

Figure 5.5 plots the effects on generator speed and torque, and turbine power coefficient for three different lengths of the SMA window. It is seen in the figure that when no averaging is performed, the generator speed varies in accordance with the wind speed. The resulting torque to command such changes in speed is plotted in the graph below. A tremendous amount of variation occurs in the torque output of the generator. The overall result of no filtering is that the turbine rotor follows the changing wind speed much more closely and thus operates much closer to maximum power coefficient. When averaging of the estimated rotor power is performed however, the change in turbine speed is more gradual and does not exhibit the same fast and sudden changes as is the case without filter of P_a . Since the turbine rotor speed is not being commanded to follow every change in wind speed, the torque output of the generator is reduced.

The main benefit of smoothing the speed reference of the generator is that the drivetrain experiences less fatigue. The downside, as seen in the figure, is that the turbine does not operate as close to maximum power coefficient $C_{p-\max}$ as often as is the case without filtering.

CHAPTER 5. OVERALL WIND TURBINE RESULTS

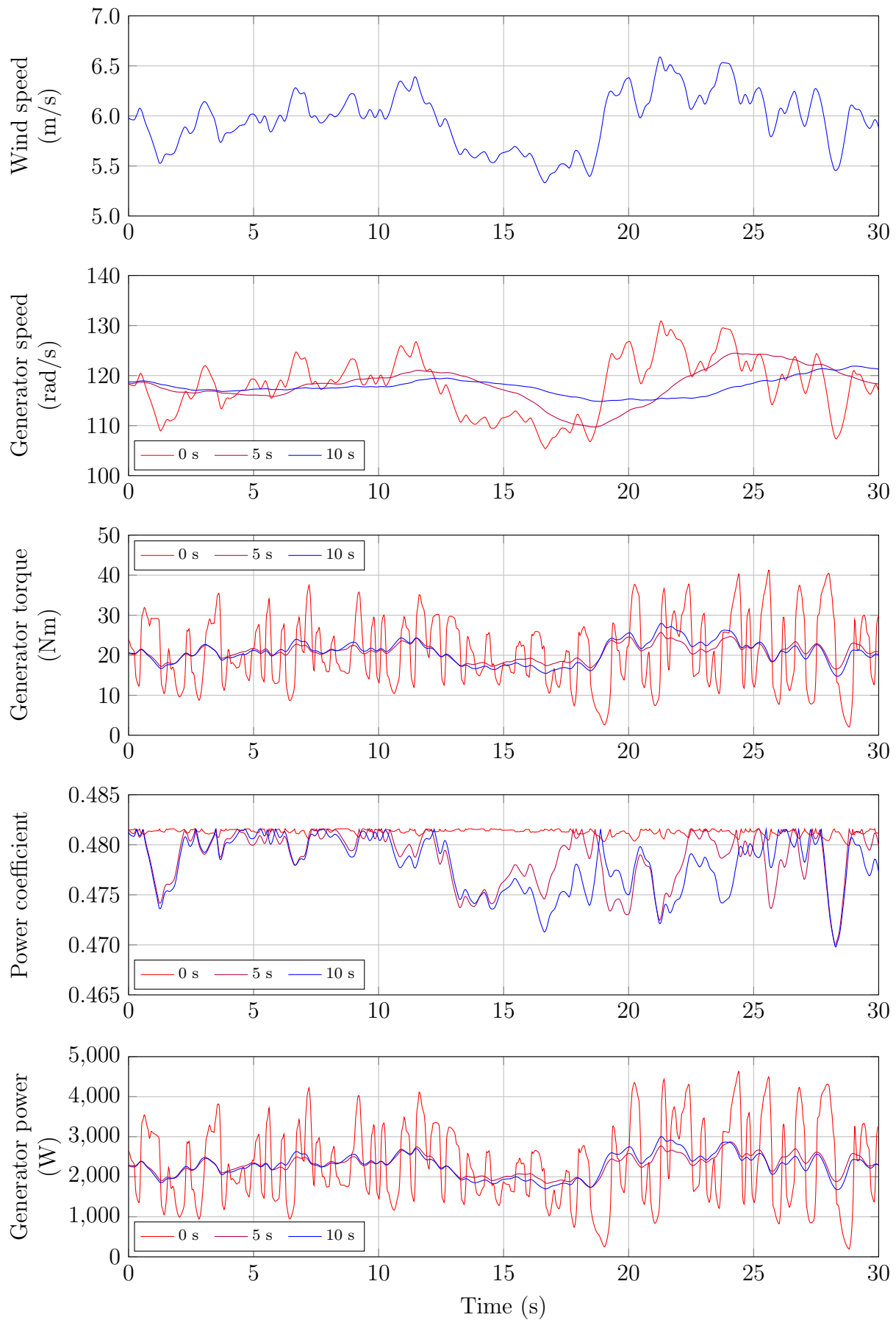


Figure 5.5: Plots of the effect that the length of the SMA window length has on the generator speed, generator torque output, and power coefficient of the blades.

CHAPTER 5. OVERALL WIND TURBINE RESULTS

5.2. Measurement results

This section discusses the practical measurements taken from the testbench set-up and their comparison with the simulated results.

5.2.1. Testbench

A laboratory testbench comprising a 37 kW induction machine coupled to the 9.2 kW RSM under test via a torque sensor is set up to confirm the simulated results. A photograph of the set-up is presented in figure 5.6. The torque sensor is used only to validate the estimated torque returned by the turbine controller. Each machine is supplied power by its own voltage-source converter (VSC). The VSCs are connected back-to-back so that their DC buses are shared while both VSCs are controlled independently by their own rapid-prototyping system (RPS). The rapid-prototyping systems execute the user-programmed control algorithms and generate the necessary space vector pulse width modulation (SV-PWM) switching states that are then used to control the VSCs directly. The rapid-prototyping systems are x86 PC-compatible single-board computers connected to a backplane that provides inputs/outputs such as the encoder reader, ADCs and DACs, PWM output, and a few switches with a hexadecimal display. Figure 5.7 is a photo of the two VSCs, the PC/104-based RPS, and an oscilloscope that is used to view waveforms and data output in real-time.

The rapid-prototyping systems run a desktop Linux distribution but have the Real-Time Applications Interface (RTAI) kernel module installed. This kernel module gives the Linux kernel the ability to execute code at strict timing intervals. Code that controls the electrical

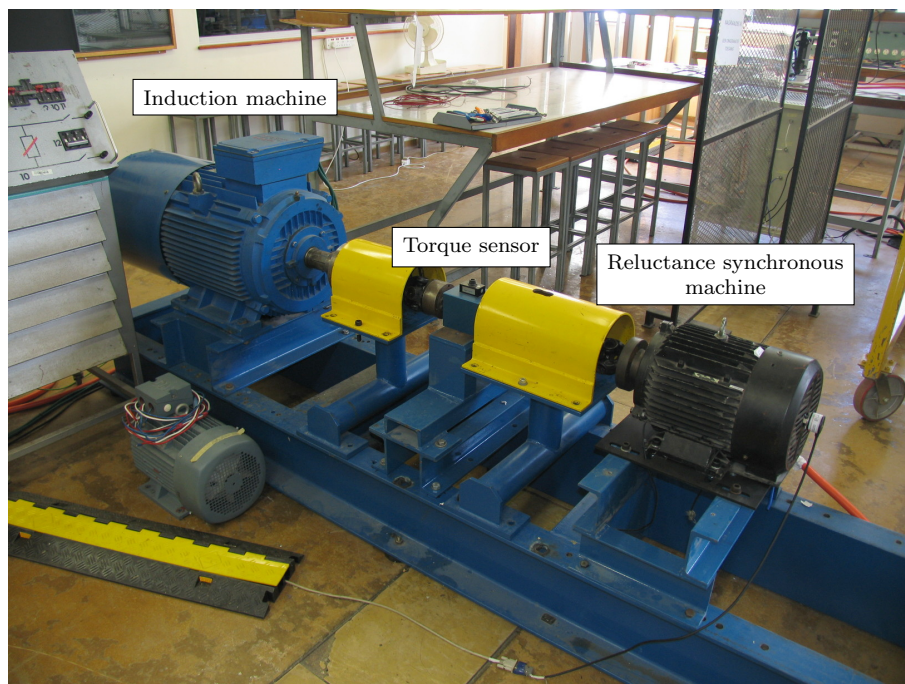


Figure 5.6: Photograph of the testbench setup with IM and RSM. A torque sensor connects the two machines.

CHAPTER 5. OVERALL WIND TURBINE RESULTS

machines is written as a kernel module that is then loaded into the kernel when the code is to be executed.

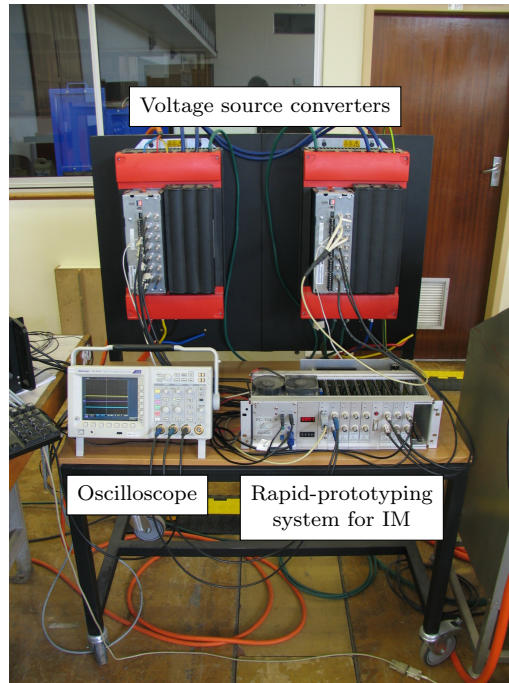


Figure 5.7: Photograph of the VSCs used along with the RPS used for controlling the IM. An oscilloscope is used for viewing system parameters in real-time.



Figure 5.8: Photograph of the RPS used for controlling the RSM and implementing the turbine control algorithm.

CHAPTER 5. OVERALL WIND TURBINE RESULTS

5.2.2. Validity of estimated generator torque

In figure 5.9, the estimated torque reported by the turbine controller along with the torque measured by the torque sensor between the RSM and the IM on the testbench is plotted. Tests are performed at the rated speed of 1500 RPM. The estimated torque results correlate well with the measured results with a slight divergence as the current magnitude begins approaching the peak current value.

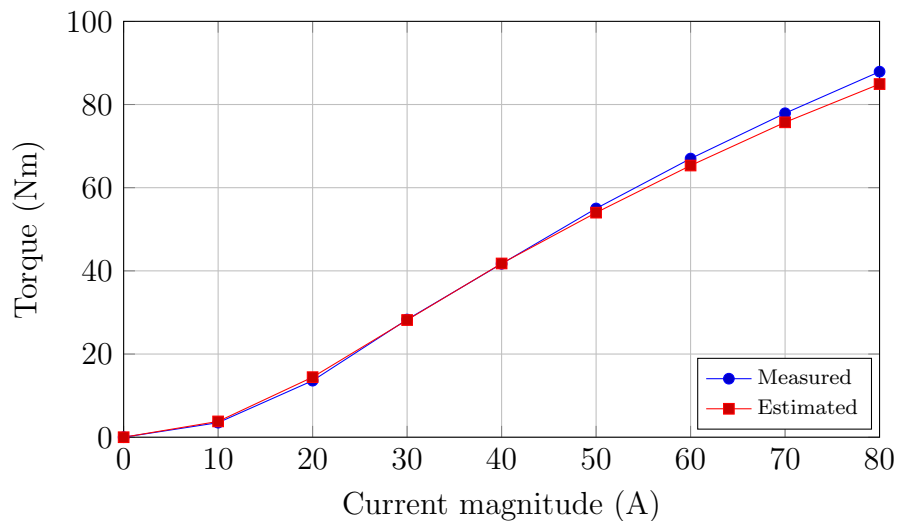


Figure 5.9: Comparison between estimated and measured generator torque, plotted against stator current magnitude at rated current angle.

Plotted in figure 5.10 is the shift in angle of the current and voltage vectors against the stator current magnitude. The current angle begins at about 68.5° at 10 A and gradually decreases towards the rated current angle of 65° as the current magnitude increases. The angle of the voltage vector in relation to the RMS rotor's d-axis begins at -55° , decreases to about -63° before increasing again to -54° .

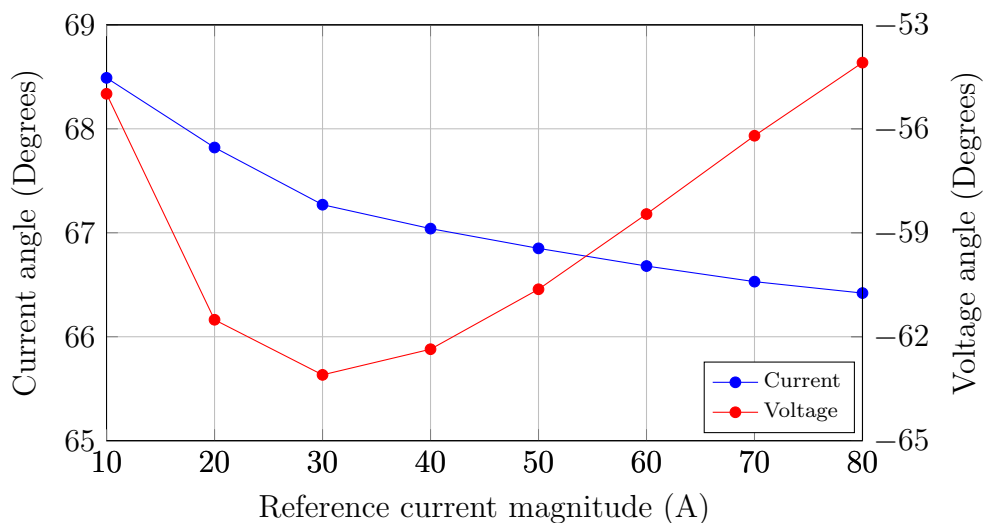


Figure 5.10: Testbench measured current and voltage angles.

CHAPTER 5. OVERALL WIND TURBINE RESULTS

5.2.3. Results from test cases ($n_g = 12$)

Plotted in figure 5.11 is the simulated wind speed, generator speed, blade power coefficient, and estimated generator torque for a 10-minute run with gearing ratio $n_g = 12$. In the test run, the turbine controller operates across all the regions of operation. The average wind speed V_0 is gradually increased throughout the run, beginning at 4 m/s and ending at 11 m/s. The graphs

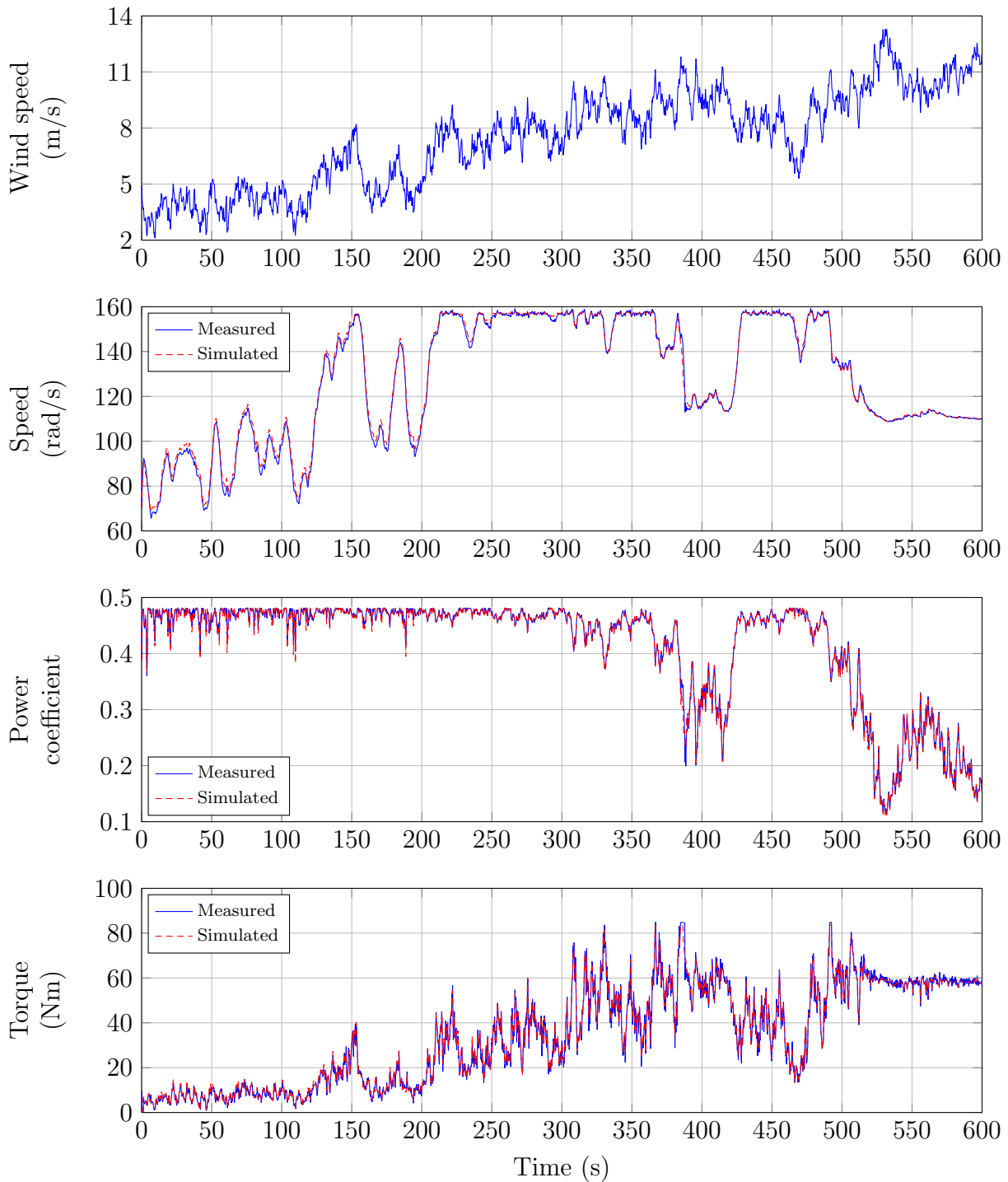


Figure 5.11: Plots of the simulated wind data, generator speed, rotor power coefficient, and generator torque estimate for a 10-minute run with $n_g = 12$.

CHAPTER 5. OVERALL WIND TURBINE RESULTS

of figure 5.11 plot the measured values from the testbench along with the simulated values from the Simulink model. At first glance, the results appear to correlate very well.

A. Maximum power point tracking operation

From figure 5.11, it is seen that the turbine is operating under MPPT control between 0 and 210 seconds. The first 120 seconds of figure 5.11 are plotted in figure 5.12 to give a closer view. The graph of the generator speed is augmented to include the optimal speed at which the generator should be operating in order to maintain optimal power coefficient of the blades. It is evident that if the turbine controller were to make the turbine hub follow the optimal speed for maximum power capture, then large swings in the generator's current reference would be required. This would cause the torque output of, as well as the electrical power produced by, the generator to fluctuate wildly too. It can also be seen how the generator speed follows the average of the optimal speed, though there is lag in response as a result of the low-pass filtering process of the SMA filter.

Examining the blade power coefficient C_p graph of figure 5.12, it is visible that there are sharp drops in C_p when the wind speed changes suddenly. This, however, is to be expected as the rotor of the turbine does not change speed quickly but rather follows the average of what it should be.

The final graph of the figure plots the “real” aerodynamic power acting on the blades, the unfiltered measured estimated hub power, the filtered measured estimated hub power, and the filtered simulated hub power. The filtered hub power follows the average of the estimated hub power, again with an obvious phase delay from the low-pass filtering process.

B. Speed-limited operation

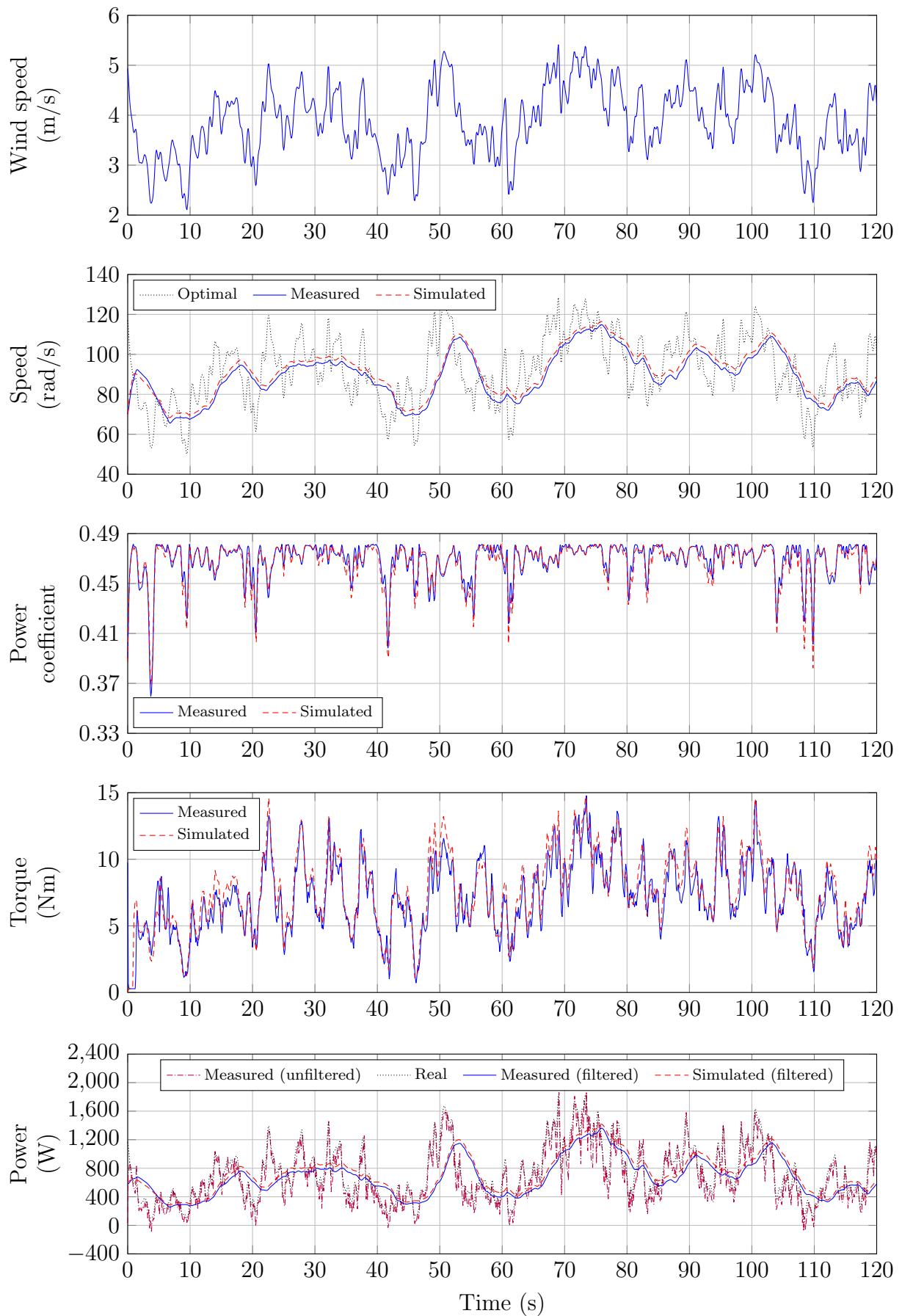
From figure 5.11, the turbine system is predominantly under speed-limited operation between 220 and 360 seconds. The time range from 200 to 320 seconds of figure 5.11 is plotted in figure 5.13, showing the turbine system entering the speed limit mode from the MPPT mode.

It is visible in the generator speed plot of figure 5.13 that as the optimal generator speed increases beyond the mechanical limit of the generator, the speed reference for the generator is simply capped at its rated limit. The generator follows the optimal speed reference again when it drops below the limit, seen occurring at around 235 seconds.

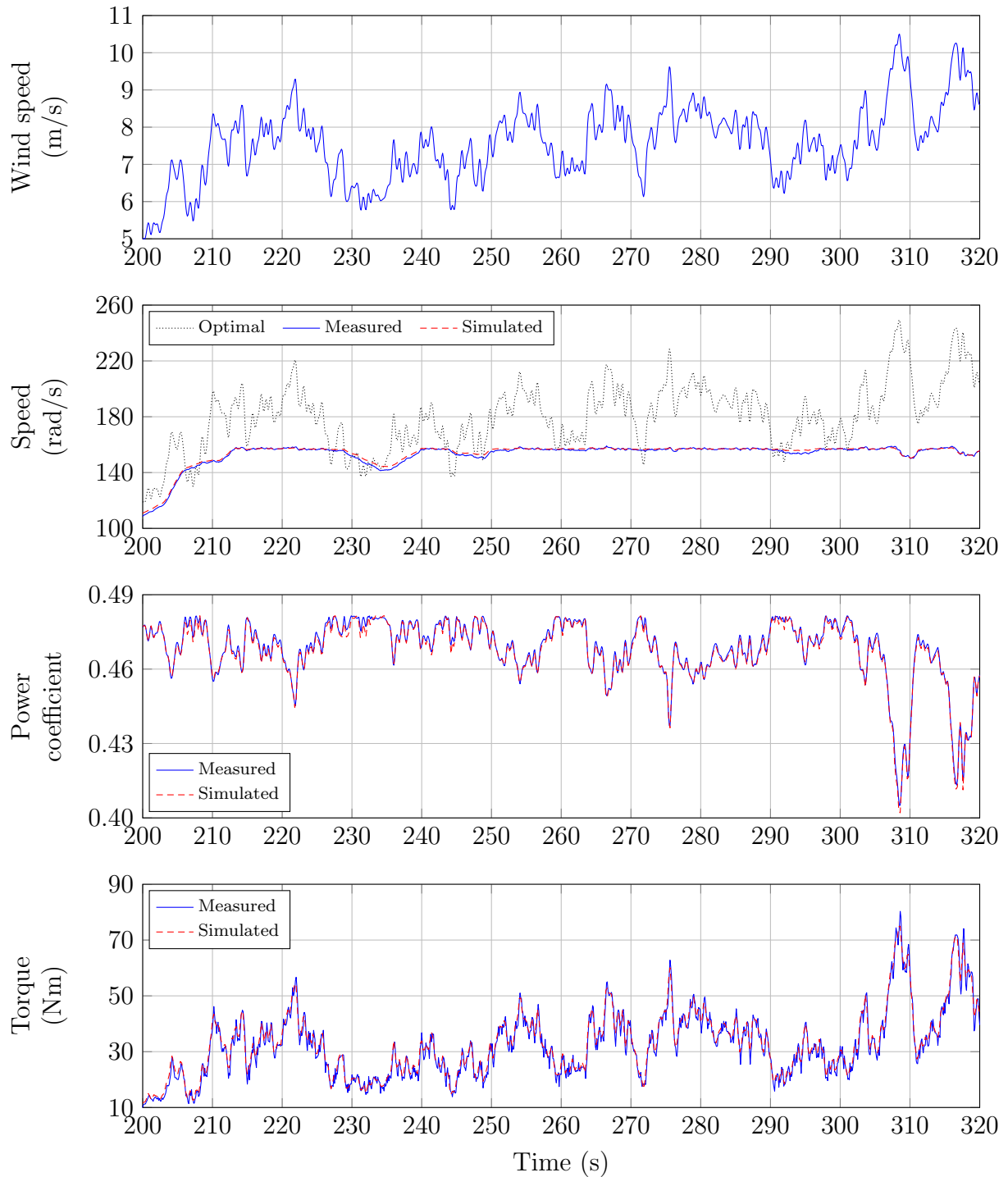
As the wind speed continues to rise gradually and the optimal generator speed ventures further away from the limit, the power coefficient begins to drop in value as the blades are unable to maintain their optimal efficiency.

Since more power is being extracted from the wind on account of the higher wind speed, the torque produced by the generator will be higher in the speed limit region compared to the MPPT region. Also, larger variations in the torque parameter will occur as well.

CHAPTER 5. OVERALL WIND TURBINE RESULTS

Figure 5.12: Closer view of the MPPT region for the $n_g = 12$ test run of figure 5.11.

CHAPTER 5. OVERALL WIND TURBINE RESULTS

Figure 5.13: Closer view of the speed-limit region for the $n_g = 12$ test run of figure 5.11.

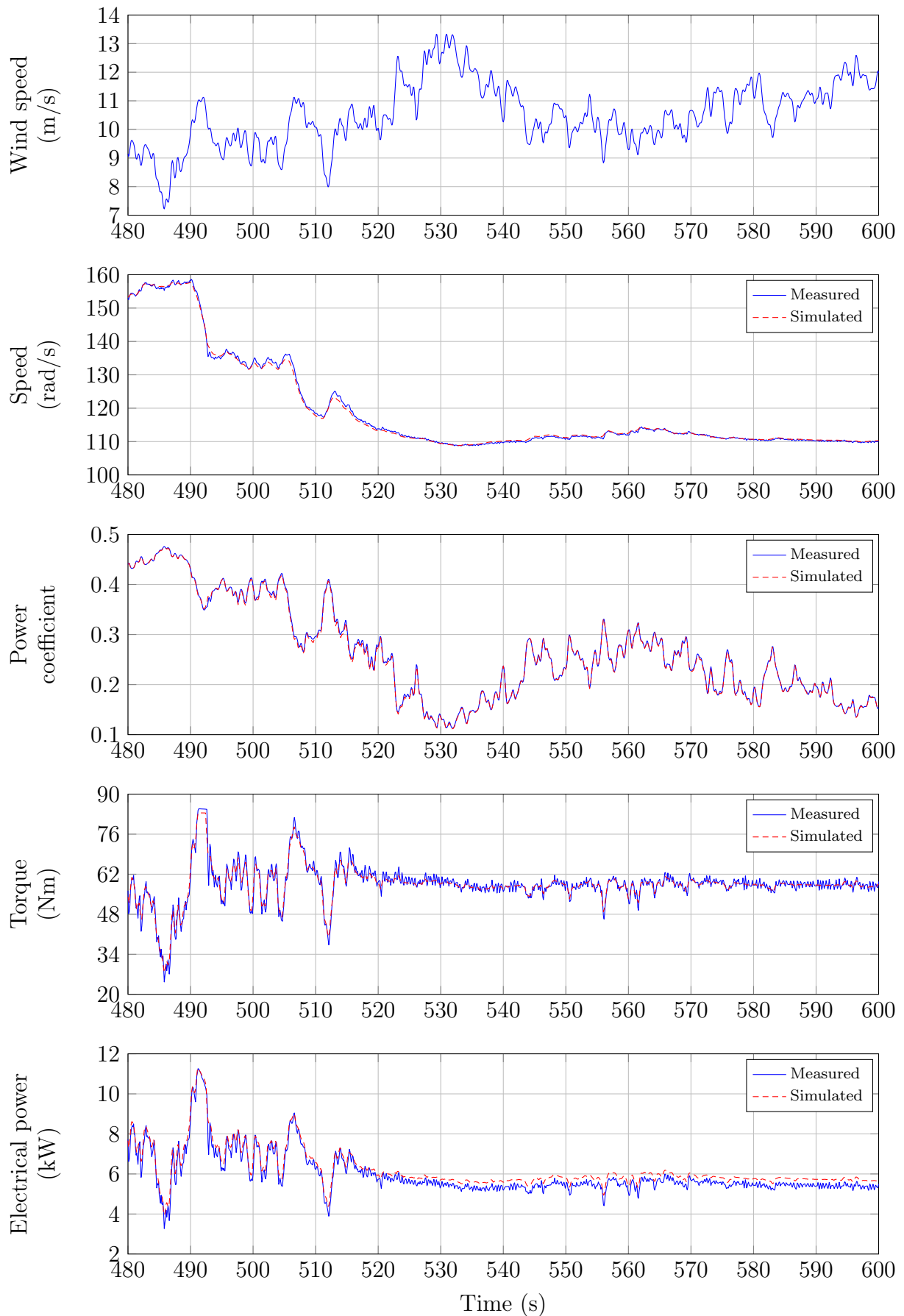
CHAPTER 5. OVERALL WIND TURBINE RESULTS

C. Torque-limited operation

Finally, from 490 seconds until the end of the run, the turbine is operating under torque-limited control. Plotted in figure 5.14 are system parameters from 480 to 600 seconds, which is when the turbine enters torque-limit control from speed-limit control.

From the generator speed graph, it is seen how the small wind gusts occurring at 490 and 505 seconds cause the generator speed to decrease rather sharply to limit the torque output of, and thus the current input to, the generator. In fact, the gust at 490 seconds causes the current controller to reach its maximum output of 80 A in the attempt to reduce the generator's speed, evidenced by the plateauing of the generator torque output. At 530 seconds, when the wind speed is around 13 m/s, the generator slows to 110 rad/s to reduce the power coefficient to as much as 0.1. As the wind speed drops somewhat around the 560 seconds mark, the generator speed is increased, and the power coefficient raised, to keep the generator torque at its rated value, 60 Nm. From the graph of the electrical power output of the generator, it is visible how the power is reduced when torque-limited soft-stalling is active.

CHAPTER 5. OVERALL WIND TURBINE RESULTS

Figure 5.14: Closer view of the torque-limit region for the $n_g = 12$ test run of figure 5.11.

CHAPTER 5. OVERALL WIND TURBINE RESULTS

5.2.4. Results from test cases ($n_g = 14$)

A second run of the testbench is performed, but for a gearing of $n_g = 14$. The results are plotted in the graphs of figure 5.15. The layout of the results is the same as before. A different wind data set is used, this time with the average wind speed V_0 beginning at 5 m/s and ending at 12 m/s.

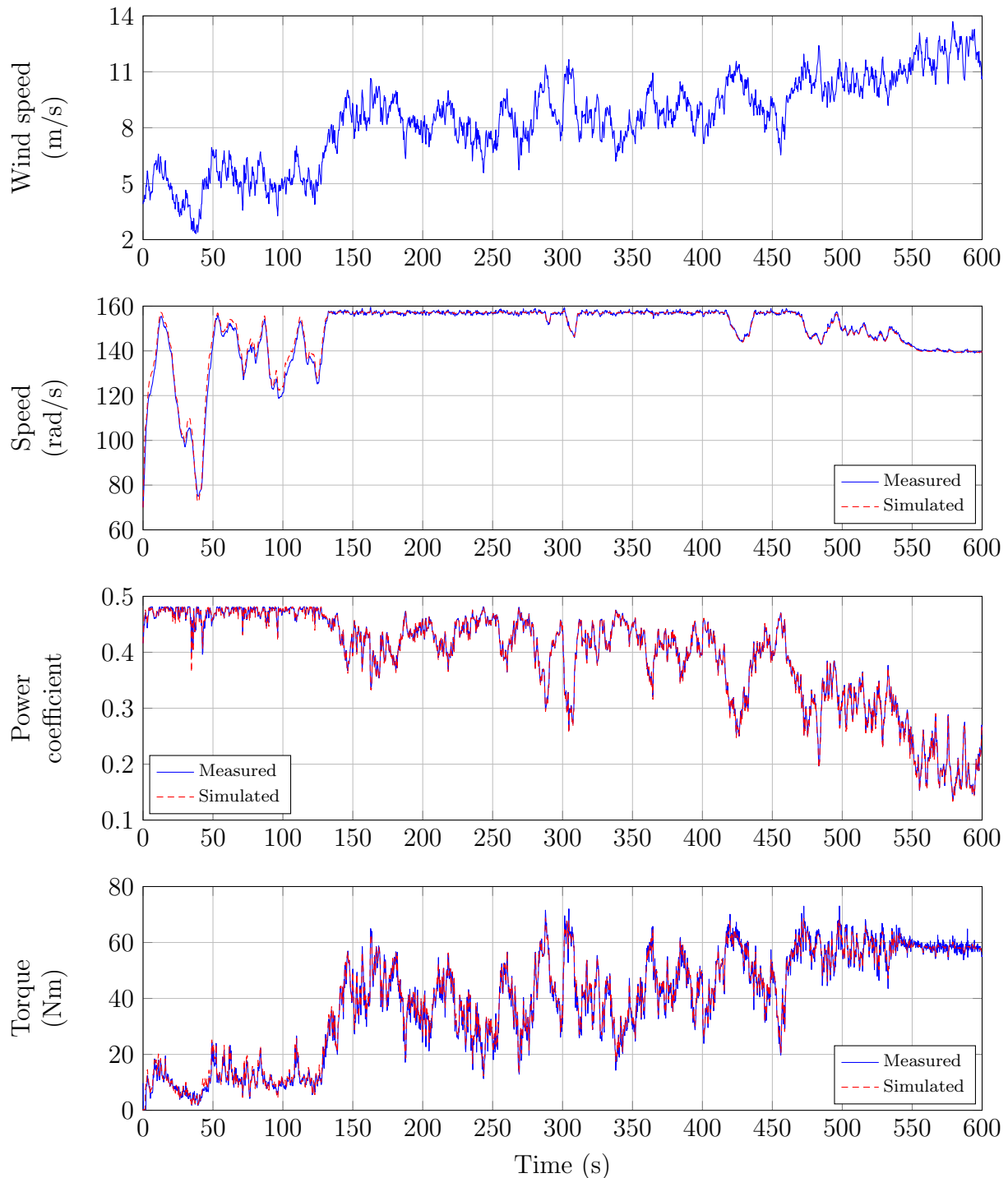


Figure 5.15: Plots of the simulated wind data, generator speed, rotor power coefficient, and generator torque estimate for a 10-minute run with $n_g = 14$.

CHAPTER 5. OVERALL WIND TURBINE RESULTS

A. Maximum power point tracking operation

As with the previous test case, the first 120 seconds of figure 5.15 is the turbine operating under MPPT and is plotted in figure 5.16. Observing the graph of the generator speed, it is noticed that the change in generator speed under MPPT control varies greater than it did for the $n_g = 12$ test case. This is a result of the gearing ratio and the fact that the generator's speed needs to change at a faster rate and a larger amount for the turbine rotor to change the equivalent amount that it did before in order to track the changing wind speed.

The graph of the power coefficient appears to vary less than the test case for $n_g = 12$. Although, this may just be a consequence of the different turbulence pattern generated for the test, even though the same parameters were used. Naturally, the turbine still experiences sudden dips in C_p with the odd wind gust or calm.

The torque and electrical power output variation of the generator is larger than the test case before, though this is to be expected when the average wind speed is 1 m/s higher across the entire run.

B. Speed-limited operation

For the speed-limited mode of operation, the time range from 150 to 270 seconds of figure 5.15 is plotted in figure 5.17. Once again, the turbine controller limits the speed reference of the generator at its mechanical limit despite the optimal speed reference being higher in value.

C. Torque-limited operation

As with the previous test case, the last 120 seconds of figure 5.15 is plotted in figure 5.17. Considering the generator speed graph, it can be seen that even though the average wind speed is slightly higher than for the $n_g = 12$ test case, the generator speed has not dropped as low in order to reduce power capture as the blades are already stalled rather heavily to begin with. With higher gearing ratios, the hub rotates at slower speeds when the turbine is operating under fixed speed. This means that for the same wind speed, provided the turbine is operating under fixed speed, the higher gearing ratio will have a slower hub speed and thus experience greater stall before torque-limit control is activated.

CHAPTER 5. OVERALL WIND TURBINE RESULTS

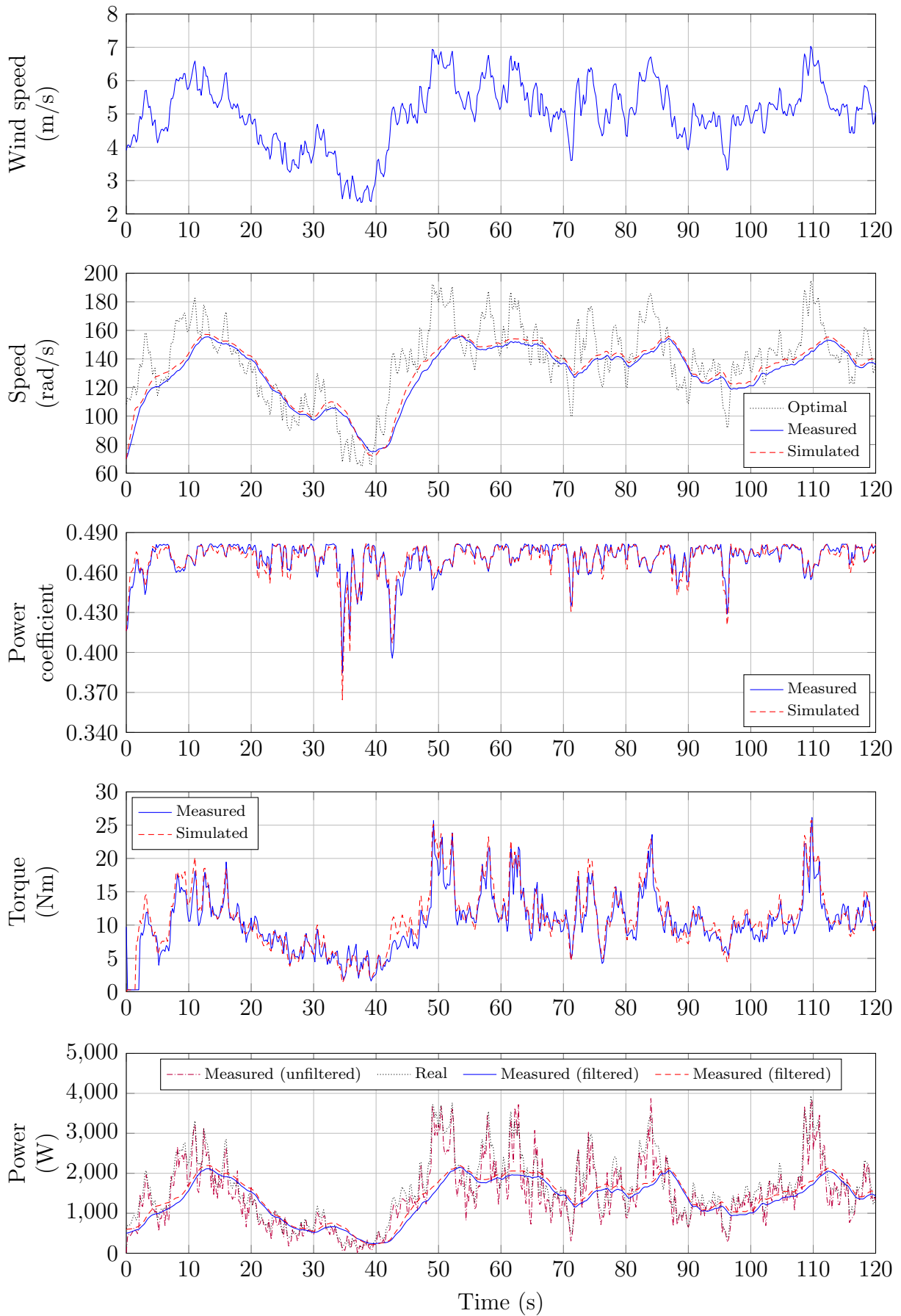


Figure 5.16: Closer view of the MPPT region for the $n_g = 14$ test run of figure 5.15.

CHAPTER 5. OVERALL WIND TURBINE RESULTS

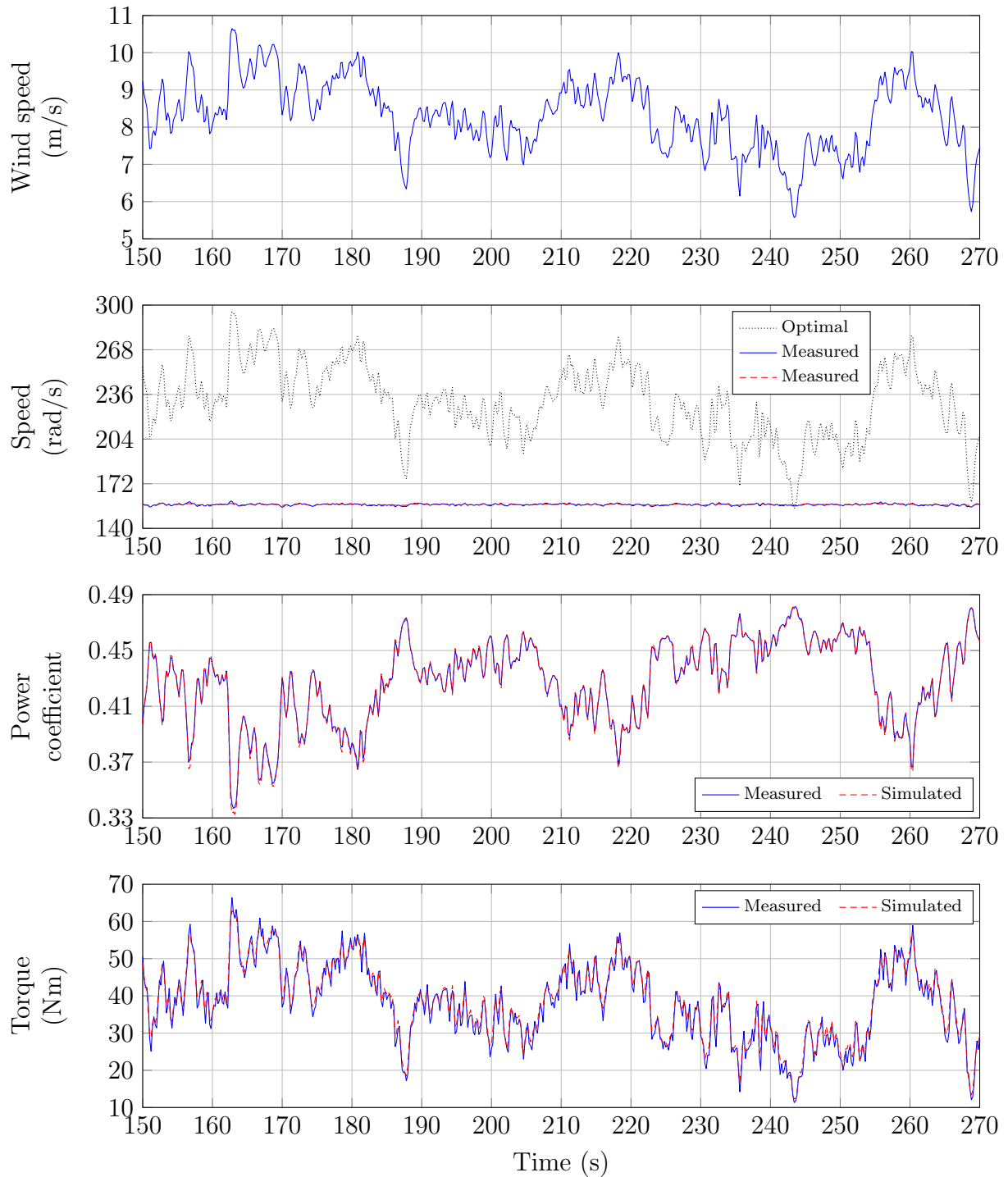
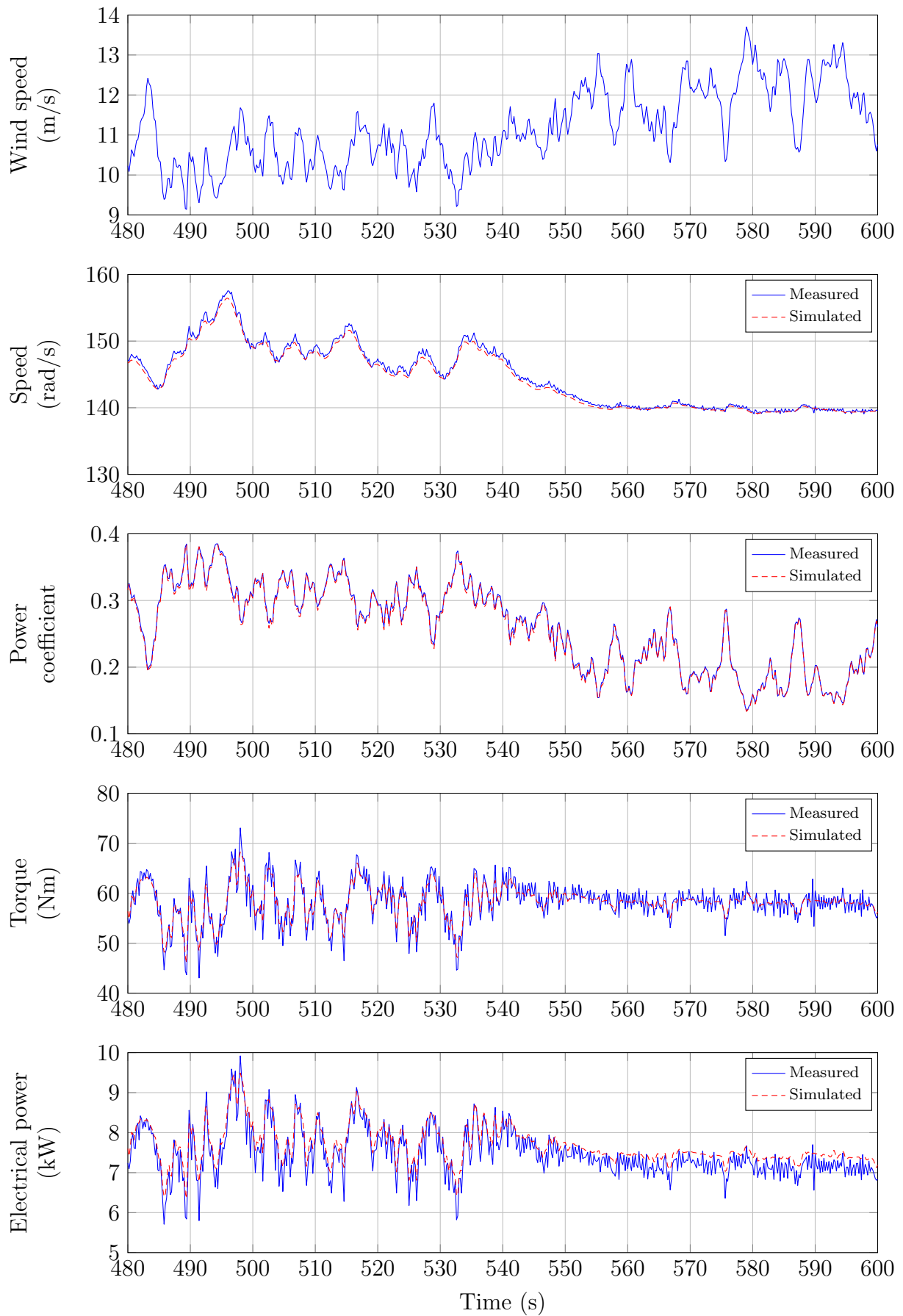


Figure 5.17: Closer view of the speed-limit region for the $n_g = 14$ test run of figure 5.15.

CHAPTER 5. OVERALL WIND TURBINE RESULTS

Figure 5.18: Closer view of the torque-limit region for the $n_g = 14$ test run of figure 5.15.

Chapter 6

Conclusions and future work

6.1. Conclusions

The desire to capture as much energy from the wind at as low a cost as possible is large. The RSM provides characteristics which make it suitable for wind turbine applications. It exhibits high efficiencies and has a high torque density when compared to IMs of the same frame size. This, coupled with the fact that RSMs are cheaper to manufacture, makes them a compelling generator technology for wind turbines.

Although the RSM used in this thesis comes from a study where it has been optimised for motoring performance, it still provides an indicative basis of the potential of the technology. Considerable research has been done and is still being conducted on improving aspects of the RSM such as the power factor for generating mode, even without assistance from permanent magnets.

A complete wind turbine simulator including wind source is developed to test the turbine control algorithm. The developed wind turbine model proves to produce results that correlated very well with the testbench measurements.

It is accepted in the literature that the speed-controlled MPPT method has the best wind speed tracking performance, and thus maintains optimal C_p of the blades, however, the method results in large fluctuations in generator torque and output power. This has implications for drivetrain fatigue and power quality provided by the turbine. The modified speed-controlled MPPT method used in this study averages the aerodynamic estimated power in order to filter the resulting generator speed reference. The modification helps to reduce the extreme variations in system parameters which means reduced drivetrain fatigue and improved power quality while maintaining satisfactory speed response to wind speed variations. However, the aforementioned improvements come at the expense of slightly reduced optimal rotor power coefficient and thus slightly lower energy yield.

During operation of the turbine under region 3, the reduction of power capture is achieved by the use of soft-stalling. However, torque limiting was implemented instead of the common power limiting as found in the literature. The implication of torque limiting over power limiting is that no limits of the generator are exceeded and the generator may continue to operate at

CHAPTER 6. CONCLUSIONS AND FUTURE WORK

above-rated wind speed conditions with no threat of thermal overload from above-rated currents as would be the case with constant-power limiting.

The RSM has strong potential to be a generator topology for wind turbines – for small-scale as well as larger-scale turbines. Its need for power electronics for optimal operation is a drawback, but variable-speed wind turbine topologies based on PMs require full-scale converters as well. The elimination of PMs in the RSM is a major cost saving aspect when compared to large-scale PMSGs. There is much research being done to improve the performance of the RSM.

6.2. Future work

A number of aspects of the turbine system potentially lend themselves to further development. These concerns will be discussed briefly in this section.

6.2.1. Blade soiling

Over time, the blades of the wind turbine will acquire dirt and grime which will degrade their performance. It would be ideal for the controller to take this parameter variation into account and alter parameters of its model of the system as time progresses. Alternatively, the variable-speed control algorithm could be replaced with one where no knowledge of the blade data is needed altogether. The turbine controller in its current state does not take into account the degradation of the blade performance. It is uncertain as to what extent blade soiling would have on the overall performance of the turbine system with the current implemented control system.

A few methods of turbine control have been developed that do not require knowledge of the system model at all. Their basic solution to the problem is to change some parameter of the system and observe the outcome. This process is known perturb-and-observe (P&O) and has been covered briefly in the introduction chapter.

6.2.2. Air density

The MPPT algorithm that determines the optimal hub speed is sensitive to changes in the air density. The equation given by (3.48) is reproduced here for reference:

$$\omega[k+1] = \sqrt[3]{\frac{P_a[k]}{K_{\text{opt}}}} \quad (6.1)$$

where

$$K_{\text{opt}} = \frac{1}{2} \rho \pi R^5 \frac{C_{p-\text{opt}}}{\lambda_{\text{opt}}^3}. \quad (6.2)$$

From (6.2), it is noticed that a change in the air density ρ will result in a change in the constant K_{opt} . Inaccuracies in this variable will cause the turbine to command a hub speed resulting in a suboptimal blade power coefficient. A brief investigation into the effects of the

CHAPTER 6. CONCLUSIONS AND FUTURE WORK

atmospheric conditions on the air density ρ starts with the ideal gas law, expressed as a function of temperature and pressure, and given by the equation

$$\rho = \frac{P}{R_0 T_k} \quad (6.3)$$

where P is absolute pressure, R_0 is the specific gas constant for dry air, and T_k is the absolute temperature. From (6.3), it is seen that the density of air is proportional to pressure and inversely proportional to temperature. The variation in air temperature, with respect to time, is greater than the variation in pressure. Pressure changes only slightly with respect to time and is more dependent on altitude variation. For this reason, the temperature of air has a greater effect on air density than pressure. Plotted in figure 6.1 is the air density against temperature.

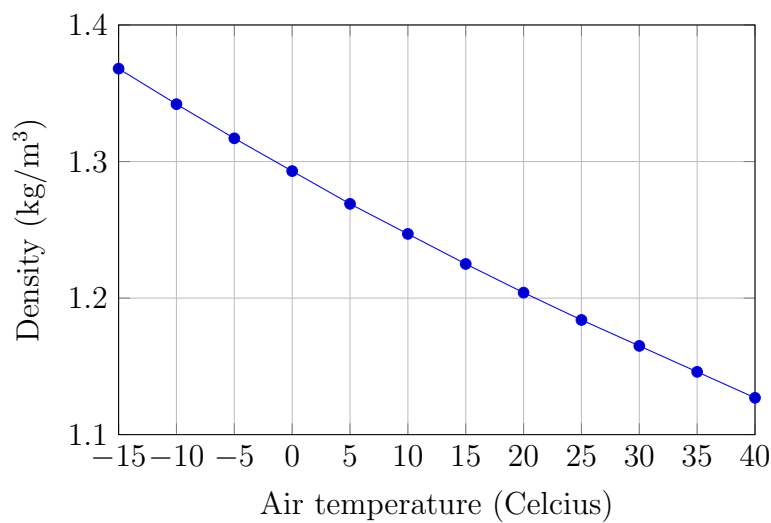


Figure 6.1: Change in density of dry air versus air temperature.

The implemented wind turbine controller does not measure air temperature and thus does not compensate for any changes in air density. The result is that extreme variations in temperature will cause the wind turbine to operate at suboptimal speeds for maximum power capture during MPPT control. Implementation of a temperature sensor for air density compensation should be a simple addition.

*CHAPTER 6. CONCLUSIONS AND FUTURE WORK***6.2.3. Torque control MPPT**

The algorithm of the turbine controller under region 2 operation utilises the speed-reference method to obtain MPPT control. It is accepted in the literature that speed-controlled MPPT results in more extreme variations of the rotor speed and drivetrain torque in order to maintain optimal power coefficient. In order to mitigate this effect, the speed reference is averaged by means of filtering the aerodynamic estimated power. The alternative to this speed-control MPPT method is to use the torque-control method. This method allows for much gentler torque variations of the drivetrain at the expense of tracking response and thus reduced power coefficient.

Perhaps a hybrid MPPT control between the speed- and torque-control methods could be developed for improved tracking response of the torque-control method but with reduced system parameter variations of the speed-control method.

Bibliography

- [1] H. Polinder et al. ‘Trends in Wind Turbine Generator Systems’. In: *Emerging and Selected Topics in Power Electronics* 1.3 (Sept. 2013), pp. 174–185.
- [2] M. Abarzadeh, H. M. Kojabadi and L. Chang. ‘Power Electronics in Small Scale Wind Turbine Systems’. In: *Advances in Wind Power*. Ed. by R. Carriveau. 2012. ISBN: 978-953-51-0863-4. DOI: 10.5772/51918.
- [3] Z. Alnasir and M. Kazerani. ‘Performance Comparison of Standalone SCIG and PMSG-Based Wind Energy Conversion Systems’. In: *27th Canadian Conference on Electrical and Computer Engineering*. May 2014, pp. 1–8.
- [4] S. Gsänger and J. Pitteloud. *Small Wind World Report 2014*. URL: <http://www.wwindea.org> (Accessed: 01/12/2014).
- [5] J.H.J. Potgieter. ‘Optimal Topology and Critical Evaluation of Slip Synchronous Permanent Magnet Wind Generator’. PhD thesis. Stellenbosch University, 2014.
- [6] I. Al-Bahady. ‘Building a wind turbine for rural home’. In: *Energy for Sustainable Development* (2009).
- [7] K. E. Johnson. *Adaptive Torque Control of Variable Speed Wind Turbines*. Tech. rep. National Renewable Energy Laboratory, 2004.
- [8] A. Mirecki, X. Roboam and F. Richardeau. ‘Architecture Complexity and Energy Efficiency of Small Wind Turbines’. In: *IEEE Transactions on Industrial Electronics* 54.1 (Feb. 2007), pp. 660–670.
- [9] C. Lewis and J. Müller. ‘A Direct Drive Wind Turbine HTS Generator’. In: *Power Engineering Society General Meeting*. June 2007, pp. 1–8.
- [10] H. Polinder et al. ‘Comparison of Direct-Drive and Geared Generator Concepts for Wind Turbines’. In: *IEEE International Conference on Electric Machines and Drives*. May 2005, pp. 543–550.
- [11] W. Liang and W. Liu. ‘Key Technologies Analysis of Small Scale Non-Grid-Connected Wind Turbines: A Review’. In: *World Non-Grid-Connected Wind Power and Energy Conference*. Nov. 2010, pp. 1–6.
- [12] W. E. Leithead. ‘Dependence of performance of variable speed wind turbines on the turbulence, dynamics and control’. In: *Generation, Transmission and Distribution, IEE Proceedings C* 137.6 (Nov. 1990), pp. 403–413.

BIBLIOGRAPHY

- [13] E. Muljadi, C. P. Butterfield and P. Migliore. ‘Variable Speed Operation of Generators with Rotor-Speed Feedback in Wind Power Applications’. In: *Fifteenth ASME Wind Energy Symposium*. 1996.
- [14] S. Arnaltes. ‘Comparison of Variable Speed Wind Turbine Control Strategies’. In: *Proceedings of the International Conference on Renewable Energies and Power Quality*. Apr. 2003.
- [15] E. Muljadi, K. Pierce and P. Migliore. ‘A Conservative Control Strategy for Variable-Speed Stall-Regulated Wind Turbines’. In: *19th American Society of Mechanical Engineers (ASME) Wind Energy Symposium*. Jan. 2000.
- [16] URL: <http://www.windturbinestar.com/> (Accessed: 01/12/2014).
- [17] URL: <http://www.bergey.com/> (Accessed: 01/12/2014).
- [18] URL: <http://www.callaglory.com/> (Accessed: 01/12/2014).
- [19] URL: <http://www.fortiswindenergy.com/> (Accessed: 01/12/2014).
- [20] URL: <http://www.gaia-wind.com/> (Accessed: 01/12/2014).
- [21] URL: <http://www.ghrepower.com/en/> (Accessed: 01/12/2014).
- [22] URL: <http://www.hopefulenergy.com/> (Accessed: 01/12/2014).
- [23] URL: <http://www.qdfzy.com/en/> (Accessed: 01/12/2014).
- [24] URL: <http://www.venterawind.com/> (Accessed: 01/12/2014).
- [25] URL: <http://www.wipo-windpower.com> (Accessed: 01/12/2014).
- [26] A. Luna et al. ‘Low Voltage Ride Through Strategies for SCIG Wind Turbines in Distributed Power Generation Systems’. In: *Power Electronics Specialists Conference*. June 2008, pp. 2333–2339.
- [27] A. D. Hansen and L. H. Hansen. ‘Market penetration of wind turbine concepts over the years’. In: *2007 European Wind Energy Conference and Exhibition*. May 2007.
- [28] M. R. J. Dubois. ‘Optimized Permanent Magnet Generator Topologies for Direct-Drive Wind Turbines’. PhD thesis. Delft University of Technology, 2004.
- [29] J. Chen, J. Chen and C. Gong. ‘New Overall Power Control Strategy for Variable-Speed Fixed-Pitch Wind Turbines Within the Whole Wind Velocity Range’. In: *IEEE Transactions on Industrial Electronics* 60.7 (Apr. 2012), pp. 2652–2660.
- [30] J. A. Baroudi, V. Dinavahi and A. M. Knight. ‘A Review of Power Converter Topologies for Wind Generators’. In: *IEEE International Conference on Electric Machines and Drives*. May 2005, pp. 458–465.
- [31] N. Madani. ‘Design of a Permanent Magnet Synchronous Generator for a Vertical Axis Wind Turbine’. MA thesis. KTH Royal Institute of Technology, 2011.

BIBLIOGRAPHY

- [32] A. M. Eltamaly and H. M. Farh. ‘Maximum power extraction from wind energy system based on fuzzy logic control’. In: *Electric Power Systems Research* 97 (Apr. 2013), pp. 144–150.
- [33] L. Bisenieks, D. Vinnikov and I. Galkin. ‘New Converter for Interfacing PMSG based Small-Scale Wind Turbine with Residential Power Network’. In: *Compatibility and Power Electronics, 7th International Conference-Workshop*. June 2001, pp. 354–359.
- [34] A. McIver, D. G. Holmes and P. Freere. ‘Optimal Control of a Variable Speed Wind Turbine under Dynamic Wind Conditions’. In: *Industry Applications Conference*. Vol. 3. 1996, pp. 1692–1698.
- [35] M. G. Simões, B. K. Bose and J. Ronald. ‘Design and Performance Evaluation of a Fuzzy Logic Based Variable Speed Wind Generation System’. In: *IEEE Transactions on Industry Applications* 33.4 (1997).
- [36] E. Muljadi, K. Pierce and P. Migliore. ‘Control Strategy for Variable-Speed, Stall-Regulated Wind Turbines’. In: 1998.
- [37] R. Datta and V. T. Ranganathan. ‘A Method of Tracking the Peak Power Points for a Variable Speed Wind Energy Conversion System’. In: *IEEE Transactions on Energy Conversion* (Mar. 2003), pp. 163–168.
- [38] Q. Wang and L. Chang. ‘An Intelligent Maximum Power Extraction Algorithm for Inverter-Based Variable Speed Wind Turbine Systems’. In: *IEEE Transactions on Power Electronics*. Vol. 19. Sept. 2004, pp. 1242–1249.
- [39] E. Koutroulis and K. Kalaitzakis. ‘Design of a Maximum Power Tracking System for Wind-Energy-Conversion Applications’. In: *IEEE Transactions on Industrial Electronics* 53.2 (2006), pp. 486–494.
- [40] M. Narayana et al. ‘Generic maximum power point tracking controller for small-scale wind turbines’. In: *Renewable Energy* 44 (2012), pp. 72–79.
- [41] J. S. Thongam et al. ‘A Method of Tracking Maximum Power Points in Variable Speed Wind Energy Conversion Systems’. In: *Power Electronics, Electrical Drives, Automation and Motion (SPEEDAM)*. 2012, pp. 1095–1100.
- [42] T. Thiringer and J. Linders. ‘Control by variable rotor speed of a fixed pitch wind turbine operating in a wide speed range’. In: *IEEE Trans. Energy Conversion*. Vol. 8. Sept. 1993, pp. 520–526.
- [43] S. Bhowmik and R. Spée. ‘Wind Speed Estimation Based Variable Speed Wind Power Generation’. In: *IECON '98. Proceedings of the 24th Annual Conference of the IEEE Industrial Electronics Society*. Vol. 2. 1998, pp. 596–601.
- [44] A. M. Eltamaly, A. I. Alolah and H. M. Farh. ‘Maximum Power Extraction from Utility-Interfaced Wind Turbines’. In: *Advances in Wind Power*. Ed. by R. Carriveau. 2012. ISBN: 978-953-51-0863-4. DOI: 10.5772/51918.

BIBLIOGRAPHY

- [45] A. Z. Mohamed, M. N. Eskander and F. A. Ghali. 'Fuzzy logic control based maximum power tracking of a wind energy system'. In: *Renewable Energy* 23.2 (June 2001), pp. 235–245.
- [46] V. Calderaro et al. 'A fuzzy controller for maximum energy extraction from variable speed wind power generation systems'. In: *Electric Power Systems Research* 78.6 (June 2008), pp. 1109–1118.
- [47] K. Belmokhtar, M. L. Doumbia and K. Agbossou. 'Modelling and fuzzy logic control of DFIG based Wind Energy Conversion Systems'. In: *IEEE International Symposium on Industrial Electronics*. May 2012, pp. 1888–1893.
- [48] H. Wagner and J. Mathur. *Introduction to Wind Energy Systems: Basics, Technology and Operation*. 2nd ed. Springer, 2013. ISBN: 978-3-642-32976-0.
- [49] E. Muljadi and C. P. Butterworth. 'Soft-Stall Control versus Furling Control for Small Wind Turbine Power Regulation'. In: *Windpower '98*. Apr. 1998.
- [50] J. T. Bialasiewicz. 'Furling Control for Small Wind Turbine Power Regulation'. In: *IEEE International Symposium on Industrial Electronics*. June 2003, pp. 804–809.
- [51] M.J. Kamper. 'Design Optimisation of Cageless Flux Barrier Rotor Reluctance Synchronous Machine'. PhD thesis. Stellenbosch University, 1996.
- [52] A. Boglietti and M. Pastorelli. 'Induction and synchronous reluctance motors comparison'. In: *34th Annual Conference of the IEEE Industrial Electronics Society*. Nov. 2008, pp. 2041–2044.
- [53] J. du Plooy. 'Performance Comparison for Motoring and Generating Modes of a Reluctance Synchronous Machine'. In: *Southern African Universities Power Engineering Conference*. Feb. 2014.
- [54] R. Vartanian et al. 'Power Factor Improvement of Synchronous Reluctance Motors (SynRM) Using Permanent Magnets for Drive Size Reduction'. In: *Applied Power Electronics Conference and Exposition*. Feb. 2012, pp. 628–633.
- [55] S. Morimoto, M. Sanada and Y. Takeda. 'Performance of PM-Assisted Synchronous Reluctance Motor for High-Efficiency and Wide Constant-Power Operation'. In: *IEEE Transactions on Industry Applications* 37.5 (Sept. 2001), pp. 1324–1240.
- [56] H.W. de Kock. 'Position Sensorless and Optimal Torque Control of Reluctance and Permanent Magnet Synchronous Machines'. PhD thesis. Stellenbosch University, 2009.
- [57] W. T. Villet et al. 'Evaluation of a Simplified High Frequency Injection Position Sensorless Control Method for Reluctance Synchronous Machine drives'. In: *6th IET International Conference on Power Electronics, Machines and Drives*. Mar. 2012, pp. 1–6.
- [58] S. Tokunaga and K. Kesamaru. 'FEM Simulation of Novel Small Wind Turbine Generation System with Synchronous Reluctance Generator'. In: *International Conference on Electrical Machines and Systems*. Aug. 2011.

BIBLIOGRAPHY

- [59] D. Artioli. ‘An Innovative Type of Synchronous Electric Generator without Rare Earth Materials and with High Efficiency’. In: *EWEA 2012*. Apr. 2012.
- [60] W. T. Villet. ‘Critical Evaluation and Application of Position Sensorless Control Techniques for Reluctance Synchronous Machines’. PhD thesis. Stellenbosch University, 2014.
- [61] H.W. de Kock. ‘Dynamic Control of the Permanent Magnet Assisted Reluctance Synchronous Machine with Constant Current Angle’. MA thesis. Stellenbosch University, 2006.
- [62] R. Morales-Caporal and M. Pacas. ‘A Predictive Torque Control for the Synchronous Reluctance Machine Taking Into Account the Magnetic Cross Saturation’. In: *IEEE International Electric Machines & Drives Conference*. Vol. 1. May 2007, pp. 59–64.
- [63] I. Boldea, Z.X. Fu and S.A. Nasar. ‘High-performance reluctance generator’. In: *IEEE Proceedings B (Electric Power Applications)*. Vol. 140. 1993, pp. 124–130.
- [64] International Electrotechnical Commission (IEC). *IEC61400-1: Wind turbines - Part 1: Design requirements*. 2005.